

Symmetry breaking in interacting Fermi systems with the functional renormalization group

Von der Fakultät Mathematik und Physik der Universität Stuttgart
zur Erlangung der Würde eines Doktors der Naturwissenschaften
(Dr. rer. nat.) genehmigte Abhandlung

vorgelegt von

Roland Gersch

aus Köln

Hauptberichter: Prof. Dr. Walter Metzner
Mitberichter: Prof. Dr. Alejandro Muramatsu
Tag der mündlichen Prüfung: ????

Max-Planck-Institut für Festkörperforschung
Stuttgart 2007

To those who use this

Contents

1	Introduction	9
1.1	Context	9
1.1.1	Functional renormalization group schemes	9
1.1.2	Counterterms	12
1.1.3	Hubbard model	13
1.2	In this work	14
2	Charge-density wave: mean-field approach	18
2.1	Second-order phase transitions	18
2.1.1	Model	18
2.1.2	Mean-field solution and resummation	21
2.1.3	Dimensionless example	25
2.2	First-order phase transitions	27
2.2.1	Model	27
2.2.2	Mean-field treatment	28
2.2.3	Example: two dimensions	31
3	Deriving the renormalization group scheme	34
3.1	General formalism for symmetry breaking	34
3.2	Introducing the cutoff	36
3.3	Generating functionals	36
3.4	The flow equation for the effective action	36
3.5	The flow equations for the 1PI vertex functions	38
3.6	The Katanin truncation	42
4	Charge-density wave: renormalization-group approach	45
4.1	Second-order phase transitions	45
4.1.1	Renormalization group setup	45
4.1.2	Renormalization group and resummation	47
4.1.3	Flow equations at finite temperature	49
4.1.4	Renormalization group at zero temperature	51
4.1.5	Renormalization group flows at finite temperatures	53
4.2	First-order phase transitions	56
4.2.1	Renormalization group setup with counterterm	58
4.2.2	Flows for first-order phase transitions	61

4.2.3	Counterterm flows for second-order phase transitions	63
4.2.4	External field	63
5	Attractive Hubbard model	67
5.1	Resummation approach to Cooper and forward scattering	67
5.1.1	Fermions with Cooper and forward scattering	68
5.1.2	Gap equation	70
5.1.3	Bethe-Salpeter equation	72
5.1.4	Redundancies of \mathbb{V}	74
5.1.5	Momentum-independent scattering	76
5.2	Resummation approach to the attractive Hubbard model	78
5.2.1	Hamiltonian	78
5.2.2	Resummation approach	79
5.2.3	No Nambu rank reduction	80
5.2.4	Numerical setup	81
5.2.5	Numerical results: momentum space	82
5.2.6	Numerical results: frequency space	85
5.2.7	Combinations of effective interactions	89
5.3	Renormalization group	92
5.3.1	Flow equations	93
5.3.2	Numerical setup	96
5.3.3	Momentum-shell flows	98
5.3.4	Interaction flows	105
5.3.5	Order parameter for superconductivity	106
6	Conclusions	110
A	Deutsche Zusammenfassung	113
B	Matsubara sums	117
C	Bubble integrands	119
D	Tadpole integrands	123

Nomenclature

$3 + 1$	odd number of incoming and outgoing legs
χ	cutoff function
Δ	off-diagonal self-energy or external field
Δ_c	counterterm
\mathbb{G}	matrix Green's function
Γ	effective action
Λ	cutoff parameter
Λ_c	critical scale
\mathbb{U}	matrix of effective interactions
μ	chemical potential
ν	multiplicity of degrees of freedom introduced to take into account symmetry breaking
ν_m	bosonic Matsubara frequency
Ω	thermodynamic potential (only in chapters 2 and 4)
ω_n	fermionic Matsubara frequency
ψ, ϕ	Grassmannian fields
\mathbb{Q}	quadratic part of the action
ρ	density of states
\mathbb{S}	single-scale propagator
Σ	self-energy
σ_i	Pauli matrix
ε	dispersion relation

\mathbf{Q}	(π, π, \dots)
ξ	dispersion relation minus chemical potential
B	bubble
c, c^\dagger	annihilation/creation operator
E	quasi-particle dispersion
H	Hamiltonian
S	action
T	temperature
t, t'	hopping amplitude between nearest and next-nearest neighbors, respectively
T_c	critical temperature
U_0, V_0	bare couplings/interactions
V, U, Ω, X, W	effective interactions
W	one half of the bandwidth in chapters before the fifth, anomalous effective interaction therein and thereafter
\mathcal{W}	generating functional of the connected Green's functions
\mathcal{Z}	partition function
1PI	one-particle irreducible
BCS	Bardeen, Cooper, Schrieffer
BEC	Bose-Einstein condensation
CDW	charge-density wave
det	determinant
DoS	density of states
eff	effective
ext	external
FRG	functional renormalization group
i.a.	interacting or interaction
Im	imaginary part

kin kinetic

MF mean field

PH particle-hole

PP particle-particle

Re real part

RG renormalization group

RHS right-hand side

td. pot. thermodynamic potential

Tr Trace

w/o fw setting all $3 + 1$ effective interactions to zero

with fw keeping all $3 + 1$ effective interactions

Chapter 1

Introduction

1.1 Context

Interacting many-particle systems contain fascinating physics, presenting a wealth of phases with experimentally and technologically exploitable properties as disparate as superconductivity, large magnetoresistances and multiferroicity. Theoretically understanding the occurrence of these phenomena would facilitate the development of new materials as well as their technological employment while empowering experimentalists to optimize their measurements and experiments. However, microscopically understanding the phase transitions which are at the heart of the problem is an intriguing challenge epitomized by the break-down of perturbation theory, which is so successful in other fields of theoretical physics.

1.1.1 Functional renormalization group schemes

Renormalization group (RG) methods are powerful tools that facilitate the systematic investigation of the physics of many-particle systems even in situations where perturbation theory breaks down. In the Wilsonian RG approach for an action containing monomials up to quartic order in the underlying fields, the degrees of freedom are ordered by their kinetic energy and taken into account successively. Contributions from the individual degrees of freedom are summed up starting at the highest energy. This can be viewed as generating a family of effective actions called the RG flow and parametrized by the lowest energy scale taken into account, which is called the cutoff. Wilson (1971b) originally devised this method to investigate critical phenomena in a generalized Ising model. Some important points in the development of his idea are listed in the following. Weinberg (1973) explicitly included the momentum dependence of the self-energy for the first time beyond Z -factor renormalization in an RG calculation. Wegner and Houghton (1973) employed an effective Hamiltonian as a generating functional to derive exact RG equations. Nicoll and Chang (1977), focussing on the generating functional for the one-particle irreducible (1PI) Green's functions, found both an explicit differential equation for the generating functional as well as a simplification of the Wegner-Houghton flow equations. Accessing the RG via a generating functional proved

to be a fruitful avenue: Polchinski (1984) started from the partition function to obtain a hierarchy of differential equations allowing him to prove renormalizability of certain scalar field theories. Wiczerkowski (1988) derived a different but also exact hierarchy which is particularly well-suited for mathematical considerations. Wetterich (1993) developed a flow equation for the 1PI effective action and derived a hierarchy of differential equations for the 1PI vertex functions, motivated by critical phenomena in statistical mechanics and high-temperature phase transitions in particle physics.

The term ‘exact RG’ is frequently used if an exact flow equation or exact hierarchy of flow equations as described above is used to derive an approximation. However, if fermionic models are studied in this way, the term ‘functional RG’ (fRG) is also common, and is adopted in the following. Early investigations using Wilson’s RG for fermions were undertaken by Benfatto and Gallavotti (1990); Feldman and Trubowitz (1990, 1991). This approach together with an analytical classification of the parts of the flowing coupling functions according to RG relevance was popularized by Shankar (1991, 1994). A hierarchy of fermionic flow equations was derived by Salmhofer (1998a) from the Wick-ordered effective interaction and used for mathematical investigations. Later, an equivalent flow equation hierarchy was derived from the generator of the 1PI vertex functions by Salmhofer and Honerkamp (2001). This work is based on the latter hierarchy. Another recent development for fermions is the exact hierarchy of two-particle irreducible flow equations (Dupuis (2005)) named after the property of the vertex functions calculated in the flow. They have proven convenient for the study of symmetry-breaking due to the favorable analytical properties of these vertex functions. We note the first dimension of the structure of the fRG field which this work belongs to: there are various *schemes*, equivalent in principle, whose differences are reflected in the quantities calculated and the diagrams used in their formulation. The distinction is important because approximations are used in most applications and may lead to variations in the results depending on the scheme employed.

The solid and versatile formal base which the generating functionals provide has also leveraged the development of new types of flow parameters. It was realized that the cutoff can formally be introduced via a cutoff function which can be chosen arbitrarily provided that certain differentiability conditions are met and that there is a well-understood starting point. While earlier investigations mostly refer to the physically appealing original energy- or momentum-shell cutoff, taking into account the degrees of freedom ordered by their frequency has proven similarly successful (Enss (2005); Andergassen (2006)). Perhaps more astonishingly, the physical temperature (Honerkamp and Salmhofer (2001)) as well as the interaction strength (Honerkamp et al. (2004)) have been introduced as flow parameters. The latter two procedures have the computational advantage of scanning a slice of the phase diagram in a single RG run, while the former schemes yield information about a single point only. Thus, we note a second dimension in the structure of the field: different *cutoff functions*, equivalent in principle but exhibiting specific advantages and disadvantages in practice, can be chosen.

In studies of the electronic structure of condensed matter, the basic building blocks are spin- $\frac{1}{2}$ electrons, which are fermions. However, it can be advantageous to formally replace fermion bilinears with bosonic fields to remove the part of the action quartic (and troublesome) in the original fermions (Altland and Simons (2006)). This exact process is called a Hubbard-Stratonovich transformation. It permits simplifications based on physical intuition about the bosonic fields. However, the decoupling of the quartic part of the action is ambiguous insofar as the distribution of the fermionic interaction over different bosonic channels can be varied. This variation introduces a bias into the approximations that follow. The fRG literature based on the idea of introducing bosons is rooted in field-theoretic high-energy physics, building on the approach by Wetterich (1993). At first, investigations focussed on field-theoretical models. By exploiting an analogy to quantum electrodynamics, Bergerhoff et al. (1996) discussed the nature of the transition in both type-I and type-II superconductors. Symmetry breaking remained an important topic, with Rosa et al. (2001); Höfling et al. (2002) studying the universal and critical properties of the Gross-Neveu and Neveu-Yukawa models. Spontaneous ordering in a fermionic system was studied by Baier et al. (2004); Baier et al. (2005), who investigated antiferromagnetism in the two-dimensional repulsive Hubbard model, introducing a bosonic field to take into account the symmetry breaking. Motivated by the same model, Krahl and Wetterich (2007) investigated a system exhibiting d -wave superconductivity. Recently, Schütz et al. (2005) have modified the formalism to emphasize the importance of carefully treating the fermionic degrees of freedom on an equal footing with the bosonic ones. Schütz and Kopietz (2006) provided examples of calculations in phases with symmetry breaking employing this modification.

A number of works which keep the fermionic degrees of freedom while not introducing any additional fields have appeared recently. Several of them are based on Salmhofer (1998b) or Salmhofer and Honerkamp (2001). A series of studies on the repulsive Hubbard model was commenced by Zanchi and Schulz (1998); Halboth and Metzner (2000) finding antiferromagnetism and d -wave superconductivity with different fRG approaches. These works cope with divergent flows arising in the symmetry-broken phase by identifying leadingly divergent couplings and susceptibilities, respectively. Despite these divergencies at a critical scale, a number of insights were gained from this approach also later on. Honerkamp and Salmhofer (2001) employed a temperature flow, focussing on the interplay of ferromagnetism and different types of superconductivity. Honerkamp et al. (2001) discussed the (in)stability of the Fermi liquid in the two-dimensional Hubbard model. Rohe and Metzner (2005) studied the pseudogap phenomenon and the importance of hot spots where the Fermi surface intersects the umklapp surface. Fu et al. (2006) found that introducing phonons into the Hubbard model supports d -density-wave order. Reiss et al. (2007) considered the interplay of antiferromagnetism and d -wave superconductivity by combining the fRG with a mean-field calculation, obtaining quantitative results for the appropriate order parameters. The flow is stopped above the critical scale and an effective model containing

the remaining scales is solved using mean-field theory, thereby sidestepping the divergence. Other recent works have focussed on improving the method itself. Honerkamp et al. (2004) introduced the concept of the interaction flow. Salmhofer et al. (2004); Gersch et al. (2005); Gersch et al. (2006b) focussed on calculations in symmetry-broken regimes and provide the foundation of this thesis. The latter works are based on a modification of the flow equations by Katanin (2004) which improves the fulfillment of Ward identities in fRG flows. If the feedback of the order parameter on the flow of the effective interactions is taken into account, it is finally possible to circumvent the divergence of the flow in the symmetry-broken phase. Thus, systems can be taken into account in their entirety, as has previously only been done in symmetric-phase studies. Two examples of such studies for one-dimensional systems are provided by Enss et al. (2005); Andergassen et al. (2006) investigating universality regimes, conductances, and the Kondo effect in systems with impurities. A brief review on fRG recent work on the two-dimensional repulsive Hubbard model as well as on one-dimensional systems with impurities is provided by Metzner (2005).

Thus reviewing the recent fRG literature, we note that by choosing the *nature of the fields* considered, either keeping the fermionic degrees of freedom or introducing bosonic ones in addition or instead, a study posits itself in the third dimension of the field. This completes our brief overview of the application of the fRG in the study of the behavior of interacting electrons in condensed matter.

1.1.2 Counterterms

Counterterms, the essential idea behind which is to write $0 = a - a$ and to treat one a as an addition to the interacting and the other a as an addition to the noninteracting part of the action, are key to the methodological developments introduced in this work. They have already been employed in fRG calculations before, notably in studies on the symmetric state of interacting electron systems. An early work by Feldman and Trubowitz (1990) considers systems with spherical free Fermi surfaces. Unphysical infrared divergencies of perturbation theory are removed by adjusting the chemical potential on the propagator lines to the interacting Fermi surface, countering this by an appropriate addition to the self-energy. The addition is determined by renormalization-group methods. This procedure can be viewed as a shift from the chemical potential into the interaction. Feldman et al. (1996) employ it for more general Fermi surfaces which necessitate a counterterm that is a function in momentum space. They identify and find bounds for the most singular contributions to this counterterm function under slightly more restrictive conditions in Feldman et al. (1999). The authors prove regularity properties of the counterterm function in Feldman et al. (1998), which they use to study the invertibility of the mapping induced by the counterterm which transforms the interacting to the corresponding free Fermi surface (Feldman et al. (2000)).

Counterterms have also been used in the study of symmetry breaking. The work by Feldman and Trubowitz (1991) is devoted to flows with symmetry-breaking in the Cooper channel for a spherically symmetric electron-phonon system. Coun-

terterms are again used to remove unphysical divergencies as in Feldman and Trubowitz (1990). The self-consistency equation for the superconducting order parameter is recovered as an approximation from the flow. Neumayr and Metzner (2003) study the interplay of d -wave superconductivity and Fermi surface deformations by a counterterm technique. The effective interactions causing the symmetry breaking are constructed order by order in perturbation theory. The counterterm is determined by setting the self-energy on the Fermi surface equal to zero, giving rise to a self-consistency equation. This completes the overview of the use of counterterms with particular emphasis on the fRG and also finishes the discussion of the methodological context.

1.1.3 Hubbard model

One of the simplest models to study interacting electrons is the Hubbard model, originally introduced to study ferromagnetism of itinerant electrons by Hubbard (1963); Kanamori (1963); Gutzwiller (1965). Essentially, the electrons are considered to be located on the sites of a lattice, their ability to transfer from one site to another usually diminishing with increasing distance between the sites, while configurations with two electrons on the same site are either favored or disfavored. The former property sets the itinerant character of the constituent electrons, while the latter determines the interaction. This model exhibits complex behavior far beyond its superficial simplicity. The repulsive version, in which double occupation is disfavored, has drawn considerable attention especially following the conjecture by Anderson (1987) that it explains the phenomenon of superconductivity at very high critical temperatures in certain ceramics (Bednorz and Müller (1986)) if restricted to two dimensions.

The attractive version has similarly been under intense investigation. The qualitative properties are well-understood in certain cases (see Scalettar et al. (1989); Alvarez and González (1998)) and reviewed by Micnas et al. (1990). Important conclusions include that superconductivity arises below a critical temperature. The superconductivity is degenerate with a density-wave order if there is nesting. At weak coupling, results for the order parameter have been obtained by studying perturbation theory up to second order by Martín-Rodero and Flores (1992). At intermediate coupling, Monte Carlo investigations have been employed to study the BCS to Bose-Einstein condensation (BEC) crossover (Singer et al. (1996)) and the pseudogap phenomenon (Randeria et al. (1992); dos Santos (1994)) known from high- T_c superconductivity. T -matrix approaches (Keller et al. (1999)) have also proven fruitful for the study of the BCS to BEC crossover. At strong coupling, Robaszkiewicz et al. (1981) found a way to map the Hubbard model onto an effective anisotropic Heisenberg spin model, from which results could be obtained by mean-field calculations. In the same work, a mapping from the attractive model at arbitrary filling to the repulsive model in a finite magnetic field is introduced. Recent investigations with modern methods have been actuated by the desire to further investigate the pseudogap phenomenon (Rohe and Metzner (2001); Toschi et al. (2005a)), to further study the crossover from BCS to BEC behavior (Toschi

et al. (2005b)), and to test the new methods' capability to study non-mean-field models (Metzner et al. (2006); Strack et al. (2007)). In this work, we study the attractive Hubbard model in the latter spirit.

1.2 In this work

We strive to construct a method which is able to approximate the order parameters associated with a microscopic model including itinerant interacting fermions and external fields, but no disorder. We apply the functional renormalization group (fRG) in the one-particle irreducible (1PI) scheme employing both momentum-shell as well as interaction flow, treating the fermionic degrees of freedom without introducing bosons to prevent bias. If symmetry-breaking – characterized by an order parameter becoming finite – occurs, practical implementations of this method have until recently been plagued by divergencies which make it impossible to obtain quantitative results for the order parameter without employing an additional method (Reiss et al. (2007)). However, Katanin (2004) has found a truncation of the 1PI fRG hierarchy which improves the fulfillment of Ward identities in the flow. Ward identities have also been fruitfully employed by Enss (2005) and in a bosonic RG (Castellani et al. (1997); Pistoiesi et al. (2004)) as well as in a bosonic fRG context (Strack et al. (2007)). Employing Katanin's truncation enabled Salmhofer et al. (2004) to reproduce the exact order parameter of a reduced Bardeen-Cooper-Schrieffer (BCS) model at zero temperature by studying the system in a small external field. Physical divergencies related to the Goldstone mode only appear in the limit of vanishing external field. While curing divergences, this procedure is more difficult compared to its predecessors in two respects. First, there is an increase in analytical complexity, as the feedback of the flow of the order parameter onto the flow of the effective interactions must be taken into account, leading to a propagator with matrix character. Anomalous interactions arise which necessitate additional flow equations. Second, there is an increase in numerical complexity as the integrals which need to be computed in the solution of the flow equations become more difficult to evaluate in the Katanin truncation. This is due to the terms added in the integrands having a larger support in the Brillouin zone as compared to the terms appearing without the Katanin truncation. Also, the increase in analytical complexity discussed above translates directly into an increase in numerical complexity.

The present text builds on the important treatises by Katanin (2004); Salmhofer et al. (2004), as alluded to above. We extend the application of the Katanin-truncated 1PI fRG to the breaking of discrete symmetries and to finite temperatures by studying a reduced charge-density-wave (CDW) model at half filling for which the mean-field solution is exact. The second-order phase transition is captured exactly also by the fRG. The divergence of the effective interaction is curbed in analogy to the case of continuous-symmetry breaking. The key difference lies in the absence of anomalous effective interactions and the absence of massless collective excitations in the CDW case. However, for the momentum-shell flow, the

divergence of the effective interaction is re-encountered at a critical scale if the external field is reduced to zero even away from criticality. This can present a problem for the accuracy of the fRG for more complicated models in the truncation employed here in the following way. Because the truncation neglects terms of order three in the effective interaction for models where mean-field theory is not exact, large effective interactions can be tolerated safely only if they live on a sufficiently small part of the total phase space, e.g. appear only in a thin shell around the Fermi energy and for specific momentum combinations. However, the effective interaction increases with decreasing external field while the shell thickness as well as the momentum combinations involved remain almost constant. Therefore, the contributions neglected for a non-reduced model are bound to become more important for smaller values of the external field. On the other hand, a larger external field implies obtaining results which are further away from the values for spontaneous symmetry breaking at zero external field. Thus, the aims of keeping the effective interaction small during the flow in order to justify the truncation employed and keeping the external field small in order to introduce as small a bias as possible are found to be conflicting. These results have already been published (Gersch et al. (2005)).

The reduced charge-density-wave model is found to exhibit first-order phase transitions in a certain filling range upon varying the temperature or the chemical potential, providing a testbed to study the ability of the method to describe first-order phase transitions. By employing a counterterm and an interaction flow, the Katanin-truncated fRG is proven capable of reproducing the exact results for such transitions in the reduced model independent of the strength of the counterterm: all flows terminate at one of a finite set of strong attractors. The role of counterterms in the renormalization group literature as described above has focussed on the removal of divergencies. In this work, the counterterm serves the purpose of selecting a certain symmetry-broken configuration. It also opens a gap in the spectrum of the system, thereby circumventing even physical divergences until the flow of the non-diverging quantities has saturated. Metastable phases are accessible which cannot be studied using only an external field, as the external field biases the fRG flow towards the stable configuration in the CDW model. As an example illustrating this new-found capability, we study a simple hysteresis phenomenon where it is important to obtain results for both the stable and the metastable configurations. Furthermore, at least away from criticality and for the breaking of a discrete symmetry, the method thus constructed does not lead to a conflict in aims as known from the previous procedure. In fact, it is possible to eliminate all traces of the critical-scale divergence away from criticality if only a discrete symmetry is broken. These results have already been published (Gersch et al. (2006b)).

In order to put this methodological development into a more general framework and in order to introduce the formalism employed in the following study of superconductivity, a generalization of the ideas of Salmhofer and Honerkamp (2001); Katanin (2004); Salmhofer et al. (2004) to the case of general symmetry-breaking

and multiple order parameters is discussed. The idea that symmetry-breaking implies the rise of nonzero expectation values of pairs of fermionic operators which are unpaired in the Hamiltonian is formalized, and the 1PI fRG equations for arbitrary pairings are derived emphasizing their diagrammatic structure. This proves useful for a graphical understanding of the Katanin truncation.

At low temperatures where symmetry breaking occurs, forward scattering processes in which no momentum is transferred between the particles involved are important (Metzner et al. (1998)). To understand the interplay of such processes with the BCS scattering driving superconductivity, we use the formalism taking into account symmetry breaking in a resummation of the perturbation theory for a model incorporating reduced Cooper as well as forward scattering. We show that the resummation solves the model exactly. The combination of scattering processes gives rise to anomalous effective interactions which correspond to operator products of odd numbers of fermion annihilation and creation operators. These anomalous effective interactions are referred to as $3 + 1$, reflecting the number of incoming (outgoing) and outgoing (incoming) legs in a graphical representation. Equivalently, anomalous effective interactions with four incoming legs are referred to as $4 + 0$. Explicit formulas are found for these as well as for the other effective interactions, permitting the study of interdependencies. The resummation scheme is numerically applied to the attractive Hubbard model as an approximation. The effect of the $3 + 1$ on the other effective interactions is found to vary in strength. However, it proves to be small for the effective interactions driving symmetry breaking. Furthermore, including the $3 + 1$ effective interactions does not modify the basic nature of the dispersion relation of the Goldstone mode, as expected. Overall, the qualitative impact of the $3 + 1$ anomalous effective interactions is found to be small.

Concluding the work is the application of both the newly-developed counterterm procedure as well as the procedure employing a small external-field to the superconducting instability of the attractive Hubbard model at zero temperature. The formal framework developed for general symmetry breaking permits the concurrent study of normal and anomalous interactions including those of $3 + 1$ character, fully taking into account their influence on the order parameter. The renormalization procedure is carried out numerically, discretizing the momentum dependence of the effective interactions and self-energies by patching according to Rohe (2005) while dropping the energy dependence. Other patching schemes are considered for example by Zanchi and Schulz (1998); Halboth and Metzner (2000). All these schemes are set up to take into account the parts of the effective interactions driving the symmetry breaking, but also others. The physical result of the calculation is that previous works by Martín-Rodero and Flores (1992); Reiss (2006) studying the influence of fluctuations on the strength of the symmetry breaking are confirmed in their prediction that the order parameter is suppressed to about 50% of its mean-field value at weak coupling. The order parameter exhibits only a negligible momentum dependence. Methodologically, it is found that the fRG flow equations can be integrated completely for the momentum-shell flow

if the external field is large enough. However, large couplings arise in the flow if the discrepancy to results by Martín-Rodero and Flores (1992); Reiss (2006) is to be kept smaller than 20% by reducing the strength of the external field. Fortunately, unphysical divergences are restricted to much smaller values of the external field. The interaction flow is capable of staying in the weak-coupling limit because for the breaking of a continuous symmetry as considered here, the rise of the effective interaction is pushed towards the end of the flow by increasing the counterterm. However, due to the approximative nature of the method in the context of the attractive Hubbard model as well as the systematic errors introduced in the numerical implementation, the counterterm cannot be chosen arbitrarily large. The strong-attractor behavior encountered for the mean-field model is transformed into a clustering of final values for certain counterterm strengths. A final value from this cluster is taken as an approximation for the true value. This is justified by considering the cluster as the analogon of the strong attractor appearing for the reduced CDW model.

This thesis is structured as follows. In chapter 2, the exact temperature and external-field dependence of the order parameter and effective interaction for a reduced charge-density-wave model is obtained for both first- and second-order phase transitions by solving the mean-field equations. Chapter 3 gives a derivation of the 1PI fRG equations, introducing a formalism to take into account symmetry breaking and analyzing diagrammatically the flows generated by applying the Katanin truncation. Chapter 4 treats the charge-density-wave model from chapter 2 with the fRG method from chapter 3, solving the first- and second-order transition problems by introducing a counterterm for the order parameter, and the second-order problem also by introducing a small external field. In chapter 5, the impact of anomalous $3 + 1$ effective interactions is analyzed by employing the formalism for symmetry-breaking in a resummation of perturbation theory. This framework is applied as an approximation to the attractive Hubbard model to study its effective interactions. The chapter culminates in a study of the attractive Hubbard model with the 1PI fRG in the Katanin truncation, studying the suppression of the order parameter below its mean-field value and comparing the counterterm with the external-field flow.

Chapter 2

Charge-density wave: mean-field approach

In this section, we introduce the concept of a phase transition following section 4.1 of Negele and Orland (1998). We discuss and solve models exhibiting phase transitions, which serve as benchmark models for our renormalization-group methods.

By definition, a phase transition of a physical system occurs if its parameters pass from a region where a locally measurable observable, for example a spectral gap or the magnetization, assumes finite values to a region where it is zero (or infinite). Said locally measurable observable is called the order parameter of the phase transition, while the parameter value separating the two parameter regions is called critical. The transition is said to be of second order if the dependence of the order parameter on the physical parameter which is changed is continuous in the critical region. If there is an isolated discontinuity of the order parameter at the critical parameter, the transition is considered to be of first order. We will study examples of both types of transitions in this section.

2.1 Second-order phase transitions

We commence with the second-order case as it presents a slightly reduced challenge. This is because due to the continuity condition, a relevant minimum of the thermodynamic potential as a function of the order parameter is always found starting at a small order parameter value.

2.1.1 Model

We introduce a model exhibiting the spontaneous formation of a charge-density wave, which we will use as example and benchmark for our renormalization group calculations. The phase transition in this model is of second order. We combine this introduction with a qualitative discussion. Furthermore, several formal conventions are fixed.

We consider spinless fermions on a d -dimensional hyper-cubic lattice with N sites labeled by \mathbf{x} . The kinetic energy is given by a tight-binding dispersion with nearest-neighbor hopping amplitude t . We also assume a repulsive nearest-neighbor density-density interaction V_0 . The Hamiltonian reads

$$H = -t \sum_{\mathbf{x}, \mathbf{n}} (c_{\mathbf{x}}^\dagger c_{\mathbf{x}+\mathbf{n}} + h.c.) + V_0 \sum_{\mathbf{x}, \mathbf{n}} c_{\mathbf{x}}^\dagger c_{\mathbf{x}} c_{\mathbf{x}+\mathbf{n}}^\dagger c_{\mathbf{x}+\mathbf{n}}. \quad (2.1)$$

The sum over \mathbf{n} runs over the d unit vectors of the d -dimensional hypercubic lattice with lattice constant set to one. We assume half filling with an average of one particle per two lattice sites, $\langle n_{\mathbf{x}} \rangle = 1/2$. The nearest-neighbor density-density repulsion favors a charge-density wave (CDW), i.e. a periodic arrangement of the particles in which the probability of two particles being nearest neighbors is reduced. This tendency competes with the hopping term, which decreases with increasing homogeneity of the electron distribution, and with the entropy, which increases when this homogeneity is increased.

In the case where a CDW is formed with a fixed modulation amplitude n_{CDW} , the charge density $\langle n_{\mathbf{x}} \rangle$ takes only two values, $1/2 + n_{\text{CDW}}$ on a given site and $1/2 - n_{\text{CDW}}$ on each adjacent site. Therefore, the half-filled CDW state breaks a discrete Ising-type symmetry, where there are two distinct ordered states. While in one dimension such order can only occur in the ground state, in two and higher dimension it is possible to have a nonzero critical temperature T_c .

For any band filling which is not a rational number, a CDW with an incommensurate modulation wave-vector generates infinitely many different density values on the lattice sites. The lattice sites sample an oscillation which is incommensurate with their spacing, so the density on a given lattice site does not repeat on a different lattice site. The possible values form a continuum, and when this symmetry is broken, at a given lattice site one of the values is assumed. Hence, a continuous symmetry is broken.

Continuing with the half-filled case, we Fourier-transform the Hamiltonian using

$$c_{\mathbf{x}} = \frac{1}{\sqrt{N}} \sum_{\mathbf{k}} e^{i\mathbf{k}\mathbf{x}} c_{\mathbf{k}} \quad (2.2)$$

and obtain

$$H = -2t \sum_{\mathbf{k}} L(\mathbf{k}) c_{\mathbf{k}}^\dagger c_{\mathbf{k}} + \frac{V_0}{N} \sum_{\mathbf{k}_1, \mathbf{k}_2, \mathbf{q}} L(\mathbf{q}) c_{\mathbf{k}_1}^\dagger c_{\mathbf{k}_1 - \mathbf{q}} c_{\mathbf{k}_2}^\dagger c_{\mathbf{k}_2 + \mathbf{q}}, \quad (2.3)$$

where we have introduced $L(\mathbf{k}) = \sum_{i=1}^d \cos(k_i)$. Abbreviating the dispersion $\varepsilon(\mathbf{k}) = -2t \sum_{i=1}^d \cos(k_i) = -2tL(\mathbf{k})$, we note that the nesting condition $\varepsilon(\mathbf{k}) = -\varepsilon(\mathbf{k} + \mathbf{Q})$ is fulfilled for the wave-vector $\mathbf{Q} = (\pi, \dots, \pi)$. This causes a divergence of the non-interacting charge response at the nesting wave-vector for $T \rightarrow 0$. If

the interactions are treated in the random phase approximation, the charge response at \mathbf{Q} actually diverges at a finite temperature, giving an estimate of T_c for the charge-density wave formation. In a mean-field treatment of the symmetry-breaking in which the interaction term is decoupled with an alternating charge density, anomalous particle-hole pairing expectation values $\langle c_{\mathbf{k}+\mathbf{Q}}^\dagger c_{\mathbf{k}} \rangle$ arise below the transition temperature.

Although this physical picture of a CDW transition is essentially correct regarding the ground state properties, the model (2.3) has not been solved exactly. However, by a reduction of the interaction keeping only processes that change both particle's momenta by \mathbf{Q} ,

$$H_{\text{red}} = \sum_{\mathbf{k}} \varepsilon(\mathbf{k}) c_{\mathbf{k}}^\dagger c_{\mathbf{k}} - \frac{V_0}{N} \sum_{\mathbf{k}_1, \mathbf{k}_2} c_{\mathbf{k}_1}^\dagger c_{\mathbf{k}_1 - \mathbf{Q}} c_{\mathbf{k}_2}^\dagger c_{\mathbf{k}_2 + \mathbf{Q}}, \quad (2.4)$$

we obtain a solvable model, as we show below. Intuitively put, this is because in (2.4) the interaction between fermions on the lattice sites \mathbf{x} and \mathbf{x}' corresponds to an infinite range density-density interaction with oscillating sign,

$$-V_0 N^{-1} \cos[\mathbf{Q}(\mathbf{x} - \mathbf{x}')] n_{\mathbf{x}} n_{\mathbf{x}'}$$

The infinite range already suggests that mean-field theory could be exact because each particle is acted upon equally strongly by all the other particles.

We show in 2.1.2 that as in the reduced BCS pairing model (Mühschlegel (1962)), mean-field theory actually is exact for the reduced model (2.4) in the thermodynamic limit $N \rightarrow \infty$. Instead of the BCS case's superconducting state, there is a CDW ordered state below a critical $T_c > 0$ in any dimension d . For the half-filled commensurate case, there are two distinct degenerate symmetry-broken configurations and the electronic order parameter n_{CDW} is real.

For convenience in our analytic considerations and because it is essential for the renormalization group calculations, we include a real external field $\Delta_{\text{ext}} \cos(\mathbf{Q}\mathbf{x})$ coupling to particle-hole pairs $c_{\mathbf{k}}^\dagger c_{\mathbf{k}+\mathbf{Q}}$ and $c_{\mathbf{k}+\mathbf{Q}}^\dagger c_{\mathbf{k}}$ which lifts the degeneracy of the ordered states by explicitly breaking the translational symmetry of the original Hamiltonian (2.4). In momentum space, this term couples to pairs of particles whose momenta differ by $\mathbf{Q} = (\pi, \dots, \pi)$. If Δ_{ext} is very small compared to all other relevant energy scales, it does not change macroscopic observables away from the critical temperature. However, it allows us to integrate the RG differential equations over all scales without encountering divergences. The Hamiltonian including the external field reads

$$H_{\text{red}} = H_{\text{kin}} + \sum_{\mathbf{k}} \Delta_{\text{ext}} c_{\mathbf{k}}^\dagger c_{\mathbf{k}+\mathbf{Q}} - \frac{V_0}{N} \sum_{\mathbf{k}_1, \mathbf{k}_2} c_{\mathbf{k}_1}^\dagger c_{\mathbf{k}_1 + \mathbf{Q}} c_{\mathbf{k}_2}^\dagger c_{\mathbf{k}_2 - \mathbf{Q}}. \quad (2.5)$$

We introduce a frequency-space field-integral representation in the usual way. Writing T for temperature, we define the fermionic Matsubara frequencies $\omega_j := (2j + 1)\pi T$ and obtain Grassmann fields $\psi_{\mathbf{k},\omega_n}, \bar{\psi}_{\mathbf{k},\omega_n}$. Introducing the Nambu-like notation

$$\begin{aligned}\bar{\Psi}_{\mathbf{k},\omega_n} &= \begin{pmatrix} \bar{\psi}_{\mathbf{k},\omega_n} \\ \bar{\psi}_{\mathbf{k}+\mathbf{Q},\omega_n} \end{pmatrix}, \\ \bar{\Psi}_{\mathbf{k}+\mathbf{Q},\omega_n} &= \begin{pmatrix} \bar{\psi}_{\mathbf{k},\omega_n} & \bar{\psi}_{\mathbf{k}+\mathbf{Q},\omega_n} \end{pmatrix},\end{aligned}$$

the partition function reads

$$\begin{aligned}\mathcal{Z} = \int \mathcal{D}(\bar{\psi}, \psi) \exp &\left[-\frac{1}{2}T \sum_{n,\mathbf{k}} \bar{\Psi}_{\mathbf{k},\omega_n} \mathbb{Q}(\varepsilon_{\mathbf{k}}, \omega_n) \Psi_{\mathbf{k},\omega_n} \right. \\ &\left. - V_0 \frac{T^3}{N} \sum_{\substack{n_1, n_2, n_3 \\ \mathbf{k}_1, \mathbf{k}_2}} \bar{\psi}_{\mathbf{k}_1, \omega_{n_1}} \psi_{\mathbf{k}_1 + \mathbf{Q}, \omega_{n_3}} \bar{\psi}_{\mathbf{k}_2, \omega_{n_2}} \psi_{\mathbf{k}_2 - \mathbf{Q}, \omega_4} \right].\end{aligned}\quad (2.6)$$

Here, $\omega_4 = \omega_{n_1+n_2-n_3}$ and

$$\mathbb{Q}(\varepsilon_{\mathbf{k}}, \omega_n) = \begin{pmatrix} i\omega_n - \varepsilon_{\mathbf{k}} & -\Delta_{\text{ext}} \\ -\Delta_{\text{ext}} & i\omega_n + \varepsilon_{\mathbf{k}} \end{pmatrix} \quad (2.7)$$

(see e.g. Lee et al. (1974)). The minus sign in front of the second ε arises from the \mathbf{Q} -anti-periodicity of the cosine. The doubling of the number of degrees of freedom by introducing the Nambu notation is compensated by the 1/2 in front of the quadratic part of the action. Due to the explicit symmetry breaking, there is a nonzero off-diagonal component in the propagator. The method of treating symmetry breaking by formally accounting twice for the degrees of freedom is generalized in section 3.1. If we apply mean-field theory by decoupling the interaction term in the CDW channel, the CDW order parameter due to the interaction, $\Delta_{\text{i.a.}}$, will add to Δ_{ext} .

2.1.2 Mean-field solution and resummation

We would like to gain a quantitative understanding of the model (2.4) to facilitate its employment as a benchmark for the renormalization group calculations. To this end, we resum the perturbation expansions for the self-energy and the effective interaction in the thermodynamic limit $N \rightarrow \infty$ in this section. For our model, this is equivalent to mean-field theory in the CDW amplitude with modulation wave-vector \mathbf{Q} . This statement is proven in the context of first-order phase transitions in section 2.2.2.

Due to the explicit symmetry breaking with $\Delta_{\text{ext}} \neq 0$ there is a nonzero frequency independent off-diagonal propagator which scatters a fermion with wave-vector \mathbf{k} to $\mathbf{k} + \mathbf{Q}$ and vice versa. Therefore, besides normal (diagonal) wave-vector conserving propagators, also anomalous (off-diagonal) propagators appear in the

diagrams of perturbation theory. On a one-particle level, the interaction causes the occurrence of an off-diagonal self-energy $\Delta_{i.a.}$ supplementing Δ_{ext} from the non-interacting propagator (2.7). In the following, we determine $\Delta_{i.a.}$ as well as the effective interaction V .

We reason hereafter that the special momentum structure of the bare interaction reduces the diversity of the diagrams contributing to the perturbation expansion of the effective interaction, similarly as in Gaudin (1960); Langer (1964). We note that the interaction term in (2.5) includes a prefactor $1/N$, contributing a factor $1/N^2$ to all second-order diagrams in the expansion in the bare interaction strength,

$$\boxed{\text{hatched}} \approx \text{brace} + \text{circle} + \text{rectangle} + \text{half-circle}.$$

From the left-hand side of the equation in Fig. 2.1(b), this same prefactor brings

$$\begin{aligned} \text{(a) } \text{hatched circle} &= \text{circle} + \text{circle} + \text{circle} + \dots \\ &= \text{circle} + \text{hatched circle} = \text{circle} \\ \text{(b) } \boxed{\text{hatched}} &= \text{brace} + \text{circle} + \text{circle} + \dots = \text{brace} + \text{circle} \end{aligned}$$

Figure 2.1: Resummation of the perturbation expansion of the reduced charge-density-wave model: (a) self-energy (hatched circle) and (b) effective interaction (hatched rectangle). Undirected internal lines carry a summation over their Nambu-like indices in addition to the frequency summation and momentum integration. Double-arrowed lines correspond to off-diagonal propagator elements, bold lines to full and thin lines to bare propagators.

a factor N . For there to remain a finite contribution from a given second-order diagram in the thermodynamic limit $N \rightarrow \infty$, the internal lines must be of order N . However, in all second order diagrams except the one also depicted in Fig. 2.1(b), the restricted momentum structure of the interaction implies that the internal momentum is fixed by an external momentum, leaving only a single term from the trace implied by the diagram. Hence, the contribution of such a diagram is $O(1/N)$ and vanishes for $N \rightarrow \infty$. The diagram depicted retains one summation over all degrees of freedom in spite of the bare interaction's restricted

momentum structure, yielding a finite contribution in the thermodynamic limit. These arguments can be iterated to arbitrary order in the bare interaction, showing that only diagrams retaining one integration per each interaction line beyond the first contribute in the thermodynamic limit. Therefore, only the bubble chains indicated in Fig. 2.1(b) contribute to the perturbation expansion of the effective interaction. The derivation of the formula in Fig. 2.1(b) is concluded by noting that repeated substitution of the right-hand side for the hatched rectangle in the right-most diagram yields the perturbation series we derived above.

Next, we discuss the possible rise of anomalous effective interactions as known from the BCS case (see section 5.1 or Salmhofer et al. (2004)). Since each bubble in the diagrams remaining in the thermodynamic limit transfers a momentum \mathbf{Q} due to the special structure of the bare interaction, only effective interaction processes with a momentum transfer of \mathbf{Q} exist. In particular, no effective interactions violating the translation symmetry are generated. This is different for incommensurate charge-density waves, where pairs of internal anomalous propagators add even multiples of the incommensurate charge-density wave vector to the total incoming momentum, generating effective interactions which violate momentum conservation. In the half-filled case, any even multiple of the charge-density wave vector is an integer multiple of $2\mathbf{Q} = (2\pi, \dots, 2\pi)$, and thus equivalent to zero.

We discuss the perturbation theory for the self-energy in order to determine $\Delta_{i.a.}$. In Fig. 2.1(a) we show the perturbation expansion for the off-diagonal self-energy. Due to the same arguments as for the expansion of the effective interaction, only diagrams which retain one momentum integration per interaction line contribute in the thermodynamic limit. Therefore, in the thermodynamic limit only diagrams constructed by forming trees of tadpole diagrams – depicted in the first equality of Fig. 2.1(a) – contribute. This implies that the normal diagonal self-energy vanishes in the thermodynamic limit since a tadpole diagram will always transfer a momentum \mathbf{Q} through its base if the interaction is nonzero only for this momentum transfer. This allows us to note the full propagator \mathbb{G} as an aside:

$$\mathbb{G}(i\omega_n, \varepsilon_{\mathbf{k}}) = \frac{1}{\omega_n^2 + \varepsilon_{\mathbf{k}}^2 + (\Delta_{\text{ext}} + \Delta_{i.a.})^2} \begin{pmatrix} -i\omega_n - \varepsilon_{\mathbf{k}} & -\Delta_{i.a.} - \Delta_{\text{ext}} \\ -\Delta_{i.a.} - \Delta_{\text{ext}} & -i\omega_n + \varepsilon_{\mathbf{k}} \end{pmatrix}. \quad (2.8)$$

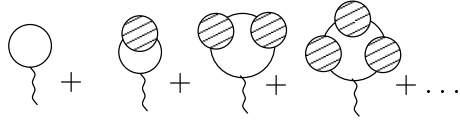
By substituting the diagrammatic form

$$\text{---} = \text{---} + \text{---} \circlearrowleft + \text{---} \circlearrowleft \circlearrowleft + \dots$$

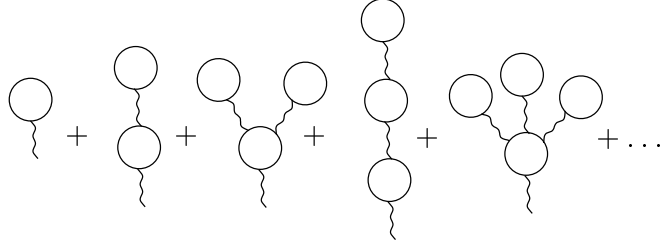
of the geometric series expansion of the Dyson equation into

$$\text{---} \circlearrowleft + \text{---} \circlearrowleft \circlearrowleft$$

from Fig. 2.1(a), we obtain



By repeated substitution of this expansion for the hatched circles included in itself, we recover



which we recognize from the first line of Fig. 2.1(a), explaining the figure's second equality. The diagrammatic form

$$\text{---} = \text{---} + \text{---} \text{---} \text{---}$$

of the Dyson equation justifies the last equality, albeit without the arrows. They appear since if a tadpole diagram is not connected to other tadpole diagrams, only the terms off-diagonal in the Nambu-like space are non-vanishing. This is because the outgoing momentum of such an off-diagonal line equals the incoming momentum plus \mathbf{Q} , which is compatible with the reduced momentum structure of the interaction. The exact resummation thus derived is equivalent to self-consistent Hartree-Fock theory of which the Fock contributions vanish in the thermodynamic limit. This is equivalent to the statement that Hartree mean-field theory is exact for this model.

With the aid of (2.8), we symbolically evaluate in the following the diagrammatic equations obtained above. We assume the density of states to be constant over the Brillouin zone and equal to its value at the Fermi energy to remove dimension-specific effects. Evaluating Fig. 2.1(a) and denoting the self-energy due to the interaction by $\Delta_{\text{i.a.}}$, the band edge by W , the density of states at the Fermi energy ρ_0 , the Fermi distribution $f(x) := (1 + \exp(x/T))^{-1}$, $\Sigma := \Delta_{\text{i.a.}} + \Delta_{\text{ext}}$ as well as $E := \sqrt{\varepsilon^2 + \Sigma^2}$, we obtain the gap equation (compare e.g. Rice and Strässler (1973))

$$\begin{aligned} \Sigma - \Delta_{\text{ext}} &= V_0 T \sum_n \rho_0 \int_{-W}^W d\varepsilon \frac{\Sigma}{\omega_n^2 + E^2} \\ &= V_0 \Sigma \rho_0 \int_0^W d\varepsilon \frac{\tanh(E/2T)}{E}, \end{aligned} \quad (2.9)$$

where we have used (B.6). We have also assumed a flat density of states $\rho(\varepsilon) \equiv \rho_0$. (2.9) resembles the BCS (Bardeen et al. (1957)) and excitonic insulator (J erome

et al. (1967)) gap equations. If we set $T = \Delta_{\text{ext}} = 0$, solving (2.9) analytically yields (compare e.g. Bardeen et al. (1957); Grüner and Zettl (1985))

$$\Sigma = 2t \frac{1}{\sinh(1/V_0 \rho_0)} \stackrel{V_0 \rho_0 \ll 1}{\approx} 4t \exp\left(-\frac{1}{V_0 \rho_0}\right). \quad (2.10)$$

Similar equations are found in the BCS theory for superconductors (Bardeen et al. (1957)).

We turn to the effective interaction with zero frequency transfer. As argued above, only fermionic bubbles contribute in the thermodynamic limit $N \rightarrow \infty$. In the notation, we omit the arguments of the hyperbolic functions originating from the Fermi distribution from now on: they are always $E/2T$. We abbreviate the bubble integral

$$\begin{aligned} B &:= -\text{Tr}(\mathbb{G}(i\omega_n, \varepsilon_{\mathbf{k}})\mathbb{G}(i\omega_n, \varepsilon_{\mathbf{k}+\mathbf{Q}})) \\ &= T \sum_{\omega_n} \rho_0 \int_W \frac{\omega_n^2 + \varepsilon^2 - \Sigma^2}{(\omega_n^2 + E^2)^2} \end{aligned} \quad (2.11)$$

$$= \rho_0 \int_0^W \frac{d\varepsilon}{E^2} \left[\frac{\Sigma^2}{2T} \cosh^{-2} + \frac{\varepsilon^2}{E} \tanh \right], \quad (2.12)$$

where we have used $\varepsilon_{\mathbf{k}+\mathbf{Q}} = -\varepsilon_{\mathbf{k}}$ for the first and (B.3) and (B.4) for the second equality. The evaluation of Fig. 2.1(b) yields

$$V = \frac{V_0}{1 - V_0 B}. \quad (2.13)$$

If $\Delta_{\text{ext}} = 0$, we can define the critical temperature T_c via the condition that $1 = V_0 B(T_c)$, i.e. that the denominator of (2.13) vanishes and V diverges. By analyzing (2.12) we note that this criterion for T_c coincides with the temperature below which we can find a nonzero solution of the gap equation (2.9). For small V_0 and $\Sigma = 0$ we find $1.76T_c \approx 4t \exp(-1/V_0 \rho_0) \approx \Sigma(T = 0)$ (see e.g. Grüner and Zettl (1985)). This is true when the approximation in (2.10) is valid. This concludes the analytical treatment of (2.5).

2.1.3 Dimensionless example

As a finite Δ_{ext} allows us to integrate the renormalization group equations over all scales as we see in section 4.1, we are interested in the dependence of the mean-field solutions (2.9) and (2.13) on Δ_{ext} . In particular, we illustrate in the following where the system including a finite symmetry-breaking field (2.5) is practically indistinguishable from the system without symmetry-breaking field, (2.4). To this end, we show in the upper part of Fig. 2.2 convergence of $\Sigma^{\Delta_{\text{ext}}}(T)$ to $\Sigma(T)$ for $\Delta_{\text{ext}} \rightarrow 0$. The convergence is worst in the vicinity of a kink that can be discerned at $T \approx 0.1t$ in the graph for $\Delta_{\text{ext}} = 0$. As an aside, we note that the continuity of the graph of $\Sigma(T)$ is the hallmark of a second-order phase transition according to our definition at the beginning of section 2. We would like to be more

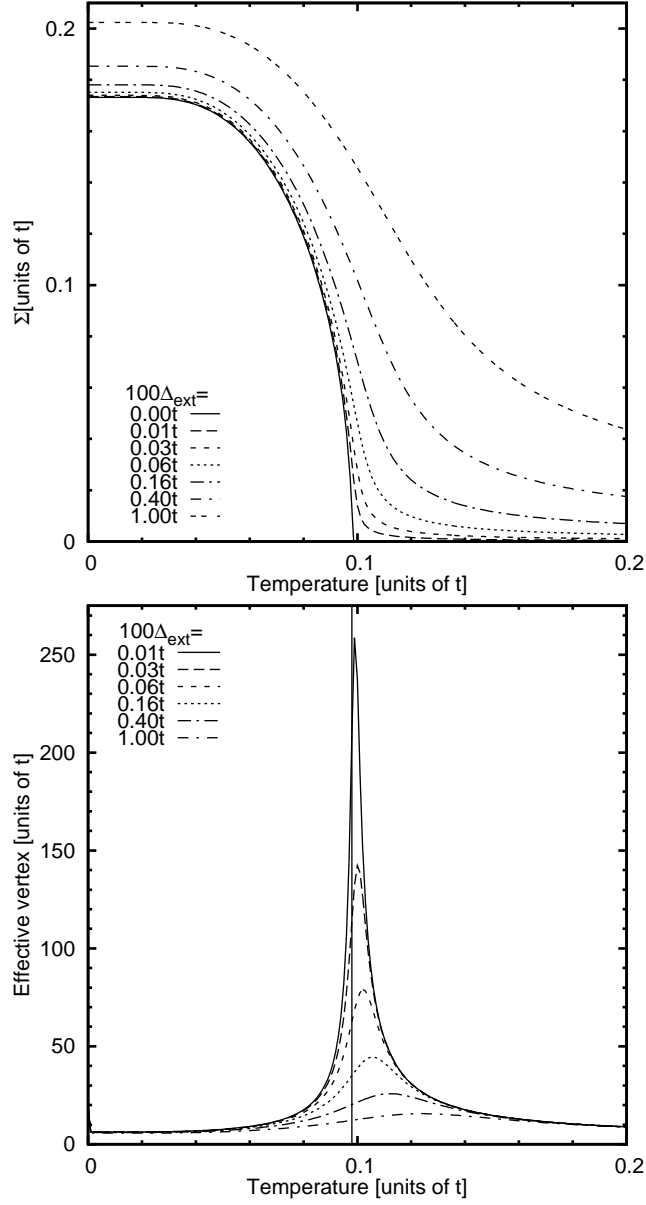


Figure 2.2: (top) Solutions $\Sigma(T)$ of the gap equation for $V_0 = 2t$ and small to intermediate initial self-energies Δ_{ext} . (bottom) Temperature dependence of the effective interactions calculated by resumming the perturbation expansion for $V_0 = 2t$ and small to intermediate initial self-energy. $\rho_0 = 1/2\pi$, $W = 2$

concrete about the temperature range in which the system including a symmetry-breaking field can be used to approximate the system without symmetry-breaking field. To this end, we consider the dependence of the effective interaction on both temperature and the symmetry-breaking field as plotted in the lower part of Fig. 2.2. Its singularity is regularized by a nonzero Δ_{ext} which cuts off the integrand of the bubble integral (2.12). The figure also shows a strong suppression of the effective interaction peak with increasing Δ_{ext} . Its location converges to T_c from above for $\Delta_{\text{ext}} \rightarrow 0$. In the figure, we also spot convergence of $V^{\Delta_{\text{ext}}}(T)$ to $V(T)$ for $T \ll T_c$ and $T \gg T_c$. We see that $V^{\Delta_{\text{ext}}}(T) \approx V(T)$ if T is outside the double width at half maximum of $V^{\Delta_{\text{ext}}}(T)$. If T is outside said width and also below T_c , we learn from the upper part of the figure that $\Sigma^{\Delta_{\text{ext}}}(T) \approx \Sigma(T)$. This is thus the temperature region in which the initial symmetry-breaking field does not appreciably change the physics.

This concludes our study of the second-order phase transition in the reduced CDW model. We have exactly solved the model using mean-field theory, determining the CDW amplitude as an anomalous self-energy as well as the effective interaction at zero energy transfer. We have gauged the impact of an external symmetry-breaking field on the results.

2.2 First-order phase transitions

The first-order case presents a subtly elevated challenge as compared to the second-order case. As there is no continuity condition, scans of the order parameter space are necessary. A main result of this thesis is the development of a procedure – which is presented in section 4.2 – to deal with these scans in the framework of the functional renormalization group. In this section, we solve a model to serve as a benchmark for this method.

2.2.1 Model

We modify the Hamiltonian (2.5) to include a chemical potential μ which allows us to vary our system's filling:

$$\begin{aligned}
 H_{\text{red}} = & \sum_{\mathbf{k}} \xi(\mathbf{k}) c_{\mathbf{k}}^{\dagger} c_{\mathbf{k}} - \frac{V_0}{N} \sum_{\mathbf{k}_1, \mathbf{k}_2} c_{\mathbf{k}_1}^{\dagger} c_{\mathbf{k}_1 + \mathbf{Q}} c_{\mathbf{k}_2}^{\dagger} c_{\mathbf{k}_2 - \mathbf{Q}} \\
 & + \sum_{\mathbf{k}} (\Delta_{\text{ext}} + \Sigma_i - \Delta_c) c_{\mathbf{k}}^{\dagger} c_{\mathbf{k} + \mathbf{Q}}, \tag{2.14}
 \end{aligned}$$

where $\xi(\mathbf{k}) := \varepsilon(\mathbf{k}) - \mu$. The chemical potential can be adjusted to produce a system exhibiting a first-order phase transition. The dispersion fulfills the nesting relation $\varepsilon(\mathbf{k}) = -\varepsilon(\mathbf{k} - \mathbf{Q})$. For $V_0 > 0$ the interaction term can lead to charge-density-wave ordering with wavevector \mathbf{Q} , as discussed in section 2.1.2. The same two-sublattice charge modulation is induced by the last term, which breaks the translational symmetry of the Hamiltonian by coupling a field alternating in space to the fermion density.

Note that the external-field part of the Hamiltonian has been blown up in comparison to (2.5) to include an initial self-energy Σ_i and a counter term Δ_c . In the fRG treatment, Σ_i will be used as the initial condition for the off-diagonal self-energy. The counterterm Δ_c will be included in the bare propagator to prevent this from affecting the physics of the system. Setting $\Sigma_i = \Delta_c$ guarantees a cancellation at the end of the fRG flow, and allows us to produce results at zero external field by setting $\Delta_{\text{ext}} = 0$. Δ_{ext} is no longer necessary for the fRG flows, but allows us to study the effect of an external field and hysteresis phenomena.

2.2.2 Mean-field treatment

The physical properties of the model for $(\Delta_{\text{ext}} + \Sigma_i - \Delta_c) = 0$ depend on the chemical potential μ . As discussed in 2.1.2, at half-filling ($\mu = 0$), the Fermi surface exhibits nesting and an exact resummation of perturbation theory, equivalent to a mean-field treatment, finds a second-order phase transition toward the charge-density-wave state at a critical temperature T_c . In this ordered state, $\tilde{\Delta}_{\text{i.a.}} := \frac{V_0}{N} \sum_{\mathbf{k}} \langle c_{\mathbf{k}}^\dagger c_{\mathbf{k}+\mathbf{Q}} \rangle$ is nonzero. This second-order mean-field transition vanishes if μ is chosen large compared to $T_c(\mu = 0)$. In this case, the symmetric configuration will appear stable when considering only a sufficiently small vicinity of $\Delta_{\text{i.a.}} = 0$. A more complete scan of the order parameters space, however, reveals global minima of the thermodynamic potential at finite $\Delta_{\text{i.a.}}$ for temperatures below a threshold T_t . These minima develop independently of the minimum at zero order parameter as the temperature is lowered. In such a situation, the system's stable configuration changes from symmetric with $\Delta_{\text{i.a.}} = 0$ to symmetry-broken with $\Delta_{\text{i.a.}} \neq 0$ discontinuously upon lowering the temperature below T_t . This phenomenon is the defining property of a first-order phase transition. The $\mu - T$ phase diagram for the Hamiltonian (2.14) is shown in Fig. 2.3. The $T = 0$ ther-

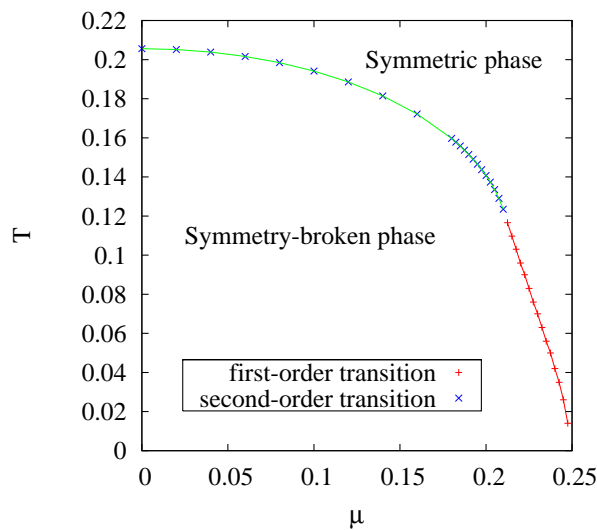


Figure 2.3: μ - T phase diagram of (2.14) for $V_0 = 2.0t$.

modynamic potentials as functions of $\Delta_{i.a.}$ described above are shown in Fig. 2.6 for $\mu = 0$ and both for first-order and second-order cases with $\mu \neq 0$.

To understand how such a simple model can have a first-order transition, we derive the gap equation from Fig. 2.1(a) as in (2.9). From the quadratic part of the action

$$\mathbb{Q}(i\omega_n, \varepsilon) = \begin{pmatrix} i\omega_n - \varepsilon_{\mathbf{k}} + \mu & -\Delta_{\text{ext}} - \Sigma_i + \Delta_c \\ -\Delta_{\text{ext}} - \Sigma_i + \Delta_c & i\omega_n + \varepsilon_{\mathbf{k}} + \mu \end{pmatrix}, \quad (2.15)$$

which is derived from (2.7) by including μ and supplementing Δ_{ext} with $\Sigma_i - \Delta_c$, we obtain the propagator as a function of Matsubara frequencies ω_n and kinetic energies $\varepsilon_{\mathbf{k}}$

$$\mathbb{G}(i\omega_n, \varepsilon_{\mathbf{k}}) = \frac{1}{-(i\omega_n + \mu)^2 + E_{\mathbf{k}}^2} \begin{pmatrix} -i\omega_n - \varepsilon_{\mathbf{k}} - \mu & -\Delta_{\text{eff}} \\ -\Delta_{\text{eff}} & -i\omega_n + \varepsilon_{\mathbf{k}} - \mu \end{pmatrix}, \quad (2.16)$$

where we have abbreviated $\Delta_{\text{eff}} := \Delta_{i.a.} + \Delta_{\text{ext}} + \Sigma_i - \Delta_c$ and $E := \sqrt{\varepsilon^2 + \Delta_{\text{eff}}^2}$ in parallel to our conventions in (2.9). Evaluating the diagrams in Fig. 2.1(a) yields

$$\begin{aligned} \Delta_{\text{eff}} - \Delta_{\text{ext}} - \Sigma_i + \Delta_c &= \frac{V_0 T}{N} \sum_{\omega_n, \mathbf{k}} \frac{\Delta_{\text{eff}}}{-(i\omega_n + \mu)^2 + E_{\mathbf{k}}^2} \\ &= \frac{V_0 T}{N} \sum_{\omega_n, \mathbf{k}} \frac{\Delta_{\text{eff}}}{\omega_n^2 - 2i\mu\omega_n - \mu^2 + E_{\mathbf{k}}^2} \\ &= \frac{V_0 T}{N} \sum_{\omega_n, \mathbf{k}} \frac{\Delta_{\text{eff}}}{\omega_n^2 + i(E_{\mathbf{k}}^+ + E_{\mathbf{k}}^-)\omega_n - E_{\mathbf{k}}^+ E_{\mathbf{k}}^-} \\ &= \frac{V_0}{N} \sum_{\mathbf{k}} \frac{\Delta_{\text{eff}}}{(E_{\mathbf{k}}^+ - E_{\mathbf{k}}^-)} (f(E_{\mathbf{k}}^-) - f(E_{\mathbf{k}}^+)), \end{aligned} \quad (2.17)$$

where the dispersion relation $E^\pm := \pm E - \mu$ is introduced in the third equality and the Matsubara sum is evaluated according to (B.14) in the last line.

To facilitate the arguments in this section, we show that the gap equation can also be obtained from the variational condition that the grand canonical potential Ω be minimal if the two-particle interaction is mean-field decoupled in an appropriate channel. To this end, we study the partition function

$$\mathcal{Z} = \text{Tr} \exp(T^{-1} H_{\text{red}}) \quad (2.18)$$

of (2.14) without introducing field integrals and decouple the interaction term of

H_{red} into

$$\begin{aligned}
 & \frac{V_0}{N} \sum_{\mathbf{k}_1, \mathbf{k}_2} c_{\mathbf{k}_1}^\dagger c_{\mathbf{k}_1+\mathbf{Q}} c_{\mathbf{k}_2}^\dagger c_{\mathbf{k}_2+\mathbf{Q}} \\
 &= \frac{V_0}{N} \sum_{\mathbf{k}_1, \mathbf{k}_2} \left[\left(c_{\mathbf{k}_1}^\dagger c_{\mathbf{k}_1+\mathbf{Q}} - \langle c_{\mathbf{k}_1}^\dagger c_{\mathbf{k}_1+\mathbf{Q}} \rangle \right) \left(c_{\mathbf{k}_2}^\dagger c_{\mathbf{k}_2+\mathbf{Q}} - \langle c_{\mathbf{k}_2}^\dagger c_{\mathbf{k}_2+\mathbf{Q}} \rangle \right) \right. \\
 & \quad \left. + 2 \left(c_{\mathbf{k}_1}^\dagger c_{\mathbf{k}_1+\mathbf{Q}} \langle c_{\mathbf{k}_2}^\dagger c_{\mathbf{k}_2+\mathbf{Q}} \rangle \right) - \left(\langle c_{\mathbf{k}_1}^\dagger c_{\mathbf{k}_1+\mathbf{Q}} \rangle \langle c_{\mathbf{k}_2}^\dagger c_{\mathbf{k}_2+\mathbf{Q}} \rangle \right) \right] \\
 & \approx \sum_{\mathbf{k}_1} 2\tilde{\Delta}_{\text{i.a.}} c_{\mathbf{k}_1}^\dagger c_{\mathbf{k}_1+\mathbf{Q}} - \frac{N\tilde{\Delta}_{\text{i.a.}}^2}{V_0}, \tag{2.19}
 \end{aligned}$$

where we have neglected the term quadratic in the fluctuations in the approximation in the last line, and abbreviated $\tilde{\Delta}_{\text{i.a.}} = \frac{V_0}{N} \sum_{\mathbf{k}} \langle c_{\mathbf{k}}^\dagger c_{\mathbf{k}+\mathbf{Q}} \rangle$ as above. Plugging the decoupling (2.19) into the partition function (2.18), we obtain

$$\begin{aligned}
 \mathcal{Z}^{\text{MF}} &= \text{Tr} \exp \left[\frac{1}{T} \sum_{\mathbf{k}} \left(\xi_{\mathbf{k}} c_{\mathbf{k}}^\dagger c_{\mathbf{k}} + \Delta_{\text{eff}} c_{\mathbf{k}}^\dagger c_{\mathbf{k}+\mathbf{Q}} \right) + \frac{N\tilde{\Delta}_{\text{i.a.}}^2}{TV_0} \right] \\
 &= \text{Tr} \exp \left[\frac{1}{2T} \sum_{\mathbf{k}} \begin{pmatrix} c_{\mathbf{k}}^\dagger & c_{\mathbf{k}+\mathbf{Q}}^\dagger \end{pmatrix} \begin{pmatrix} \varepsilon_{\mathbf{k}} - \mu & \Delta_{\text{eff}} \\ \Delta_{\text{eff}} & -\varepsilon_{\mathbf{k}} - \mu \end{pmatrix} \begin{pmatrix} c_{\mathbf{k}} \\ c_{\mathbf{k}+\mathbf{Q}} \end{pmatrix} + \frac{N\tilde{\Delta}_{\text{i.a.}}^2}{TV_0} \right] \\
 &= \text{Tr} \exp \left[\frac{1}{2T} \sum_{\mathbf{k}} \begin{pmatrix} \gamma_{\mathbf{k}}^\dagger & \beta_{\mathbf{k}}^\dagger \end{pmatrix} \begin{pmatrix} E_{\mathbf{k}}^+ & 0 \\ 0 & E_{\mathbf{k}}^- \end{pmatrix} \begin{pmatrix} \gamma_{\mathbf{k}} \\ \beta_{\mathbf{k}} \end{pmatrix} + \frac{N\tilde{\Delta}_{\text{i.a.}}^2}{TV_0} \right], \tag{2.20}
 \end{aligned}$$

where $\Delta_{\text{eff}} = \Delta_{\text{ext}} + \Sigma_{\text{i}} - \Delta_{\text{c}} - 2\tilde{\Delta}_{\text{i.a.}}$ is used in the first line and composite ladder operators

$$\begin{aligned}
 \gamma_{\mathbf{k}}^\dagger &= \frac{1}{\sqrt{2E(\varepsilon_{\mathbf{k}} - E_{\mathbf{k}})}} \left(-\Delta_{\text{eff}} c_{\mathbf{k}}^\dagger - (E_{\mathbf{k}} - \varepsilon_{\mathbf{k}}) c_{\mathbf{k}+\mathbf{Q}}^\dagger \right) \\
 \beta_{\mathbf{k}}^\dagger &= \frac{1}{\sqrt{2E(\varepsilon_{\mathbf{k}} - E_{\mathbf{k}})}} \left((-E_{\mathbf{k}} + \varepsilon_{\mathbf{k}}) c_{\mathbf{k}}^\dagger + \Delta_{\text{eff}} c_{\mathbf{k}+\mathbf{Q}}^\dagger \right)
 \end{aligned}$$

are introduced in the third line. γ , γ^\dagger and β , β^\dagger obey fermionic commutation relations while β , γ commute. The grand canonical potential is

$$\begin{aligned}
 \Omega^{\text{MF}} &= T \ln \mathcal{Z}^{\text{MF}} \\
 &= \frac{N\tilde{\Delta}_{\text{i.a.}}^2}{V_0} + T \ln \text{Tr} \exp \left[\frac{1}{T} \sum_{\mathbf{k}}' (E_{\mathbf{k}}^+ \gamma_{\mathbf{k}}^\dagger \gamma_{\mathbf{k}} + E_{\mathbf{k}}^- \beta_{\mathbf{k}}^\dagger \beta_{\mathbf{k}}) \right] \\
 &= \frac{N\tilde{\Delta}_{\text{i.a.}}^2}{V_0} + T \ln \prod_{\mathbf{k}}' \left(1 + e^{E_{\mathbf{k}}^+/T} \right) \left(1 + e^{E_{\mathbf{k}}^-/T} \right) \\
 &= \frac{N\tilde{\Delta}_{\text{i.a.}}^2}{V_0} + T \sum_{\mathbf{k}}' \ln \left(1 + e^{E_{\mathbf{k}}^+/T} \right) \left(1 + e^{E_{\mathbf{k}}^-/T} \right), \tag{2.21}
 \end{aligned}$$

where we have restricted the summation in the second line to only one half of the Brillouin zone and removed a factor $1/2$ in comparison to (2.20). These measures balance each other out. Differentiating the grand canonical potential $\Omega^{\text{MF}} = T \ln \mathcal{Z}^{\text{MF}}$ with respect to $\tilde{\Delta}_{i.a.}$ and setting this derivative to zero yields

$$\frac{2N\tilde{\Delta}_{i.a.}}{V_0} + \sum_{\mathbf{k}} \frac{\Delta_{\text{eff}}}{E_{\mathbf{k}}^+ - E_{\mathbf{k}}^-} (f(E_{\mathbf{k}}^-) - f(E_{\mathbf{k}}^+)) = 0. \quad (2.22)$$

By $2\tilde{\Delta}_{i.a.} = -\Delta_{i.a.}$, (2.22) is equivalent to (2.17).

The derivation of (2.22) merits discussion. (2.22) is derived from the form (2.21) of the grand canonical potential Ω_{MF} by differentiating with respect to the order parameter $\Delta_{i.a.}$. This implies that by integrating the left-hand side of the gap equation (2.22) from zero order parameter to a finite value Δ , we obtain the grand canonical potential for Δ . This means that if at a given $\Delta_{i.a.}^0$ the right-hand side of (2.17) is larger (smaller) than the left-hand side, $\Omega_{\text{MF}}(\Delta_{i.a.}^0)$ is decreasing (increasing) in $\Delta_{i.a.}$. Therefore, we can distinguish stable, metastable, and unstable configurations by studying the gap equation.

2.2.3 Example: two dimensions

As an example, we discuss the zero-temperature case in two spatial dimensions without external field and $\Delta_c = \Sigma_i = 0$. Considering the two sides of (2.17) as functions of $\Delta_{i.a.}$, we plot their graphs in Fig. 2.4. The right-hand side exhibits a

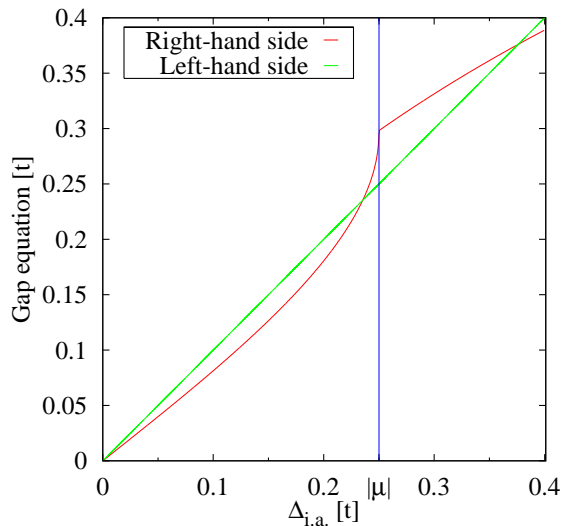


Figure 2.4: The right-hand side of the gap equation (2.17) has a kink at $\Delta_{i.a.} = |\mu|$ leading to further solutions. The solutions at $\Delta_{i.a.} = 0, 0.39t$ are minima while the solution at $\Delta_{i.a.} = 0.24t$ is a maximum of the grand canonical potential Ω . All data obtained for $V_0 = 2t$.

kink at $\Delta_{i.a.} = |\mu|$ because the sign of one of the dispersion branches E^\pm changes on the whole $\varepsilon_{\mathbf{k}} = 0$ line. Subsequently, the Fermi function cuts this line from the

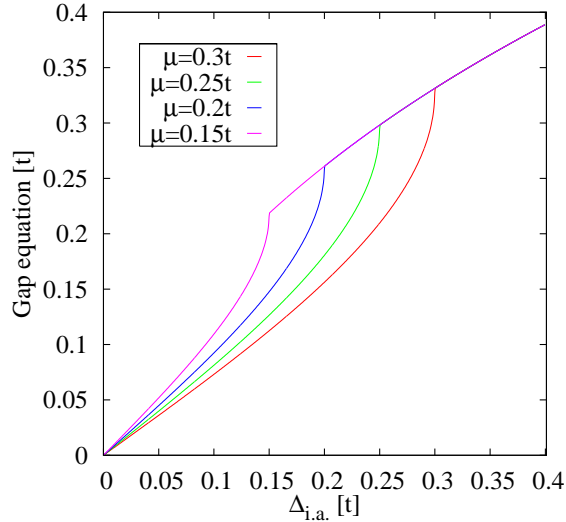


Figure 2.5: Right-hand side of the gap equation (2.17) for $V_0 = 2t$, $T = 0$, and varying chemical potential μ . Note that there is no dependence on μ for $\Delta_{i.a.} > \mu$.

integration domain on the right-hand side of (2.17). At the kink, the slope of the right-hand side of (2.17) as a function of $\Delta_{i.a.}$ diverges as $(1/\sqrt{|\mu| - \Delta_{i.a.}}) \log(|\mu| - \Delta_{i.a.})$ for $\Delta_{i.a.} \nearrow |\mu|$, as is shown by Reiss (2006). The right-hand side does not depend on μ if $\Delta_{i.a.} > |\mu|$, i.e. to the right of the kink in the figures, since μ enters the gap equation only via the Fermi distributions, see Fig. 2.5.

Since E_k^+ (E_k^-) is always positive (negative) for $\Delta_{i.a.} > |\mu|$, the thermodynamically stable solution is always half filled if the thermodynamically stable value of $\Delta_{i.a.}$ is larger than the modulus of the chemical potential. In this case, the system exhibits vanishing compressibility. This effect is neglected if the dependence of the filling on $\Delta_{i.a.}$ is not taken into account, as by Hirsch (1985). For a detailed discussion, see Reiss (2006).

Since (2.22) is obtained from $\partial_{\Delta_{i.a.}} \Omega^{\text{MF}} = 0$, all intersection points are extrema or saddle-points of Ω . If all intersection points are extrema of $\Omega(\Delta_{i.a.})$, the outermost one must correspond to a minimum of $\Omega(\Delta_{i.a.})$ for a thermodynamically stable configuration of the system to exist. Furthermore, by the construction of (2.22) and the discussion in the last paragraph of section 2.2.2, the integral of the bisector minus the right-hand side of (2.17) is equal to the energy gained through the opening of a finite gap. Thus, comparing the areas enclosed by the two graphs of Fig. 2.4 determines which of the two minima given by the intersections has lower energy.

Plots of the thermodynamic potential are shown in Fig. 2.6. For small $|\mu| > 0$, a local minimum develops at $\Delta_{i.a.} = 0$, which becomes the global and finally the only minimum if μ is increased further. Numerical study of (2.17) and Ω for various T and μ leads to the phase diagram of Fig. 2.3.

This concludes our mean-field investigation of the CDW mean-field model for general filling. We have derived the gap equation (2.17) without resorting to any approximation. In the derivation of (2.22), we have shown that mean-field

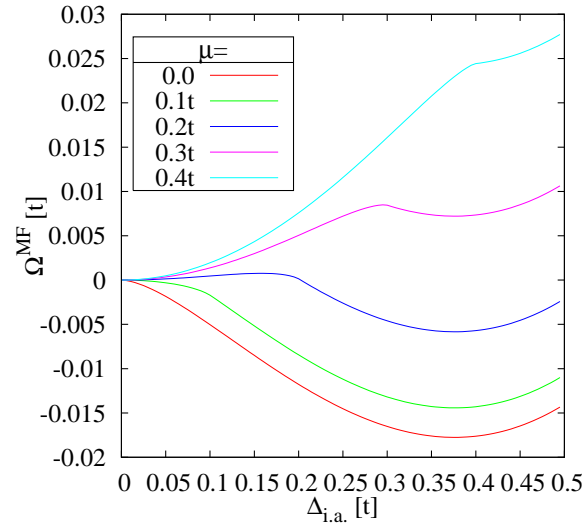


Figure 2.6: The grand canonical potential for $t' = 0$, $V_0 = 2t$. The position of the minimum at non-zero gap values does not change appreciably with μ , while the energy gain strongly depends on μ . $\Omega(\Delta_{i.a.} = 0)$ is subtracted from all curves.

theory yields the same result. From the quasiparticle energies E^\pm appearing in the diagonalization in (2.20) and the way they enter (2.17), we have seen how first-order phase transitions arise. Our understanding of the model (2.14) thus suffices to employ it as a testing ground for the functional renormalization-group method developed in 3.

Chapter 3

Deriving the renormalization group scheme

The term functional renormalization group (fRG) refers to any method which derives a set of properties of a physical system from an exact infinite hierarchy of ordinary differential equations. The differential equations which we derive here can be expressed as one-particle irreducible (1PI) Feynman diagrams, and the physical properties calculated are the so-called 1PI vertices. Hence, this particular incarnation of the fRG is called the 1PI scheme. Other frequently-encountered implementations are the Wick-ordered (Wieczerkowski (1988)) and Polchinski (Polchinski (1984)) schemes. A comparative derivation of the flow equations for each of these three schemes can be found in Enss (2005), and Rohe (2005) compares the results for certain approximate solutions in the context of the two-dimensional repulsive Hubbard model.

3.1 General formalism for symmetry breaking

Our goal in this chapter is to generalize the formal treatment of specific broken symmetries such as the translation-invariance breaking introduced in section 2.1.2. We start from the fermionic action S typically found in the exponent of the functional integral representation of a partition function

$$\mathcal{Z} = \int \mathcal{D}(\bar{\psi}, \psi) e^{-S(\bar{\psi}, \psi)}, \quad (3.1)$$

see e.g. chapter 2 of Negele and Orland (1998). Separating the quadratic part, we write

$$S(\bar{\psi}, \psi) \stackrel{\text{def}}{=} (\bar{\psi}, Q\psi) - \tilde{V}(\bar{\psi}, \psi), \quad (3.2)$$

where $\bar{\psi}, \psi$ are Grassmannian fields and we have introduced the notation

$$(\bar{\psi}, Q\psi) = \sum_j \bar{\psi}_j Q_j \psi_j.$$

\tilde{V} is assumed to be a polynomial where each monomial has an equal number of ψ and $\bar{\psi}$ factors. j is the collection of indices in which Q is diagonal. For free particles, j is the triple $(i\omega_n, \mathbf{k}, s)$ of Matsubara frequency (again, see Negele and Orland (1998)), particle momentum, and spin while $Q_j = i\omega_n - \xi_{\mathbf{k}}$, where ξ is the difference between the dispersion relation ε and the chemical potential μ .

For Bardeen-Cooper-Schrieffer (BCS) superconductivity (Bardeen et al. (1957)), symmetry breaking is taken into account by expanding Q into a matrix \mathbb{Q} so that the quadratic part of the action reads

$$(\bar{\phi}, \mathbb{Q}\phi) = \frac{1}{2} \sum_{s,k} (\bar{\psi}_{s,k} \quad \psi_{-s,-k}) \begin{pmatrix} i\omega_n - \xi_{\mathbf{k}} & \Delta_k \\ \Delta_k^* & i\omega_n + \xi_{-\mathbf{k}} \end{pmatrix} \begin{pmatrix} \psi_{s,k} \\ \bar{\psi}_{-s,-k} \end{pmatrix}.$$

This is equal to $(\bar{\psi}, Q\psi)$ if $\Delta = 0$. In comparison with ψ , the field operator ϕ has an additional index which can assume two different values. Flipping this index reverses the spin s , the four-momentum k , and switches the bar of the associated ψ or $\bar{\psi}$ to form singlet pairs of particles or holes, $\bar{\psi}_{s,k}\bar{\psi}_{-s,-k}$ and $\psi_{-s,-k}\psi_{s,k}$, through the off-diagonal elements of \mathbb{Q} . The strength of this pairing is given by Δ_k . It violates the particle-number conservation of the quadratic part of the action and breaks its invariance under phase shifts of the field operators.

To generalize this formulation, we introduce a generalized Nambu index l which can assume ν different values:

$$S = \nu^{-1} \sum_{j;l_1 l_2} \bar{\phi}_{j;l_1} \mathbb{Q}_{j;l_1 l_2} \phi_{j;l_2} - V(\bar{\phi}, \phi). \quad (3.3)$$

For each ψ_j , there must be ν pairs (j_i, l_i) , $i = 1, \dots, \nu$, such that

$$\text{either 1. } \phi_{j_i l_i} = \psi_j \quad \text{or 2. } \bar{\phi}_{j_i l_i} = \psi_j, \quad (3.4)$$

and the equivalent mapping must hold for each $\bar{\psi}_j$. Then, if the action is to remain invariant under the transformation to the new fields,

$$\mathbb{Q}_{j_i; l_i l_i} = \begin{cases} Q_j & \text{for alternative 1 in (3.4)} \\ -Q_j & \text{for alternative 2 in (3.4)}, \end{cases}$$

the sign being due to the anticommutative property of the Grassmannian fields. All entries of \mathbb{Q} off-diagonal in the l -indices constitute external fields favoring one possible symmetry breaking. In the BCS example, this is the pairing field Δ_k . By Wick's theorem, the inverse of $\nu^{-1}\mathbb{Q}$ is the bare Green's function \mathbb{G}_0 of the physical system under consideration. Under this inversion, the off-diagonal external fields turn into anomalous bare propagators.

As another example of such a transformation and the introduction of an external field, in (2.7) the additional index is used to – depending on its value – add or not add a momentum $\mathbf{Q} = (\pi, \pi, \dots)$ to the momentum index of the original field. This introduces processes which do not conserve momentum into the action, breaking translational symmetry.

3.2 Introducing the cutoff

In the following derivation of the flow equations for the one-particle irreducible (1PI) vertices, we follow Salmhofer and Honerkamp (2001) and Meden (2005). We introduce a real parameter Λ into our action by substituting \mathbb{Q} with

$$\mathbb{Q}^\Lambda := \mathbb{Q}/\chi(\Lambda), \quad (3.5)$$

where $\chi(\Lambda)$ is a function of the indices j, l_1, l_2 of \mathbb{Q} and the division in (3.5) is component-wise. χ must be differentiable in the continuous parameters of \mathbb{Q} and in Λ . Furthermore, there must be a $\Lambda_i \in \mathbb{R}$ for which the physical system S^Λ is solvable, i.e. the vertex functions are known, and a Λ_f with $\chi(\Lambda_f) \equiv 1$, i.e. $S^\Lambda = S$. These conditions allow for numerous choices of χ with various physical interpretations (see, for example, Enss (2005), section 4.2). Some problems can be simplified significantly by choosing a suitable cutoff function, as we see in chapter 5.

3.3 Generating functionals

Our aim is to calculate the anomalous self-energy and the effective interaction. The generating functional for these functions is the effective action, for which we know no explicit form in terms of microscopic parameters but which is related to the generating functional \mathcal{W} for the (connected) Green's functions by a Legendre transformation. Therefore, we first pass from the cutoff-dependent partition function \mathcal{Z}^Λ to \mathcal{W}^Λ by introducing Grassmannian source fields $\eta, \bar{\eta}$:

$$\exp \mathcal{W}(\eta, \bar{\eta}) = \int \frac{\mathcal{D}(\bar{\phi}, \phi)}{\det \mathbb{Q}/\nu} \exp [-S(\bar{\phi}, \phi) + (\bar{\phi}, \eta) + (\bar{\eta}, \phi)]. \quad (3.6)$$

We no longer explicitly denote the cutoff dependence for readability. We introduce the field expectation values in the presence of the sources,

$$J := -\frac{\partial \mathcal{W}}{\partial \bar{\eta}}(\eta, \bar{\eta}), \quad \bar{J} := \frac{\partial \mathcal{W}}{\partial \eta}(\eta, \bar{\eta}) \quad (3.7)$$

as well as their inverses $\eta(J, \bar{J})$ and $\bar{\eta}(J, \bar{J})$. The effective action

$$\Gamma(J, \bar{J}) = -\mathcal{W}(\eta(J, \bar{J}), \bar{\eta}(J, \bar{J})) - (\bar{J}, \eta(J, \bar{J})) - (\bar{\eta}(J, \bar{J}), J) \quad (3.8)$$

is the generating functional of the one-particle irreducible vertex functions γ_m (see Negele and Orland (1998)).

3.4 The flow equation for the effective action

In this section, we derive a flow equation for the effective action Γ through a flow equation for the generating functional \mathcal{W} of the connected Green's functions. Γ

and \mathcal{W} are related through (3.8), which we differentiate with respect to Λ to obtain

$$\begin{aligned}\dot{\Gamma} &= -\partial_\Lambda \mathcal{W}(\eta, \bar{\eta}) - (\dot{\eta}, \partial_\eta \mathcal{W}(\eta, \bar{\eta})) - (\dot{\bar{\eta}}, \partial_{\bar{\eta}} \mathcal{W}(\eta, \bar{\eta})) \\ &\quad - (\bar{J}, \dot{\eta}) - (\dot{\eta}, J),\end{aligned}$$

where we have omitted (J, \bar{J}) for readability. Employing (3.7), we see that all terms but the first on the right-hand side cancel and find $\dot{\Gamma} = -\partial_\Lambda \mathcal{W}(\eta, \bar{\eta})$. Hence, we can obtain a flow equation for Γ from a flow equation for \mathcal{W} . We thus take the partial derivative of (3.6) with respect to Λ , obtaining

$$\partial_\Lambda \mathcal{W} \exp \mathcal{W} \tag{3.9}$$

from the left-hand side, again omitting parameters for brevity. Differentiating the normalization factor on the right-hand side yields

$$\begin{aligned}\partial_\Lambda \frac{1}{\det(\mathbb{Q}/\nu)} &= -\frac{1}{(\det(\mathbb{Q}/\nu))^2} \partial_\Lambda \exp \text{Tr} \ln(\mathbb{Q}/\nu) \\ &= -\frac{1}{\det(\mathbb{Q}/\nu)} \text{Tr}(\dot{\mathbb{Q}} \mathbb{Q}^{-1}).\end{aligned} \tag{3.10}$$

Finally, we differentiate the exponential:

$$\begin{aligned}& -\frac{1}{\nu} \int \frac{\mathcal{D}(\bar{\phi}, \phi)}{\det(\mathbb{Q}/\nu)} (\bar{\phi}, \dot{\mathbb{Q}} \phi) e^{-S(\bar{\phi}, \phi) + (\bar{\phi}, \eta) + (\bar{\eta}, \phi)} \\ &= -\frac{1}{\nu} \int \frac{\mathcal{D}(\bar{\phi}, \phi)}{\det(\mathbb{Q}/\nu)} (\partial_\eta, \dot{\mathbb{Q}} \partial_{\bar{\eta}}) e^{-S(\bar{\phi}, \phi) + (\bar{\phi}, \eta) + (\bar{\eta}, \phi)} \\ &= -\frac{1}{\nu} (\partial_\eta, \dot{\mathbb{Q}} \partial_{\bar{\eta}}) \exp(\mathcal{W}) \\ &= -\frac{1}{\nu} \left((\partial_\eta \mathcal{W}, \dot{\mathbb{Q}} \partial_{\bar{\eta}} \mathcal{W}) + \text{Tr}(\dot{\mathbb{Q}} \partial_\eta \partial_{\bar{\eta}} \mathcal{W}) \right) \exp(\mathcal{W}).\end{aligned} \tag{3.11}$$

Note that in (3.11), the product $\dot{\mathbb{Q}} \partial_\eta \partial_{\bar{\eta}} \mathcal{W}$ is a matrix product, where the indices of the second term are given by the parameters of the source fields in the partial derivatives. We combine (3.9), (3.10), and (3.11) into

$$\partial_\Lambda \mathcal{W} = -\frac{1}{\nu} \left(\nu \text{Tr}(\dot{\mathbb{Q}} \mathbb{Q}^{-1}) + (\partial_\eta \mathcal{W}, \dot{\mathbb{Q}} \partial_{\bar{\eta}} \mathcal{W}) + \text{Tr}(\dot{\mathbb{Q}} \partial_\eta \partial_{\bar{\eta}} \mathcal{W}) \right). \tag{3.12}$$

To eliminate \mathcal{W} in favor of Γ , we replace the second term with $-(\bar{J}, \dot{\mathbb{Q}} J)$ according to (3.7). For the third term, we need two additional relations, which we derive in the following. For the first relation, we differentiate (3.8) with respect to the field expectation values J, \bar{J} :

$$\begin{aligned}\partial_J \Gamma &= -(\partial_J \eta, \partial_\eta \mathcal{W}(\eta, \bar{\eta})) - (\partial_J \bar{\eta}, \partial_{\bar{\eta}} \mathcal{W}(\eta, \bar{\eta})) \\ &\quad + (\bar{J}, \partial_J \eta) - (\partial_J \bar{\eta}, J) + \bar{\eta} \\ &= \bar{\eta}, \\ \partial_{\bar{J}} \Gamma &= -\eta,\end{aligned} \tag{3.13}$$

The cancellations are due to (3.7). For the second relation, we differentiate (3.7) with respect to J and \bar{J} and obtain

$$\begin{aligned}
 \mathbf{I} &= -(\partial_J \eta \partial_\eta \partial_{\bar{\eta}} \mathcal{W} + \partial_J \bar{\eta} \partial_{\bar{\eta}} \partial_\eta \mathcal{W}) \\
 \mathbf{I} &= \partial_{\bar{J}} \eta \partial_\eta \partial_\eta \mathcal{W} + \partial_{\bar{J}} \bar{\eta} \partial_{\bar{\eta}} \partial_\eta \mathcal{W} \\
 0 &= -(\partial_{\bar{J}} \eta \partial_\eta \partial_{\bar{\eta}} \mathcal{W} + \partial_{\bar{J}} \bar{\eta} \partial_{\bar{\eta}} \partial_\eta \mathcal{W}) \\
 0 &= \partial_J \eta \partial_\eta \partial_\eta \mathcal{W} + \partial_J \bar{\eta} \partial_{\bar{\eta}} \partial_\eta \mathcal{W}.
 \end{aligned} \tag{3.14}$$

Using (3.13), we rewrite our second relation (3.14) as

$$\underbrace{\begin{pmatrix} \partial_J \partial_J & \partial_J \partial_{\bar{J}} \\ \partial_J \partial_J & \partial_J \partial_{\bar{J}} \end{pmatrix}}_{=: \mathcal{V}} \Gamma \begin{pmatrix} \partial_{\bar{\eta}} \partial_\eta & -\partial_{\bar{\eta}} \partial_{\bar{\eta}} \\ -\partial_\eta \partial_\eta & \partial_\eta \partial_{\bar{\eta}} \end{pmatrix} \mathcal{W} = \mathbf{I}. \tag{3.15}$$

This allows us to replace the second derivative of \mathcal{W} in (3.12) with the upper left (or – up to a sign – the lower right) entry of \mathcal{V}^{-1} to obtain the flow equation

$$\dot{\Gamma} = \frac{1}{\nu} \left(\nu \text{Tr} \left(\dot{\mathbb{Q}} \mathbb{Q}^{-1} \right) - (\bar{J}, \dot{\mathbb{Q}} J) - \text{Tr}(\dot{\mathbb{Q}} (\mathcal{V}^{-1})_{11}) \right). \tag{3.16}$$

3.5 The flow equations for the 1PI vertex functions

By expanding (3.16) in the field expectation values J, \bar{J} and comparing coefficients, we derive flow equations for the 1PI vertex functions γ_m . First, we expand the effective action in the field expectation values:

$$\Gamma(J, \bar{J}) = \sum_{m=0} \sum_{X_1 \dots X_{2m}} \frac{\gamma_m(X_1, \dots, X_{2m})}{(m!)^2} \bar{J}(X_1) \dots \bar{J}(X_m) J(X_{m+1}) \dots J(X_{2m}), \tag{3.17}$$

where the indices X_i comprise both index types known from (3.3). We choose γ_m antisymmetric under permutations of the first m arguments and of the second m arguments. This makes the expansion (3.17) unambiguous. Plugging (3.17) into (3.15) while setting $\eta = \bar{\eta} = 0$ and $J = \bar{J} = 0$ yields

$$\mathbb{G} = -\gamma_1^{-1}. \tag{3.18}$$

Our strategy is to plug (3.17) into (3.16) and compare the coefficients of monomials in J, \bar{J} on both sides of the equation, but this is non-trivial due to the matrix inversion in (3.16). To study this inversion, we first notice that an equal number of J and \bar{J} arise in each term of (3.17), since our action (3.2) contains only monomials with an equal number of ϕ and $\bar{\phi}$. This argument can be understood by picturing perturbation theory diagrams for the vertex functions: All bare vertex functions have an even number of external legs, and every connection between two vertex

functions makes two legs internal. (3.15) thus implies that terms constant in J, \bar{J} appear only on the diagonal of \mathcal{V} :

$$\mathcal{V} = \underbrace{\begin{pmatrix} -\gamma_1 & 0 \\ 0 & \gamma_1 \end{pmatrix}}_{=: \mathcal{V}_0} + \underbrace{\begin{pmatrix} \tilde{\Gamma} & \partial_{\bar{J}}^2 \Gamma \\ \partial_J^2 \Gamma & -\tilde{\Gamma}^T \end{pmatrix}}_{=: \tilde{\mathcal{V}}}. \quad (3.19)$$

Note that

$$\tilde{\Gamma}(Y_1, Y_2) = \sum_{m=1} \sum_{X_1, \dots, X_{2m}} \frac{\gamma_{m+1}(Y_1, X_1, \dots, X_m, Y_2, X_{m+1}, \dots, X_{2m})}{(m!)^2} \bar{J}(X_1) \dots \bar{J}(X_m) J(X_{m+1}) \dots J(X_{2m}) \quad (3.20)$$

by the product rule and the antisymmetry of the vertex functions γ_m . Likewise, we find

$$(\partial_J \partial_J \Gamma)(Y_1, Y_2) = \sum_{m=1} \sum_{X_1, \dots, X_{2m}} \frac{\gamma_{m+1}(X_1, \dots, X_{m+1}, Y_1, Y_2, X_{m+2}, \dots, X_{2m})}{(m-1)!(m+1)!} \bar{J}(X_1) \dots \bar{J}(X_{m+1}) J(X_{m+2}) \dots J(X_{2m}), \quad (3.21)$$

and a very similar formula for $\partial_{\bar{J}} \partial_{\bar{J}} \Gamma$. The second matrix $\tilde{\mathcal{V}}$ of (3.19) therefore only contains vertex functions with $m \geq 2$. We expand \mathcal{V}^{-1} into a geometric series:

$$\mathcal{V}^{-1} = \mathcal{V}_0^{-1} \left(\mathbf{I} + \tilde{\mathcal{V}} \mathcal{V}_0^{-1} + (\tilde{\mathcal{V}} \mathcal{V}_0^{-1})^2 + (\tilde{\mathcal{V}} \mathcal{V}_0^{-1})^3 + \dots \right), \quad (3.22)$$

with

$$\tilde{\mathcal{V}} \mathcal{V}_0^{-1} = \begin{pmatrix} \tilde{\Gamma} \mathbb{G} & -\partial_{\bar{J}} \partial_{\bar{J}} \Gamma \mathbb{G} \\ \partial_J \partial_J \Gamma \mathbb{G} & \tilde{\Gamma}^T \mathbb{G} \end{pmatrix}, \quad (3.23)$$

where we have used (3.18). By (3.12) and (3.15), we only need to consider the upper left entry of \mathcal{V}^{-1} .

As a concrete first example, we construct the contribution of order zero in J, \bar{J} . Since $\gamma_1^{-1} = -\mathbb{G}$ by (3.18), we obtain

$$\text{Tr} \left(\dot{\mathbb{Q}} \gamma_1^{-1} \right) = \text{Tr} \left(\dot{\mathbb{Q}} \mathbb{G} \gamma_1 \mathbb{G} \right) \stackrel{\text{def}}{=} -\text{Tr} \left(\mathbb{S} \gamma_1 \right), \quad (3.24)$$

where we have defined the *single-scale propagator* \mathbb{S} . The name is motivated by its living on only the cutoff energy scale Λ when the limit of a sharp momentum shell cutoff is considered. This can be seen by plugging $\chi(\Lambda) = \Theta(|\xi_{\mathbf{k}}| - \Lambda)$ into (3.5) and taking the scale derivative to obtain the δ -distribution. Considering (3.24), we observe that the last term is the simplest case of a linear tree of vertex functions γ connected by full propagators \mathbb{G} and closed by convolution with the single-scale

propagator \mathbb{S} . Combining (3.24) and (3.16), we find the full flow equation for γ_0 :

$$\begin{aligned}
 \dot{\gamma}_0 &= \frac{1}{\nu} \text{Tr} \left(\dot{\mathbb{Q}} (\mathbb{Q}^{-1} \nu - \mathbb{G}) \right) \\
 &= -\frac{1}{\nu} \text{Tr} \left(\frac{\dot{\chi}}{\chi} (\nu - \nu (\mathbf{I} - \Sigma \mathbb{Q}^{-1} \nu)^{-1}) \right) \\
 &= -\frac{1}{\nu} \text{Tr} \left(\frac{\dot{\chi} \nu}{\chi} (\Sigma \mathbb{Q}^{-1} \nu + (\Sigma \mathbb{Q}^{-1} \nu)^2 + \dots) \right) \\
 &= \text{Tr} \left(\frac{\dot{\chi}}{\chi} \Sigma \mathbb{G} \right)
 \end{aligned} \tag{3.25}$$

where we have used (3.5) and the Dyson equation

$$-\gamma_1 = \mathbb{G}^{-1} = \frac{1}{\nu} \mathbb{Q} - \Sigma \tag{3.26}$$

for the second equality, employed geometric series expansion for the third and geometric series contraction for the fourth equality.

The tree concept is illustrated further by considering as a second example terms of second order in J, \bar{J} arising from the second term $\mathcal{V}_0^{-1} \tilde{\mathcal{V}} \mathcal{V}_0^{-1}$ in (3.22). The upper left component of this term is $-\gamma_1^{-1} \tilde{\Gamma} \gamma_1^{-1} = -\mathbb{G} \tilde{\Gamma} \mathbb{G}$. Keeping only the coefficient of the second-order monomial in J, \bar{J} leaves

$$- \sum_{X_1, X_2, Y_1, Y_2} \mathbb{G}(\bullet, Y_1) \gamma_2(Y_1, X_1, Y_2, X_2) \bar{J}(X_1) J(X_2) \mathbb{G}(Y_2, \bullet), \tag{3.27}$$

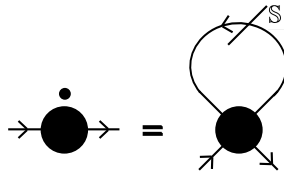
where the bullets are placeholders for the indices of $\mathbb{G} \tilde{\Gamma} \mathbb{G}$. We plug this into (3.16) to obtain

$$\dot{\gamma}_1 = \frac{1}{\nu} \left(-\dot{\mathbb{Q}} + \text{Tr}(\mathbb{S} \gamma_2) \right). \tag{3.28}$$

Employing the Dyson equation (3.26), we attain the flow equation

$$\dot{\Sigma} = \frac{1}{\nu} \text{Tr}(\mathbb{S} \gamma_2) \tag{3.29}$$

for the self-energy Σ . Diagrammatically, this can be expressed as



where the placement of the arrows is given by the structure of (3.27). We see that $\tilde{\mathcal{V}} \mathcal{V}_0^{-1}$ contributes to the flow equation of γ_m a tadpole diagram in which γ_{m+1} is closed by a single-scale propagator \mathbb{S} .

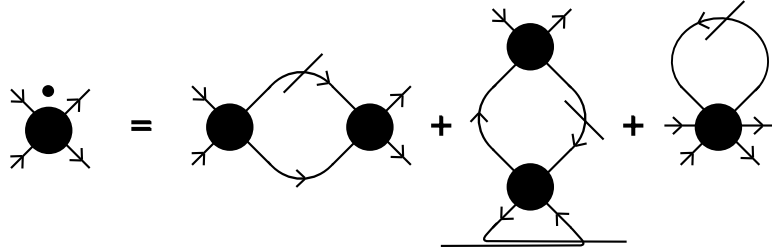
The flow equation for γ_2 is thus given by a tadpole diagram closing γ_3 and the diagrams arising from inserting the third term of (3.22) into (3.16). The upper left component of this third term reads

$$\mathbb{G}\tilde{\Gamma}\tilde{\Gamma}\mathbb{G} - \mathbb{G}\partial_J^2\Gamma\mathbb{G}\partial_J^2\Gamma\mathbb{G}. \quad (3.30)$$

Keeping only the terms of fourth order in \bar{J}, J , we obtain

$$\begin{aligned} \dot{\gamma}_2(\alpha_1, \alpha_2, \alpha_3, \alpha_4) &= \frac{4}{\nu} \sum_{X_i} \left[\gamma_2(X_1, \alpha_1, X_2, \alpha_3)\mathbb{G}(X_2, X_3)\gamma_2(X_3, \alpha_2, X_4, \alpha_4) \right. \\ &\quad \left. - \frac{1}{4}\gamma_2(X_1, X_2, \alpha_3, \alpha_4)\mathbb{G}(X_2, X_3)\gamma_2(\alpha_1, \alpha_2, X_3, X_4) \right] \mathbb{S}(X_4, X_1) \\ &\quad + O(\gamma_3). \end{aligned} \quad (3.31)$$

The discrepancy in the combinatorial prefactors of the two terms arises from the combinatorial discrepancy between (3.20) and (3.21). The antisymmetry of γ_2 is preserved in the second term of (3.31), but the first one needs to be antisymmetrized before or during the integration of the flow equation. The diagrammatic form of (3.31) is



In each second-order diagram, the single-scale propagator \mathbb{S} can be put on any internal line due to the cyclic property of the trace. We see that (3.30) contributes bubble diagrams to the flow of γ_m .

We present construction rules for the right-hand side of the flow equation for γ_m . These are derived from the structure of (3.23) and (3.22) as well as from the combinatorial factors in (3.20) and (3.21), as can be seen from the examples above. The diagrams on the right-hand side of the flow equation for γ_m are constructed in the following way.

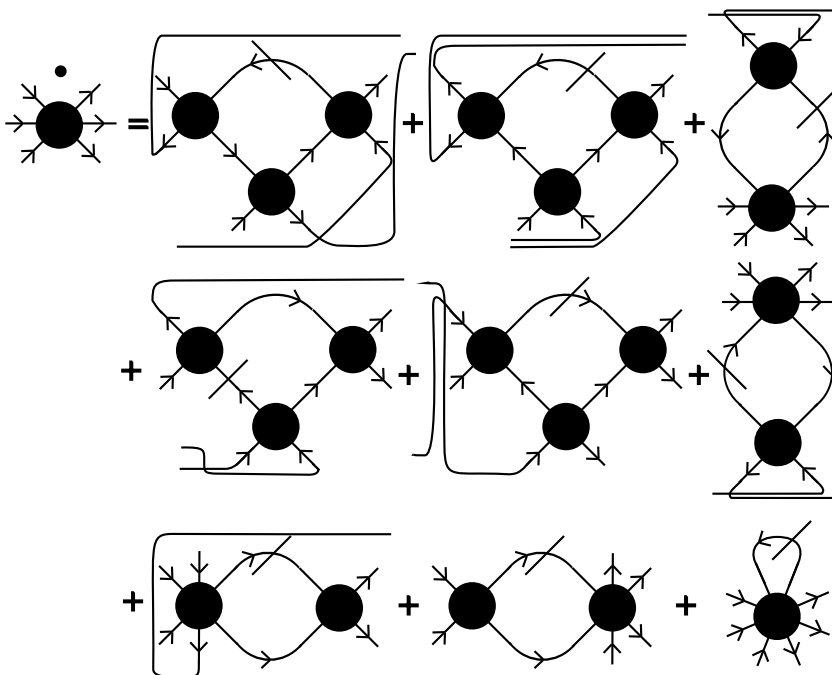
1. Form all linear trees with $2m+2$ external legs by connecting vertex functions γ_m with full Green's functions \mathbb{G} .
2. Close these trees with a single-scale propagator \mathbb{S} so that a one-particle irreducible diagram is formed.

The diagrams are evaluated by forming matrix products of γ_m for the vertices and \mathbb{G} for the lines and tracing over the external indices of the resulting convolution. For the combinatorial factors,

- a $2m$ -vertex by itself incurs a factor $(m!)^{-2}$.
- a $2m$ -vertex within a linear tree incurs
 - a factor $((m-1)!)^{-2}$ if its internal legs are antiparallel.
 - a factor $((m-2)!m!)^{-1}$ if its external legs are pointing out of the diagram.
 - a factor $-((m-2)!m!)^{-1}$ if its external legs are pointing into itself.

As the last step, the right-hand side must be antisymmetrized.

As an example, we draw the flow equation for γ_3 :



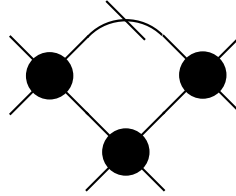
The last term constitutes a feed-back of γ_4 on the flow of γ_3 . The flow equations for all γ_m form a hierarchy in which a given level feeds back on the level above through a tadpole diagram arising from the second term in (3.22). While the author knows no method which extracts physical information from the whole hierarchy, truncations yield approximations for which rigorous error estimates can be obtained (Salmhofer and Honerkamp (2001)). We present the truncation which we employ in the remainder of this work in the next section.

3.6 The Katanin truncation

In this section, following Katanin (2004), we truncate the infinite hierarchy of flow equations derived in 3.5. There are two key advantages to Katanin's approach in comparison to the usual zeroing of γ_6 (see Zanchi and Schulz (1998); Halboth (1999); Halboth and Metzner (2000); Halboth and Metzner (2000); Zanchi and

Schulz (2000); Salmhofer and Honerkamp (2001); Rohe (2005); Enss (2005); Fu et al. (2006)). First, the approximate flow equations it delivers are exact up to third order in the quartic part of the action (3.2), and thus ideally suited for the treatment of physical problems with two-particle interactions. Second, a further approximation brings the approximate flow equations into a form that is treatable and still reproduces the exact solutions of the mean-field models introduced in chapter 2 and section 5.1. Treatable here means that the usual divergence of the flow of γ_2 , which has previously been used as a signpost for symmetry breaking, can be circumvented. The fRG for the two-particle irreducible vertex functions has similar advantages for mean-field models (Dupuis (2005)).

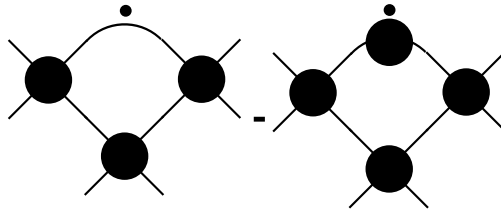
We study the flow equation for γ_3 up to third order in γ_2 . The only diagram we have to treat is



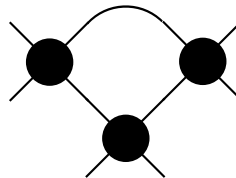
where we have omitted the arrows for brevity. We rewrite the single-scale propagator

$$\mathbb{S} = -\mathbb{G}\dot{\mathbb{Q}}\mathbb{G} = -\mathbb{G}(\mathbb{G}^{-1} + \dot{\Sigma})\mathbb{G} = \dot{\mathbb{G}} - \mathbb{G}\dot{\Sigma}\mathbb{G} \quad (3.32)$$

to isolate the dependence on $\dot{\mathbb{G}}$. Plugging (3.32) into the above diagram yields

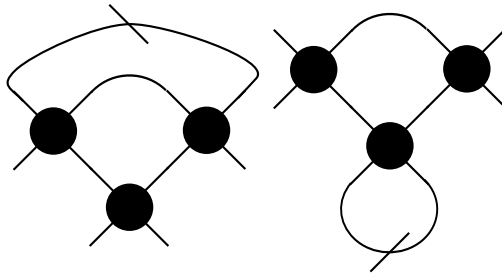


where the second diagram is of fourth order in γ_2 as can be seen by plugging in the flow equation for Σ , (3.29). The second diagram is therefore subsequently ignored. Up to order three in γ_2 , the first diagram is the scale derivative of

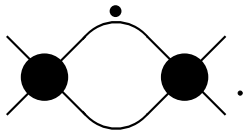


as can be seen diagrammatically by taking into account that γ_2 is of order two in γ_2 according to (3.31). This implies that in our approximation γ_3 is given by the above triangle diagram.

We diagrammatically plug our result for γ_3 into the flow equation (3.31) for γ_2 . We observe that in the absence of arrows, there are two topologically distinct ways to close the diagram with a single-scale propagator \mathbb{S} :



We first consider the second “panting-dog” diagram, where we discern the tadpole diagram from (3.29) in the dog’s tongue. Substituting $\dot{\Sigma}$, we exploit (3.32) to combine the resulting diagram with the loop diagrams from the flow equation for γ_2 , (3.31), to obtain



Secondly, we study the first “dog-snout” diagram, which consists of two loops overlapping in the dog’s brow. In chapter 2 and section 5.1, we see that diagrams with overlapping loops vanish in the thermodynamic limit for mean-field models. Furthermore, the dog-snout diagram is of third order in γ_2 , and therefore less important in a weak-coupling context than the panting-dog diagram, which turned out to contribute on the second order of γ_2 . We ignore the dog snout’s contribution in the remainder of this work. The flow equations which we employ are

Solving these flow equations yields the exact self-energy and effective interaction in the thermodynamic limit for any model with only two-particle interactions for which the dog-snout diagram vanishes. We study an example both analytically and numerically in chapter 4. In addition, in the presence of only two-particle interactions, the corrections to the right-hand side of these flow equations are of third order in the interaction strength (Salmhofer et al. (2004)). Furthermore, the fulfillment of Ward identities in the flow is systematically improved by this modification (Katanin (2004)).

Chapter 4

Charge-density wave: renormalization-group approach

4.1 Second-order phase transitions

4.1.1 Renormalization group setup

We apply the one-particle irreducible (1PI) functional renormalization group (fRG) scheme introduced in chapter 3 to the reduced charge-density-wave model (2.4) at half filling of section 2.1.1. The 1PI scheme is described by Salmhofer and Honerkamp (2001); Wetterich (1993) and is here employed in the version suggested by Katanin (2004), as derived in section 3.6. In this version, the differential equations for the self-energy and effective interaction constitute a closed system. The special structure of the interaction in (2.4) allows us to further simplify the equations. In contrast to the Bardeen-Cooper-Schrieffer (BCS) flow studied by Salmhofer et al. (2004), no anomalous effective interactions are generated in our case. We verify analytically and numerically that the fRG reproduces the resummation results from sections 2.1.2 and 2.1.3.

Following section 3.2, we introduce a cutoff function

$$\chi(\Lambda) = \Theta(|\xi| - \Lambda). \quad (4.1)$$

In our calculations, all modes satisfying $|\xi| > \Lambda$ have been integrated out. The effective interaction and self-energy at this scale can thus be interpreted as parameters of an effective theory for a reduced system with smaller bandwidth. We start the flow at $\Lambda_i = W$, where $2W$ is our system's bandwidth and all modes have yet to be integrated out. We integrate the flow down to $\Lambda_f = 0$, as we see from (4.1) that $\chi(\Lambda_f) \equiv 1$. To analytically implement this procedure, we introduce $\chi(\xi, \Lambda)$ as a placeholder for any cutoff function, which shall have range $[0, 1]$, assume the value $1/2$ when $\Lambda = \xi$, approach 0 when reducing ξ below Λ and 1 when increasing ξ above Λ . We replace $\mathbb{Q}(\xi)$ by $\mathbb{Q}(\xi)/\chi(\xi, \Lambda)$ as in (3.5), suppressing low-energy modes in the field integral and rendering the self-energy and effective interaction scale-dependent.

The replacement of $\mathbb{G}\mathbb{S}$ in the flow (3.31) of the effective interaction by $\dot{\mathbb{G}}\mathbb{G}$ (see section 3.6) is crucial for our ability to follow the flow down to $\Lambda = 0$. This is because in the original version of the fRG, the flow of the effective interaction diverges before all modes are integrated out. In the Katanin version of the 1PI scheme, the exact hierarchy of RG differential equations with the exception of the first equation is written using only full four-point functions, full propagators and scale-differentiated full propagators on the right-hand sides. The differential equations for the self-energy and the four-point function thus constitute a closed system. In particular, the contribution to the flow of the four-point function which involves the six-point function (see the diagrammatic equation on page 41) is partially taken into account in the Katanin scheme by diagrams involving only four-point functions and full or scale-differentiated full propagators, respectively. The part with overlapping loops – the dog-snout diagram of section 3.6 – of this contribution vanishes for the special structure of the interaction and the thermodynamic limit considered here. The remaining part of this contribution is taken into account by the replacement of the single-scale propagator by the scale-differentiated full propagator. We use the diagrammatic conventions from section 2.1.2, where a hatched rectangle denotes the effective interaction V , a hatched circle denotes the anomalous self-energy $\Delta_{\text{i.a.}}$, and bold lines denote full propagators. We introduce the additional convention that straight lines denote Λ -differentiation of all entities crossed by the line. The graphical form of the fRG differential equations according to these conventions is as shown in Fig. 4.1. The right-hand side of the

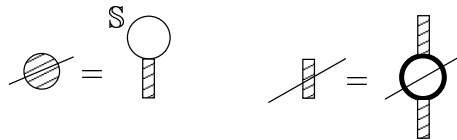


Figure 4.1: The hierarchy of flow equations for the self-energy and the effective interaction

flow equation for the self-energy only contains the off-diagonal (anomalous) part of the single-scale propagator \mathbb{S} due to the restricted form of the interaction. This is discussed in the context of the derivation of the gap equation (2.9) in 2.1.2.

In the flow of the effective interaction (right part of Fig. 4.1), the summation over the Nambu indices of the internal lines includes normal and anomalous propagators. Analogously to the perturbation expansion in section 2.1.2, in the thermodynamic limit $N \rightarrow \infty$ the special momentum structure of the initial interaction is conserved by the RG flow of the effective interaction. At half filling, no new effective interactions with different external legs are generated. This is in contrast to the BCS pairing model (Bardeen et al. (1957)), where $U(1)$ -symmetry-breaking effective interactions with four incoming or four outgoing legs are generated (Salmhofer et al. (2004)). For the BCS case, linear combinations of normal and anomalous effective interactions are identified with amplitude and phase modes. These names stem from the thermodynamic potential as a function of the order parameter. Rotating the $\mu = 0$ graph of Fig. 2.6 around the

Ω^{MF} -axis, we obtain a shape that has been described as a Mexican hat but also as a Bordeaux bottle bottom, see Fig. 4.2. This is a thermodynamic potential

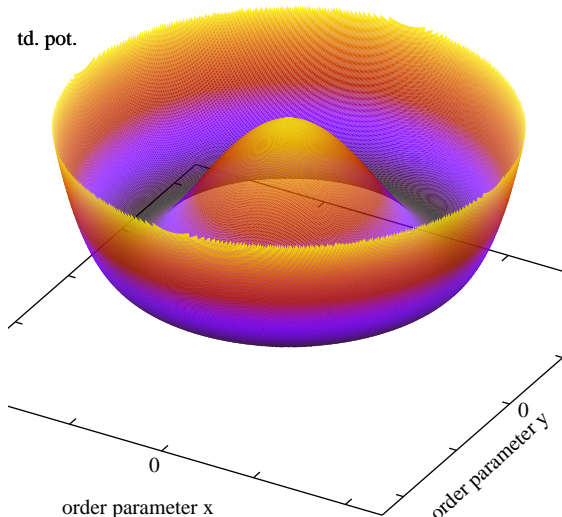
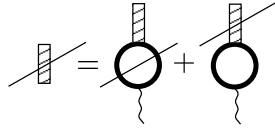


Figure 4.2: The Bordeaux-bottle bottom or Mexican hat thermodynamic potential

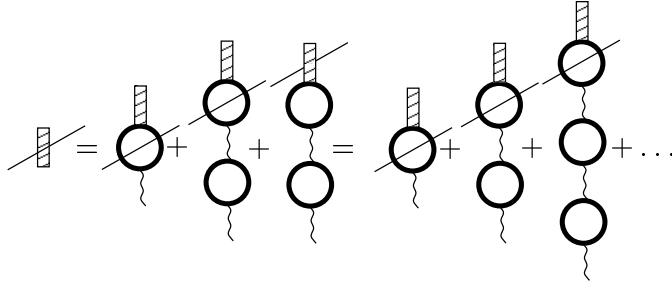
shape typical for the breaking of a continuous symmetry. It sports a continuum of energetically degenerate minima of the thermodynamic potential. Selecting one of these minima breaks the symmetry. The shape implies the existence of two distinct types of excitations, one radial and one angular in the order parameter plane. They are called amplitude and phase mode, respectively. Phase modes can be excited with arbitrarily small energy since there is no energy slope to overcome as for the amplitude mode. Thus, the phase mode is massless while the amplitude mode is massive away from criticality (Salmhofer et al. (2004)), a fact that is also observed when studying bosonic theories (Strack et al. (2007)). In the half-filled CDW model, there is no phase mode, as the order parameter has no phase. In this case, the effective interaction behaves like the amplitude mode of the BCS problem.

4.1.2 Renormalization group and resummation

We prove in the following that the equations in Fig. 2.1 are equivalent to the fRG equations in Fig. 4.1. We observe that the cutoff changes neither the structure of the bare interaction nor the conservation laws of the bare propagator. Therefore, the arguments of section 2.1.2 that lead to the resummations of the perturbation expansions for the self-energy and the effective interaction also hold for the cut-off system. We take the derivative with respect to Λ of the diagrammatic form of the Bethe-Salpeter equation for the cut-off system:

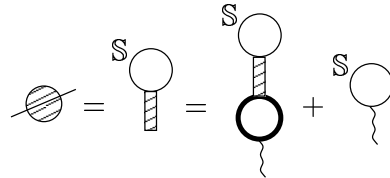


On the right-hand side, we have applied the product rule. We repeatedly replace the scale-differentiated effective interaction on the right-hand side with the full right-hand side to obtain:

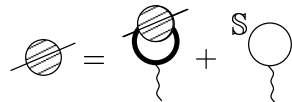


We identify the sum of loop chains that we resummed in the derivation of Fig. 4.1(b) and thus recover the right-hand side of the flow equation for the effective interaction. Since the solution of the corresponding initial-value problem is unique, the solution of the fRG flow equations satisfies the Bethe-Salpeter equation from which we started. This demonstrates the equivalence of the effective interaction flow equation and the Bethe-Salpeter equation.

We now study the flow equation for the self-energy. Replacing the effective interaction on the right-hand side with the right-hand side of the diagrammatic form of the Bethe-Salpeter equation yields:



The flow equation for the self-energy allows us to substitute the cutoff-differentiated self-energy for the tadpole part of the diagram including the effective interaction:



Symbolically, the loops of the two tadpole diagrams read:

$$\mathbb{G} \left(\frac{d}{d\Lambda} \Sigma \right) \mathbb{G} - \mathbb{G} \left(\frac{d}{d\Lambda} \mathbb{G}_0^{-1} \right) \mathbb{G} = -\mathbb{G} \left(\frac{d}{d\Lambda} \mathbb{G}^{-1} \right) \mathbb{G} = \frac{d}{d\Lambda} \mathbb{G}. \quad (4.2)$$

This shows that the fRG flow equation for the self-energy is the derivative of the gap equation for the system including the cutoff. Since the solution of the corresponding initial-value problem is unique, the solution of the fRG flow equations is also a solution of the gap equation. This concludes the proofs of the equivalence of the resummation and the fRG equations for the case of the Hamiltonian (2.5).

4.1.3 Flow equations at finite temperature

To evaluate the diagrams of Fig. 4.1, we derive the cutoff Green's function from (2.7) and (2.8):

$$\mathbb{G}^\Lambda = \frac{\chi(\Lambda)}{\omega_n^2 + \varepsilon^2 + (\chi(\Lambda)\Sigma^\Lambda)^2} \begin{pmatrix} -i\omega_n - \varepsilon & -\chi(\Lambda)\Sigma^\Lambda \\ -\chi(\Lambda)\Sigma^\Lambda & -i\omega_n + \varepsilon \end{pmatrix}. \quad (4.3)$$

In comparison with (2.8), the self-energy is replaced by its scale-dependent variant multiplied by χ , and the Green's function as a whole is multiplied by χ .

(4.3) enables us to write down the flow equation for the effective interaction V . To that end, we first note the complication that the momentum arguments of the propagators in the right loop of Fig. 4.1 differ by \mathbf{Q} , just as in the mean-field case 2.1. However, this only changes the sign of the bare energies ε written on the diagonal of (4.3), as Σ is constant in momentum and χ contains only the modulus of ε . This eases the evaluation of the diagram which proceeds mainly by multiplying $\mathbb{G}_{\mathbf{k}}$ and $\mathbb{G}_{\mathbf{k}+\mathbf{Q}}$ and tracing, which yields

$$\dot{V} = V^2 T \sum_{\mathbf{k}, \omega_n} \frac{\partial}{\partial \Lambda} \frac{2\chi^2}{(\omega_n^2 + \varepsilon^2 + \chi^2 \Sigma^2)^2} (-\omega_n^2 - \varepsilon^2 + \chi^2 \Sigma^2),$$

where we have suppressed the dependence on Λ in the notation. Second, we note that the Matsubara sum can be done analytically using (B.3) and (B.4) to obtain

$$\dot{V} = 2V^2 \frac{\partial}{\partial \Lambda} \sum_{\mathbf{k}} \chi^2 \left\{ (-\varepsilon^2 + \chi^2 \Sigma^2) \left[\frac{\tanh}{4E^3} - \frac{1}{8TE^2 \cosh^2} \right] - \frac{\tanh}{4E} - \frac{1}{8T \cosh^2} \right\}, \quad (4.4)$$

where we have suppressed the arguments of the hyperbolic functions, all of which are $E/2T$, as well as momentum arguments, all of which are \mathbf{k} , and recycled E to abbreviate $\sqrt{\varepsilon^2 + \chi^2 \Sigma^2}$. This form of the flow equation already suffices for numerical evaluation purposes, and we will exploit this in the context of the Hubbard model in section 5.3.

To further our analytical understanding of the flow equations, we evaluate the scale derivative of the integral in (4.4). To make optimal use of the sharp cutoff (4.1), we employ Morris' lemma (3.19) of Morris (1994) in the following way. We first rewrite the integration over momenta as an integration over energies

$$\sum_{\mathbf{k}} \rightarrow \int_{-W}^W d\varepsilon \rho(\varepsilon),$$

which is unproblematic as \mathbf{k} appears only as $\varepsilon_{\mathbf{k}}$ in (4.4). Second, we note that the Λ -dependence of the right-hand side of (4.4) stems from χ and Σ . This implies that the Λ -derivative of the integrand \mathcal{I} is split into two parts:

$$\int_{-W}^W d\varepsilon \rho(\varepsilon) \dot{\mathcal{I}} = \int_{-W}^W d\varepsilon \rho(\varepsilon) \left(\dot{\chi} \frac{\partial \mathcal{I}}{\partial \chi} + \dot{\Sigma} \frac{\partial \mathcal{I}}{\partial \Sigma} \right)$$

which can be rewritten as

$$\int_{-W}^W d\varepsilon \rho(\varepsilon) \dot{\mathcal{I}} = \int_{-W}^W d\varepsilon \rho(\varepsilon) \left(\mathcal{I}|_{\chi=1} \delta(|\varepsilon| - \Lambda) + \dot{\Sigma} \frac{\partial \mathcal{I}}{\partial \Sigma} \right)$$

according to Morris' lemma. Third, we plug in the expression for \mathcal{I} from (4.4) to obtain

$$\begin{aligned} \dot{V} = \rho_0 V^2 \left\{ -\frac{\Lambda^2}{E} \left(\frac{\Lambda^2}{E^2} \tanh + \frac{\Sigma^2 \beta}{2E} \cosh^{-2} \right) \right\} \Big|_{\varepsilon=\Lambda} \\ - \int_{\Lambda}^W \frac{d\varepsilon}{E} \frac{\Sigma \dot{\Sigma}}{E^2} \left[\frac{3\varepsilon^2}{E^2} \left(\tanh - \frac{\beta E}{2} \cosh^{-2} \right) + \beta^2 \Sigma^2 \frac{\tanh}{2 \cosh^2} \right] \Big|_{\chi=1}, \end{aligned} \quad (4.5)$$

where we have assumed a constant density of states to remove dimensionality effects. This is the flow equation we will use for our numerical and analytical analysis. Note that χ has been eliminated from the expression along with one integration in comparison to (4.4).

We turn to the flow equation for the order parameter and anomalous self-energy Σ . Its diagrammatic form is drawn in the left part of Fig. 4.1. The algebraic complexity of the equation can be significantly reduced by employing Morris' lemma (3.19) of Morris (1994). To this end, we study the single-scale propagator \mathbb{S} appearing in the diagram. We note that

$$\begin{aligned} \dot{\chi} \frac{\partial \mathbb{G}}{\partial \chi} &= \dot{\chi} \frac{\partial}{\partial \chi} (\mathbb{Q} - \Sigma \sigma_x)^{-1} \\ &= (\mathbb{Q} - \Sigma \sigma_x)^{-1} \dot{\chi} \frac{\partial \mathbb{Q}}{\partial \chi} (\mathbb{Q} - \Sigma \sigma_x)^{-1} \\ &= -\mathbb{G} \dot{\mathbb{Q}} \mathbb{G} \\ &= \mathbb{S}. \end{aligned} \quad (4.6)$$

(4.6) facilitates the use of Morris' lemma in the presence of single-scale propagators. We continue with our study of the self-energy flow by including the external field Δ_{ext} in Σ as its initial condition. Evaluating the diagrams of Fig. 4.1, we again suppress scale and frequency dependence in the notation and write $E := \sqrt{\varepsilon^2 + \chi^2 \Sigma^2}$, where Σ is the spectral gap caused by the symmetry breaking. The fRG differential equation reads

$$\dot{\Sigma} = V \frac{\Sigma \rho_0}{E} \tanh \Big|_{\substack{\varepsilon=\Lambda \\ \chi=1}}, \quad (4.7)$$

where we have switched from momentum integration to energy shell integration, used (4.6), and assumed a flat density of states ρ_0 in order to remove dimensionality effects. If we choose $\Delta_{\text{ext}} = 0$, Σ remains zero for all scales. Then only the first term in (4.5) remains, and the flow will diverge at a nonzero scale Λ_c . We would thus be neither able to integrate over all scales nor compare our results to

the resummation of section 2.1.2. We therefore always study the RG equations for a finite Δ_{ext} , usually $10^{-4}t$. We show in the following that this circumvents the divergence of the effective interaction while still enabling us to approximate arbitrarily well the exact mean-field results without explicit symmetry breaking in the temperature range determined in section 2.1.3.

4.1.4 Renormalization group at zero temperature

We first consider zero temperature, $T = 0$. In this case, it is easier to write down the analytical expressions, the roles of the different right-hand side terms are easily identifiable, and the value of the effective interaction at $\Lambda = 0$ is nearly independent of Δ_{ext} , as Λ_c is larger than the double width at half maximum of the effective interaction flow peak (see Fig. 4.3, lower part).

In the limit $T \rightarrow 0$, (4.5) and (4.7) become

$$-\frac{d}{d\Lambda}V = V^2 \frac{\Lambda^2 \rho_0}{\sqrt{\Lambda^2 + \Sigma^2}^3} - 3V^2 \Sigma \left(-\frac{d\Sigma}{d\Lambda} \right) \int_{\Lambda}^W d\xi \frac{\xi^2 \rho_0}{E^5}, \quad (4.8)$$

$$-\frac{d}{d\Lambda}\Sigma = V\Sigma\rho_0 \frac{1}{\sqrt{\Lambda^2 + \Sigma^2}}. \quad (4.9)$$

(4.8) and (4.9) can be integrated numerically. The typical shapes of these flows are exhibited in Fig. 4.3. We see that the divergence of the effective interaction is regularized by the external symmetry-breaking field, which is taken into account as the initial value of Σ . Hence, we can integrate out all modes of the fermionic spectrum. The effective interaction in the CDW problem behaves analogously to the linear combination of normal and anomalous effective interactions in the BCS problem (Salmhofer et al. (2004)) which drives the flow of the order parameter. This agrees with our interpretation of the effective interaction as an amplitude mode. The Λ -dependence of Σ around the scale where V peaks approaches a kink for $\Delta_{\text{ext}} \rightarrow 0$. The graph of $\Sigma(\Lambda)$ resembles the graph of $\Sigma(T)$ from Fig. 2.2, showing that temperature acts in a similar fashion as the cutoff in this system. The main difference between the graphs is that $\Sigma(T \rightarrow 0)$ approaches a constant function while $\Sigma(\Lambda \rightarrow 0)$ is linear.

The impact of the self-energy feedback on the RG flow can be thoroughly understood by analyzing the terms appearing in (4.8) and (4.9). Bear in mind that we think of the flow as progressing from larger to smaller values of Λ , i.e. from right to left in our plots. We first consider the limit $\Sigma = 0$. Now, the self-energy no longer flows while the effective interaction flows according to $-dV/d\Lambda \propto V^2/\Lambda$. For any positive V_0 , the solution of the corresponding initial value problem is singular, showing that at $T = 0$ symmetry is broken for all repulsive initial interactions.

An arbitrarily small initial symmetry-breaking field immediately has dramatic consequences: As soon as V begins to increase strongly, so does the self-energy due to the coupled effects of a large V and a back-feeding Σ on the RHS of (4.9). The second term on the RHS of (4.8) is negative. It corresponds to a correction of the flow by the modes which are integrated out at the current scale, which is necessary

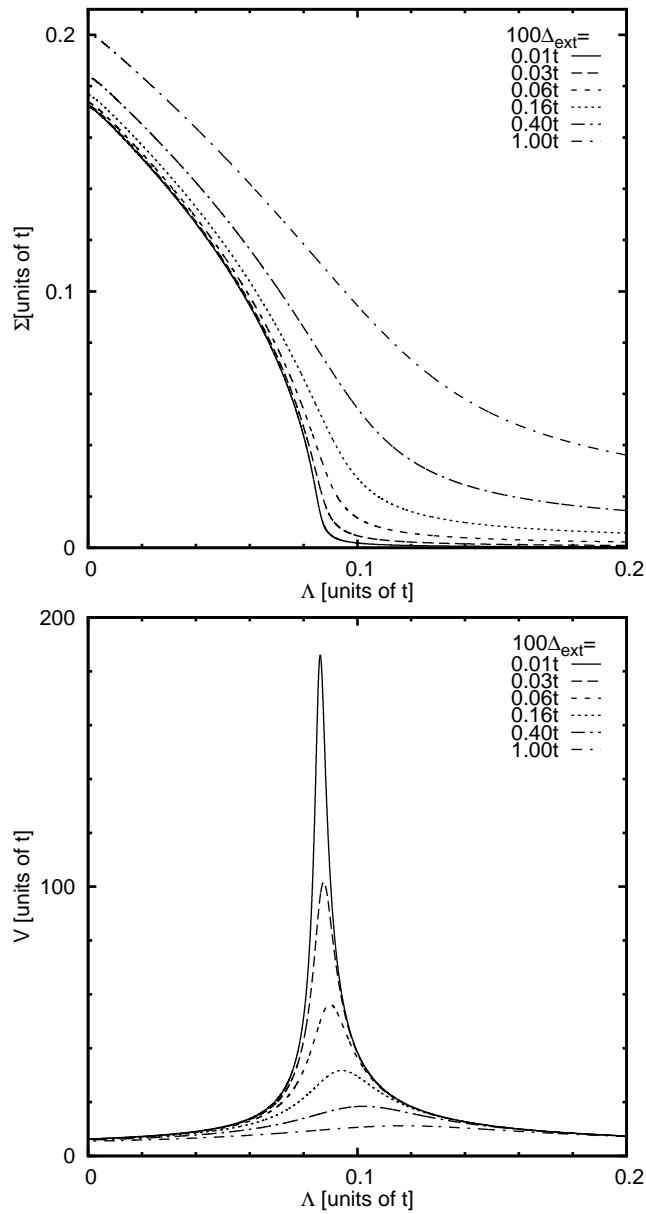


Figure 4.3: Low-energy portions of the $T = 0$ flows of the self-energy (top) and effective interaction (bottom) for $V_0 = 2t$ and various Δ_{ext} . $\rho_0 = 1/2\pi$ for all numerical calculations. Compare with Fig. 2.2.

because these modes' self-energy is changing in the flow even at scales where the modes themselves are integrated out. It becomes large as the slope of Σ exceeds Σ itself, while the positive first term is damped by an effective Λ^2/Σ^3 -dependence as soon as Σ becomes much larger than Λ . The effective interaction is hence pulled back down. It never reaches zero since the negative second term on the RHS of (4.8) becomes proportional to V^3 while the positive first term becomes proportional to V^2 ($d\Sigma/d\Lambda$ is $O(V)$). This implies that the self-energy never decreases. The two terms on the RHS of (4.8) thus approach mutual cancellation, causing V and in turn $-d\Sigma/d\Lambda$ to be almost constant in Λ (the contributions from Σ on the RHS of (4.9) cancel when $\Sigma \gg \Lambda$).

The behavior described above remains qualitatively the same at finite temperatures, as long as these are below the double width at half maximum of $V^{\Delta_{\text{ext}}}(T)$. This is illustrated by the lowest-temperature curve of the lower panel of Fig. 4.4. The shape of $V(\Lambda)$ is very similar to the shape of $V(T)$ in the lower part of Fig. 2.2, thus illustrating again that temperature has an effect comparable to that of an energy or momentum cutoff. The finite temperature case is discussed in detail in the next section.

4.1.5 Renormalization group flows at finite temperatures

We now turn to the analysis of the finite temperature fRG equations (4.5) and (4.7). Due to their more involved nature, the analysis is largely numeric. We find the same behavior as calculated using the conventional resummation methods applied in section 2.1.2. The initial symmetry-breaking field plays the same crucial role as in the zero-temperature case. We use a coupling of $V_0 = 2t$ in the following.

The upper plot of Fig. 4.4 shows how the flows of the self-energy flatten if the temperature increases beyond $T \approx 0.1t$. Above T_c , $\Sigma(\Lambda = 0)$ vanishes in the limit $\Delta_{\text{ext}} \rightarrow 0$. The flow of the effective interaction is shown in the lower panel of Fig. 4.4. The graph of the flow is pushed to the left with increasing temperature, its shape remaining largely unchanged. As the flow's maximum approaches zero, the final value of the effective interaction increases until the maximum has reached $\Lambda = 0$. This corresponds to the behavior of the effective interaction on the low-temperature side of Fig. 2.2 (lower part). For even higher temperatures, the final value of the effective interaction decreases, corresponding to the behavior on the high-temperature side of Fig. 2.2.

The lower part of Fig. 4.5 shows that $\Lambda_c(T)$ saturates quickly far below the critical temperature. It also illustrates the motion of the effective interaction flow maximum, which is pushed to lower scales by an increase in temperature as described above. It approaches zero in a linear fashion with increasing temperature, in contrast to $\Sigma(T \rightarrow T_c)$, which exhibits a square-root behavior.

We are furthermore interested in the dependence on Δ_{ext} of the flow of the self-energy at finite temperatures. As we see below, this raises the question of the method's extensibility to non-mean-field models, which is undertaken in section 5. This question arises due to the interplay of the correctness of the truncation and the necessary limit of vanishing external field, which is studied below. In contrast

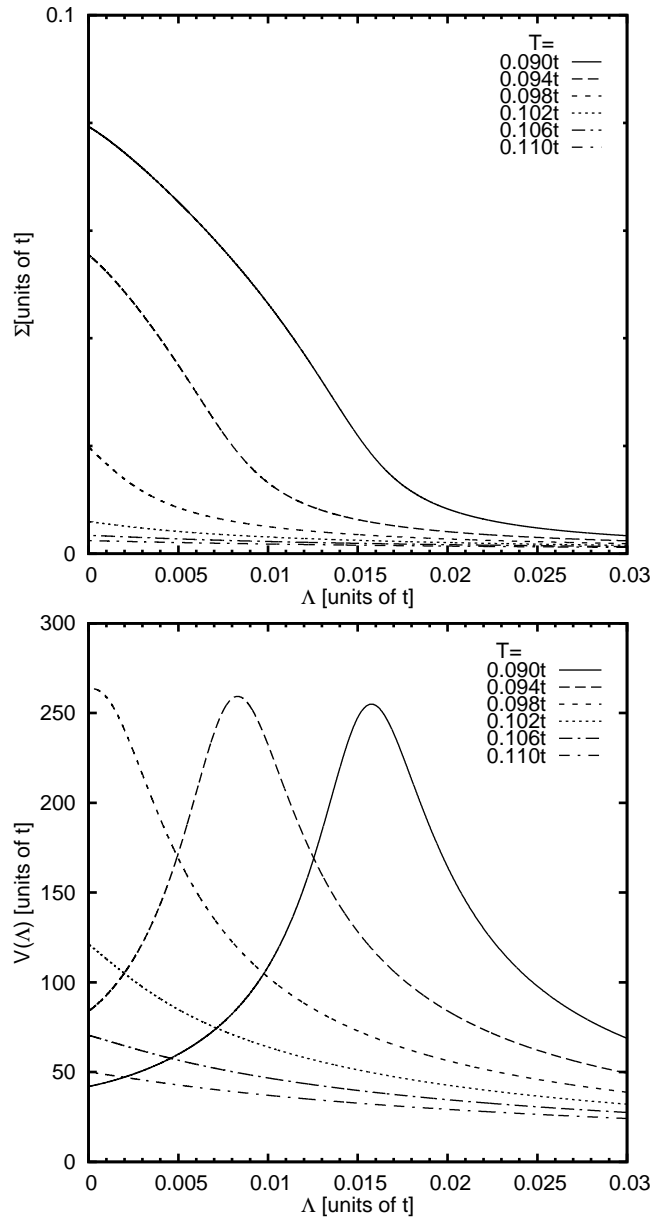


Figure 4.4: Flows of the self-energy Σ and the effective interaction V plotted against Λ for temperatures around the transition, $V_0 = 2t$ and $\Delta_{\text{ext}} = 10^{-4}t$. $\rho_0 = 1/2\pi$ for all numerical calculations.

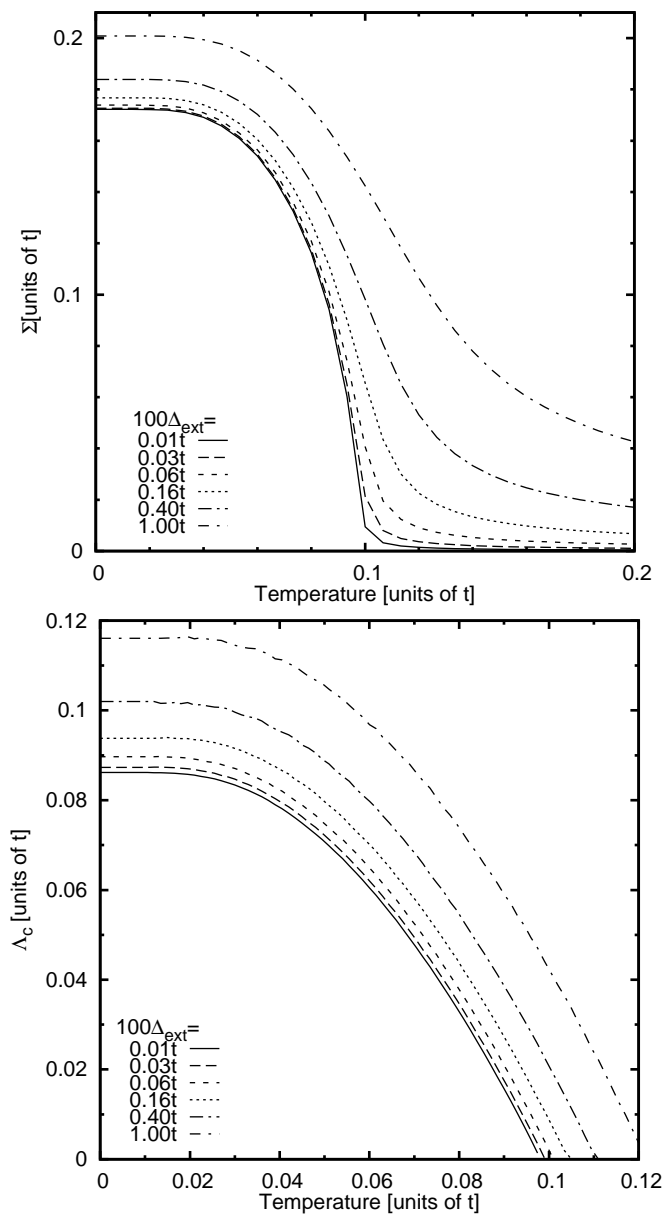


Figure 4.5: (top) Self-energy against temperature calculated using fRG methods for $V_0 = 2t$ and small to intermediate Δ_{ext} . Minute deviations in comparison to Fig. 2.2 are due to numerical errors in the integration of the fRG differential equations. (bottom) Position of the maximum of the cutoff-dependent effective interaction against temperature for small to intermediate Δ_{ext} . $\rho_0 = 1/2\pi$ for all numerical calculations.

to the resummation treatment case (see the upper part of Fig. 2.2), we cannot set Δ_{ext} to zero as the effective interaction would diverge before the flow reaches $\Lambda_f = 0$. However, the upper part of Fig. 4.3 implies that $\lim_{\Delta_{\text{ext}} \rightarrow 0} \Sigma_{\Delta_{\text{ext}}}(\Lambda)$ exists and is approached in a continuous fashion. For $T > 0$, if $\Delta_{\text{ext}} \approx \Sigma(\Lambda_f)/100$, there is a clearly observable steep rise of $\Sigma(T)$ (see the upper part of Fig. 4.4) which would permit a fairly precise determination of T_c even in models with complexity beyond what is studied here. However, note that for such Δ_{ext} , the effective interaction reaches maximal values $\sim 100t$ in the flow. This is much larger than the bandwidth of low-dimensional systems (see, e.g., the lower part of Fig. 4.6 for the temperature evolution). The agreement between fRG and mean-field results in spite of these large effective interactions underlines that the truncated fRG is exact for our model.

Close to the T -dependent critical scale Λ_c , the effective interaction reaches a maximum whose height depends singularly on Δ_{ext} (see Fig. 4.6, lower panel). A numerical analysis shows that the maximal effective interaction is $\propto 1/\Delta_{\text{ext}}^\alpha$ with $\alpha \approx 2/3$. The values for the maximal effective interaction can be read off for $T = 0$ in Fig. 4.3 (bottom) and for finite temperatures in the lower part of Fig. 4.6. For a direct application of the method to non-mean-field models, the maximum of the effective interaction must be restricted to smaller values. Otherwise, the small-interaction approximation from section 3.6 is not justified. However, a larger Δ_{ext} entails that the rise of $\Sigma_{\Lambda=0}(T)$ at T_c gets smeared out strongly (see Fig. 4.5 (upper part) and Fig. 2.2 (upper part)). The upper part of Fig. 4.6 shows that far below T_c , the relative error $\Delta\Sigma/\Sigma$ is linear in Δ_{ext} . At the highest considered Δ_{ext} , it is already of the order of 0.1 while $V(\Lambda_c)$ is still $\approx 10t$. This implies that the method we employ could be improved in the closely intertwined areas of effective interaction suppression and gap value accuracy, as will be attempted in the next section.

4.2 First-order phase transitions

In this section, we describe and apply an extension of the one-particle irreducible (1PI) fermionic functional renormalization group (fRG) scheme as formalized by Salmhofer and Honerkamp (2001) permitting the study of first-order phase transitions and hysteresis phenomena. We show how this constitutes an improvement of the capabilities of the method as introduced in chapter 3 and applied in section 4.1. The extension also allows us to circumvent the rise of large interactions at intermediate scales which has plagued the approach so far while preserving the accuracy of the results for the gap. As above, we start from the flow equations as suggested by Katanin (2004), derived in section 3.6, studied for the case of the breaking of a continuous symmetry in Salmhofer et al. (2004) and for the case of the breaking of a discrete symmetry in section 4.1, see Gersch et al. (2005). We use the interaction flow by Honerkamp et al. (2004), which permits the fruitful employment of counterterms as introduced in section 4.2.1. We show flows for first-order (section 4.2.2) and second-order (section 4.2.3) phase transitions, dis-

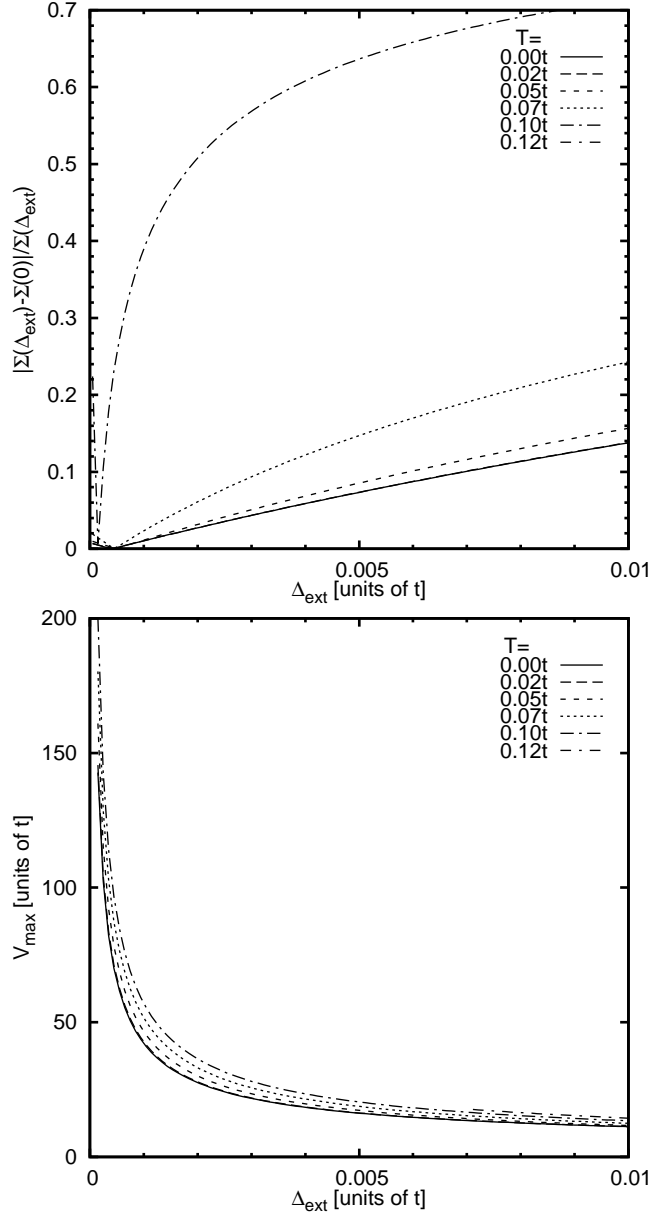


Figure 4.6: (top) Relative deviation of the fRG-derived self-energy from the value without external field against the initial anomalous self-energy for temperatures from $T = 0$ to just above T_c . The values for $T = 0.12t$ are 1 and thus not visible in the selected range. (bottom) Maximal value of the effective interaction during the flow against the initial anomalous self-energy for temperatures from zero to just above T_c .

Discussing the effect of the counterterm on possible approximations. We also study the effect of an external field on the flow, identifying a criterion for unphysical starting points.

4.2.1 Renormalization group setup with counterterm

The basic setup of a 1PI fRG calculation with Katanin's modification is outlined in 4.1.1 and for the reduced BCS model by Salmhofer et al. (2004). To understand the problem solved in the following, we consider the order-parameter dependence of the thermodynamic potential Ω in the plot for $\mu = 0$ in Fig. 2.6. Following the lead of Salmhofer et al. (2004); Gersch et al. (2005), a small external field is included as the initial condition for the order parameter in section 4.1. This external field is relevant in Wilson's fixed-point picture (Wilson (1971a,b)), but does not appreciably change the physics away from critical scales. It biases the fRG flow toward the thermodynamic potential minimum at finite $\Delta_{i.a.}$ (see the $\mu = 0$ graph in Fig. 2.6), which becomes the endpoint of the flow. This method is unable to deal with first-order phase transitions where the thermodynamically stable state is separated from the symmetric state by an energy barrier. A thermodynamic potential as function of the order parameter illustrating this situation is depicted in the plot for $\mu = -0.2t$ in Fig. 2.6. Because the external field must be small, the flow always veers toward the symmetric minimum at zero order parameter, following the gradient of the thermodynamic potential. Other minima are inaccessible, even if their thermodynamic potentials are smaller. Furthermore, the method cannot be used to study hysteresis effects appearing if systems exhibiting second-order phase transitions (see the graphs for $\mu = 0$ and $\mu = -0.1t$ in Fig. 2.6) are placed in an external field. The external field destroys the axis symmetry of $\Omega(\Delta_{i.a.})$, but always biases the flow toward the global minimum of the thermodynamic potential, making it impossible to study the metastable configuration. Thus, the challenge encountered here is to set up an fRG scheme with a parameter that allows the selection of any stable or metastable configuration as the endpoint of the flow.

The basic idea that will be exploited in the following is to include in the calculation a counterterm Δ_c of arbitrary strength that cancels an equally strong external field Σ_i as introduced in (2.14), but only at the end of the flow. In the fRG calculation, the external field is taken into account as the initial value of the order parameter Σ , while the counterterm Δ_c is included in the bare propagator. Schematically, the matrix Green's function of the system reads

$$\mathbb{G}^{-1} = \frac{\mathbb{Q}_0 + \Delta_c}{\chi} - \Sigma, \quad (4.10)$$

where χ is the cutoff function and \mathbb{Q}_0 is the inverse bare propagator without counterterm. For any degree of freedom with $\chi \neq 1$, counterterm and self-energy do not cancel each other. However, the special case $\chi \equiv 1$ is approached at the end of the fRG flow. Thus, the effective action of the original symmetric model is recovered.

We first consider the case of $\chi = \chi_\Lambda(\mathbf{k})$ describing the sharp momentum-shell cutoff of conventional RG schemes (see Wilson (1971b, 1972); Wegner and Houghton (1973) and (4.1) of section 4.1.1). In this case, only momenta for which $\chi_\Lambda(\mathbf{k}) = 1$ are taken into account in the RG flow. For these momenta, Δ_c and Σ cancel exactly at the start of the flow, causing Σ to remain stationary. This is due to the right-hand side of the 1PI flow equation for the order parameter being proportional to the anomalous part of the Green's function (compare (4.7)) which vanishes if Δ_c and Σ cancel. This argument generalizes to the case of multiple order parameters, as can be seen by considering the adjugate matrix of the inverse Green's function, which is schematically similar to (4.10) but with multiple different counterterms and self-energies in the spirit of section 3.1. Consequently, Δ_c and Σ also cancel at all stages of the flow. In the case of a second-order transition, the fRG diverges at a $\Lambda_c \neq \Lambda_f$ as no gap opens in the spectrum and small energy denominators appear. In the case of a first-order transition, the flow remains finite, incorrectly suggesting that the symmetric phase is stable. We conclude that we have to employ a softer cutoff function.

Next, we consider the softest possible cutoff function, provided by the interaction flow introduced by Honerkamp et al. (2004). It works by linearly turning on the interaction with the flow parameter (note the similarity to the treatment by Mahan (2000), from page 148) while turning on the counterterm with the square root of the flow parameter. By rescaling the fields, this is found to be equivalent to employing a cutoff function χ which is constant at all momenta, zero at the start of the flow, one at the end of the flow, and

$$\chi = \sqrt{\Lambda} \quad (4.11)$$

in between. With this, the counterterm and the external field in (4.10) cancel only at the end of the flow, and all configurations become accessible, as is illustrated in the following.

We prepare to evaluate the flow equation diagrams in Fig. 4.1. For a general cutoff function χ , we obtain from (2.16) the cut-off Green's function \mathbb{G} for the Hamiltonian (2.14):

$$\mathbb{G}(i\omega_n, \mathbf{k}) = \frac{\chi}{-(i\omega_n + \mu)^2 + E_{\mathbf{k}}^2} \begin{pmatrix} -i\omega_n - \varepsilon_{\mathbf{k}} - \mu & -\chi\Sigma + \Delta_c \\ -\chi\Sigma + \Delta_c & -i\omega_n + \varepsilon_{\mathbf{k}} - \mu \end{pmatrix}, \quad (4.12)$$

where $E_{\mathbf{k}} = \sqrt{\varepsilon_{\mathbf{k}} + \Delta_{\text{eff}}^2}$ and $\Delta_{\text{eff}} = \chi\Sigma - \Delta_c$. The external field Δ_{ext} inducing a charge-density wave as well as Σ_i are to be absorbed in the initial condition for Σ . To facilitate the use of Morris' lemma (3.19) of Morris (1994), we prepare to employ $\mathbb{S} = \dot{\chi} \frac{\partial \mathbb{G}}{\partial \chi}$ (see (4.6)) by calculating

$$\begin{aligned} \frac{\partial \mathbb{G}}{\partial \chi}(i\omega_n, \mathbf{k}) &= \frac{1}{-(i\omega_n + \mu)^2 + E_{\mathbf{k}}^2} \begin{pmatrix} -i\omega_n - \varepsilon_{\mathbf{k}} - \mu & -\chi\Sigma - \Delta_{\text{eff}} \\ -\chi\Sigma - \Delta_{\text{eff}} & -i\omega_n + \varepsilon_{\mathbf{k}} - \mu \end{pmatrix} \\ &\quad - \frac{2\Sigma\Delta_{\text{eff}}\chi}{(-(i\omega_n + \mu)^2 + E_{\mathbf{k}}^2)^2} \begin{pmatrix} -i\omega_n - \varepsilon_{\mathbf{k}} - \mu & -\Delta_{\text{eff}} \\ -\Delta_{\text{eff}} & -i\omega_n + \varepsilon_{\mathbf{k}} - \mu \end{pmatrix}. \end{aligned} \quad (4.13)$$

To evaluate the tadpole of Fig. 4.1, we sum an off-diagonal entry of (4.13) over the Matsubara frequencies ω_n :

$$\begin{aligned}
 T \sum_{\omega_n} \frac{\partial \mathbb{G}_{12}}{\partial \chi} &= (-\chi \Sigma - \Delta_{\text{eff}}) \frac{1}{2E} (f(E^-) - f(E^+)) \\
 &\quad + \Sigma \Delta_{\text{eff}}^2 \chi \frac{1}{2E^2} \left(\frac{1}{E} (f(E^-) - f(E^+)) + f'(E^+) + f'(E^-) \right) \\
 &= \frac{f(E^-) - f(E^+)}{2E} \left(-\chi \Sigma \frac{\varepsilon^2}{E^2} - \Delta_{\text{eff}} \right) \\
 &\quad + \frac{f'(E^+) + f'(E^-)}{2E^2} \chi \Sigma \Delta_{\text{eff}}^2, \tag{4.14}
 \end{aligned}$$

where $f(E) = (\exp(E/T) + 1)^{-1}$ is the Fermi distribution and (B.14) and (B.15) are used in the first equality. Tracing over the momentum degrees of freedom, multiplying with the effective interaction and diagrammatic factors as well as plugging in $\chi = \sqrt{\Lambda}$ in accordance with (4.11), we obtain the flow equation

$$\begin{aligned}
 \dot{\Sigma} &= -V \int \frac{d^d k}{(2\pi)^d} \frac{1}{4\sqrt{\Lambda}} \left\{ \frac{f(E^-) - f(E^+)}{E} \left[\sqrt{\Lambda} \Sigma \frac{\varepsilon^2}{E^2} + \Delta_{\text{eff}} \right] \right. \\
 &\quad \left. - \frac{f'(E^-) + f'(E^+)}{E^2} \sqrt{\Lambda} \Sigma \Delta_{\text{eff}}^2 \right\}. \tag{4.15}
 \end{aligned}$$

Turning to the loop diagram of Fig. 4.1, we trace over the Nambu index of the product of $\mathbb{G}(i\omega_n, \mathbf{k})$ and $\mathbb{G}(i\omega_n, \mathbf{k} + \mathbf{Q})$, making use of the nesting condition $\varepsilon_{\mathbf{k}} = -\varepsilon_{\mathbf{k}+\mathbf{Q}}$ to obtain

$$\begin{aligned}
 &\frac{2\chi^2}{(-i\omega_n + \mu)^2 + E_{\mathbf{k}}^2} [(i\omega_n + \varepsilon_{\mathbf{k}} + \mu)(i\omega_n - \varepsilon_{\mathbf{k}} + \mu) + \Delta_{\text{eff}}^2] \\
 &= \frac{-2\chi^2}{\omega_n^2 + (E^+ + E^-)i\omega_n - E^+E^-} + \frac{4\chi^2 \Delta_{\text{eff}}^2}{(\omega_n^2 + (E^+ + E^-)i\omega_n - E^+E^-)^2}.
 \end{aligned}$$

Performing the Matsubara sum according to (B.14) and (B.15) yields

$$2\chi^2 \left[-\frac{f(E^-) - f(E^+)}{2E} \frac{\varepsilon^2}{E^2} + \frac{f'(E^-) + f'(E^+)}{2E^2} \Delta_{\text{eff}}^2 \right]. \tag{4.16}$$

To complete the evaluation of the loop diagram of Fig. 4.1, we substitute $\sqrt{\Lambda}$ for χ , differentiate (4.16) with respect to Λ , multiply with V^2 , trace over the momentum degrees of freedom and include diagrammatic factors to obtain

$$\begin{aligned}
 \dot{V} &= -V^2 \int \frac{d^d k}{(2\pi)^d} \frac{1}{2E^2} \left\{ \frac{f(E^-) - f(E^+)}{E} \varepsilon^2 \left(3\Lambda \frac{\dot{E}}{E} - 1 \right) + \right. \\
 &\quad \left. (f'(E^-) + f'(E^+)) \left(3\varepsilon^2 \Lambda \frac{\dot{E}}{E} + \Delta_{\text{eff}}^2 \right) \right. \\
 &\quad \left. - (f''(E^-) + f''(E^+)) \Lambda \Delta_{\text{eff}}^2 \dot{E} \right\}. \tag{4.17}
 \end{aligned}$$

We furthermore need to calculate the thermodynamic potential using the functional renormalization group. From the flow equation (3.25) for γ_0 and the relation $\Omega_{\text{i.a.}} = T\gamma_0$ for the thermodynamic potential Ω , we construct

$$\dot{\Omega} = -\frac{T}{2}\text{Tr}\left(\Sigma\frac{\dot{\chi}}{\chi}\mathbf{G}\right). \quad (4.18)$$

If the flow is started at the thermodynamic potential of the non-interacting system, the full thermodynamic potential is recovered. Since we will always do so, we have written Ω instead of $\Omega_{\text{i.a.}}$ in (4.18). Evaluating the Matsubara sums, (4.18) reads

$$\dot{\Omega} = \int \frac{d^d k}{(2\pi)^d} \Sigma \Delta_{\text{eff}} \frac{f(E^-) - f(E^+)}{4E\sqrt{\Lambda}}. \quad (4.19)$$

(4.15), (4.17), and (4.19) constitute a closed system of integro-differential equations which can be numerically solved given appropriate initial conditions.

4.2.2 Flows for first-order phase transitions

We consider a system exhibiting a first-order phase transition at a transition temperature T_t . Our example is (2.14) at $\mu = 0.245t$, which exhibits a first-order phase transition in temperature according to the phase diagram in Fig. 2.3. Studying flows below T_t (see Fig. 4.7), we notice two strong attractors. By its lower thermodynamic potential at the end of the flow, one of them can be identified with the stable, symmetry-broken configuration. The values for the order parameter, effective interaction, and thermodynamic potential difference reproduce the exact mean-field results. Note that the final values do not depend on the magnitude of the counterterm. This means that the dependence of the results on the external field, known from sections 2.1.3, 2.2.3, 4.1.4, and 4.1.5 as well as Gersch et al. (2005); Dupuis (2005); Salmhofer et al. (2004), is eliminated. This is an advantage of the procedure introduced here.

Considering Fig. 4.7(a), we see that there is a separatrix between the effective gap flows to the metastable configuration and the flows to the stable configuration. The distances between the gap flows for different counterterm values decrease monotonically with increasing cutoff. The flows contract onto a single point. In models more complicated than (2.14), this contraction will no longer lead to a single point due to the approximations which become necessary, but the strength of the contraction can be interpreted as a measure of the approximations' quality. Here, those flows which exhibit weak changes of the effective interaction away from $\Lambda = 1$ and weak changes of the order parameter close to $\Lambda = 1$ are most promising for determining order parameters in more complicated models. We see that the flows closest to the separatrix are not optimal flows since $\Delta(\Lambda)$ still shows a large slope at $\Lambda = 1$. This final slope is smallest for a counterterm of roughly twice the magnitude of the order parameter. Such a flow would yield an excellent approximation of the order parameter, even if it were to be stopped at $\Lambda = 0.75$.

Considering the flows of the effective interaction in diagram 4.7(b), we do not find a separatrix as in (a). Instead, the flows corresponding to the ones close to the

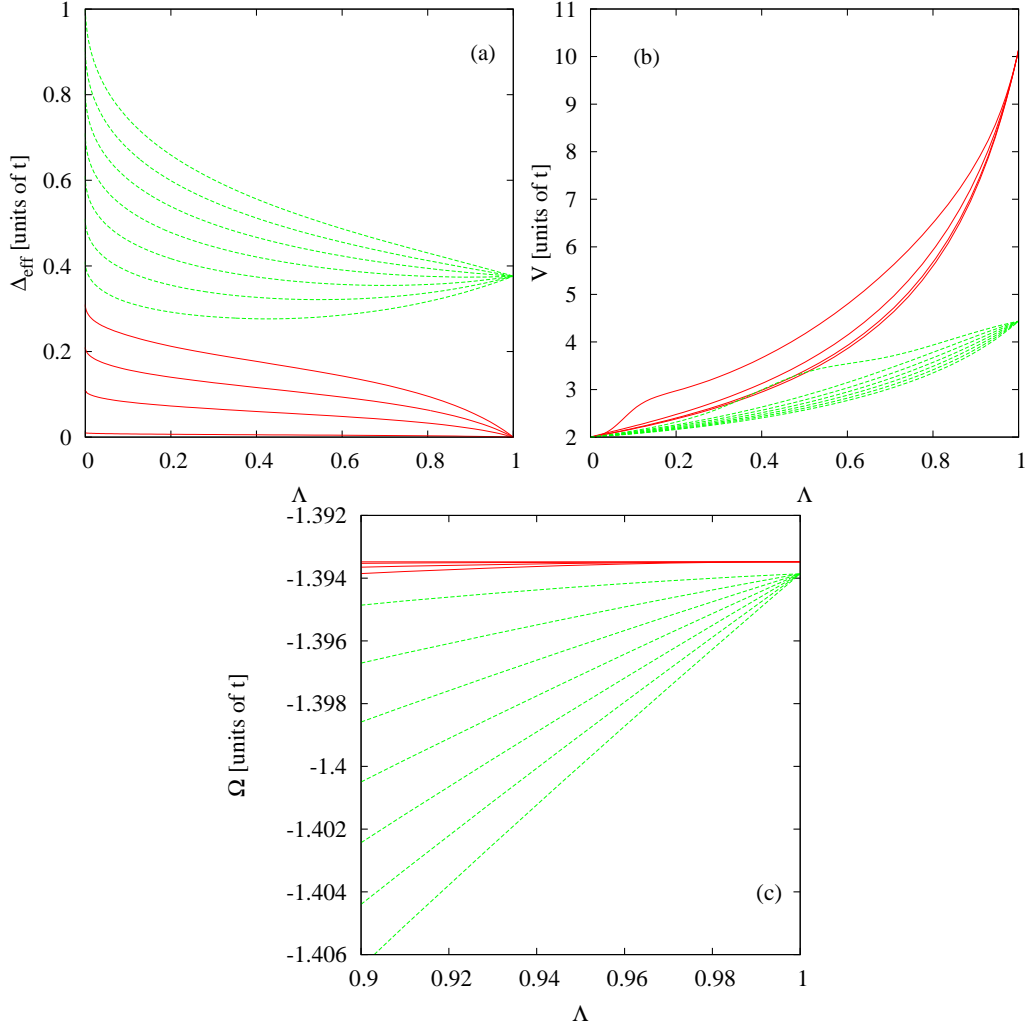


Figure 4.7: Flows for $V_0 = 2t$ at $\mu = 0.245t$, $T = 0.01t < T_t$, and Δ_c increasing from $0.01t$ to $1.01t$ in increments of $0.1t$. Broken lines denote flows converging to the stable symmetry-broken configuration; solid lines denote flows converging to the metastable symmetric configuration. The flow starts at $\Lambda = 0$ and finishes at $\Lambda = 1$. (a) Effective gap Δ_{eff} . Δ_c for each graph can be read off at the y-axis. (b) Effective interaction V . Flows converging at $10.14t$ pass through greater values with increasing counter-term. Flows converging at $4.43t$ behave inversely. (c) Thermodynamic potential Ω . Flows pass through smaller values with increasing counterterm.

separatrix in (a) develop a shoulder which becomes a maximum for certain values of the counterterm (for an example of such a maximum, see diagram 4.8(b)). The flows exhibiting the strongest effective interactions correspond to the flows giving the worst approximations for the order parameter if terminated prematurely. This entails for applications to models where this method is not exact that carefully choosing the counterterm can significantly simplify the calculation and improve the accuracy of the results.

The flows of the thermodynamic potential shown in 4.7(c) again exhibit separatrix behaviour. This is in contrast to the flows above T_t . For the thermodynamic potential, the flows closest to the separatrix yield the best approximations if terminated prematurely. However, it is apparent from 4.7(c) that the flow must be continued until the external field is completely compensated by the counterterm to obtain reliable results for the thermodynamic potential.

Flows above T_t are illustrated in Fig. 4.8. Again, we clearly discern two attractors. In this case, however, the thermodynamic potential flows of the symmetry-broken-phase attractor cross the thermodynamic potential flows of the symmetric-phase attractor. The symmetric phase is therefore thermodynamically more stable. Apart from this, the flows behave similarly as those below T_t . For inconveniently chosen counterterms, the maxima in the effective-interaction flows are clearly visible in 4.8(b). Nevertheless, the flows reproduce the exact mean-field results.

4.2.3 Counterterm flows for second-order phase transitions

The flows for second-order phase transitions behave similarly to the flows for first-order phase transitions, but only a single attractor appears, as can be seen in Fig. 4.9(a). Fig. 4.9(b) shows that it is possible to suppress the effective interaction during the flow by choosing a large counterterm. Approximations for the order parameter can be obtained by stopping the flow before Λ reaches 1. The quality of such an approximation depends on the counterterm chosen. Again, the best approximation can be obtained by choosing a counterterm of twice the non-approximated value of the gap.

4.2.4 External field

If the external field Δ_{ext} in (2.14) is zero, the half-filled system below T_c exhibits two degenerate stable configurations (local minima of the thermodynamic potential) distinguished by the sign of the order parameter. If Δ_{ext} is non-zero, this degeneracy is lifted. The fRG scheme outlined above allows us to select the endpoint of the flow independently of the external field by appropriately setting the counterterm, in contrast to the scheme from section 4.1. The flows toward the metastable configuration are shown in Fig. 4.10 (broken lines). As the external field is increased toward a critical value, the order parameter for the metastable configuration vanishes and the corresponding local minimum of the thermodynamic potential disappears. Beyond this critical value, the flows for negative counterterms become divergent as the effective gap reaches values close to zero, exposing

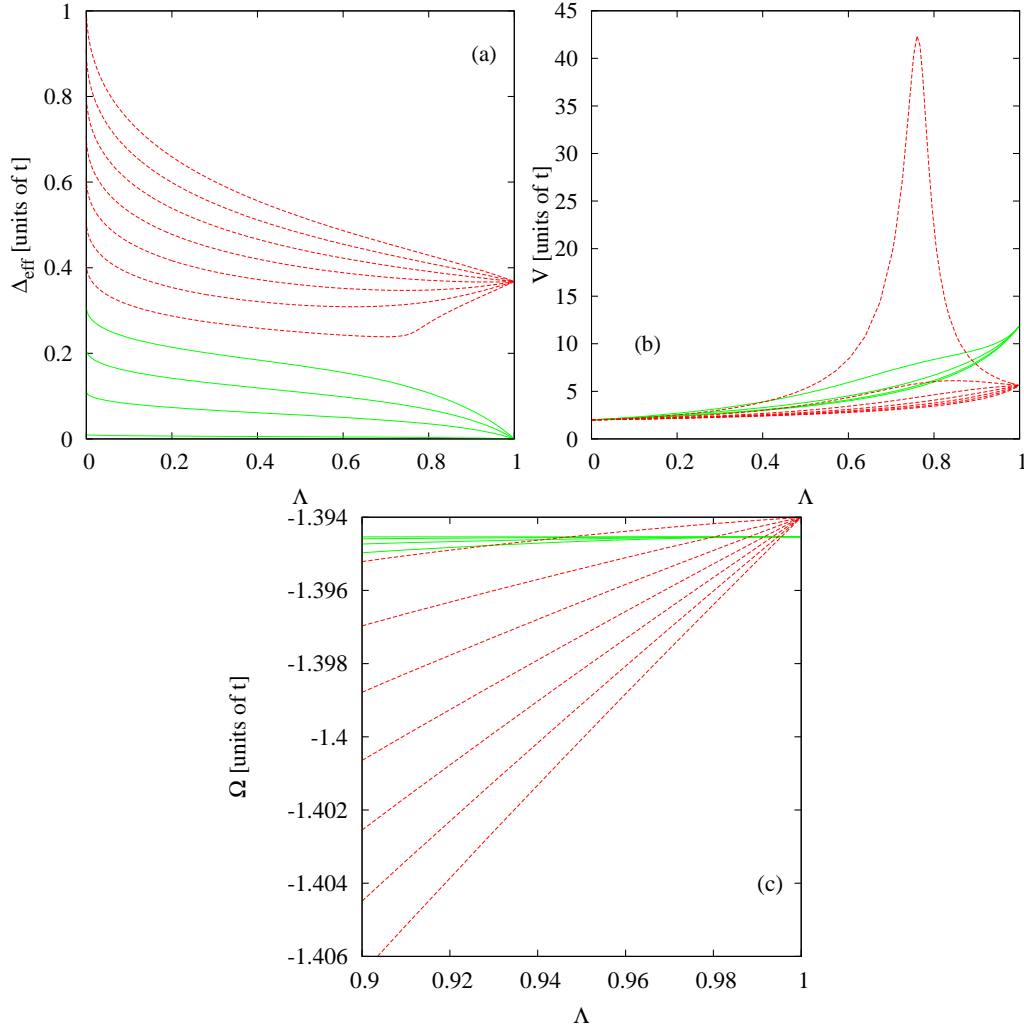


Figure 4.8: Flows for $V_0 = 2t$ at $\mu = 0.245t$, $T = 0.04t > T_t$, and Δ_c increasing from $0.01t$ to $1.01t$ in increments of $0.1t$. Broken lines denote flows converging to the metastable symmetry-broken configuration; solid lines denote flows converging to the stable symmetric configuration. The flow starts at $\Lambda = 0$ and finishes at $\Lambda = 1$. (a) Effective gap Δ_{eff} . Δ_c for each graph can be read off at the y-axis. (b) Effective interaction V . Flows converging at $11.90t$ pass through greater values with increasing counter-term. Flows converging at $5.62t$ behave inversely. (c) Thermodynamic potential Ω . Symmetric flows pass through smaller values with increasing counterterm, and so do symmetry-broken flows.

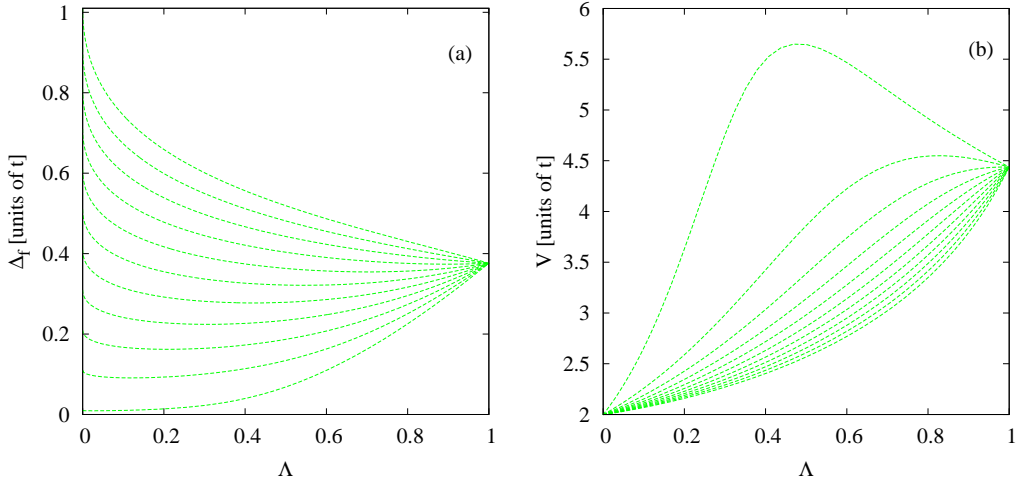


Figure 4.9: Flows for $V_0 = 2t$ at $\mu = 0$, $T \ll T_c$, and Δ_c increasing from $0.01t$ to $1.01t$ in increments of $0.1t$. Broken lines denote flows converging to the stable symmetry-broken configuration. The flow starts at $\Lambda = 0$ and finishes at $\Lambda = 1$. (a) Effective gap Δ_{eff} . Δ_c for each graph can be read off at the y-axis. (b) Effective interaction V . Flows pass through smaller values with increasing counterterm.

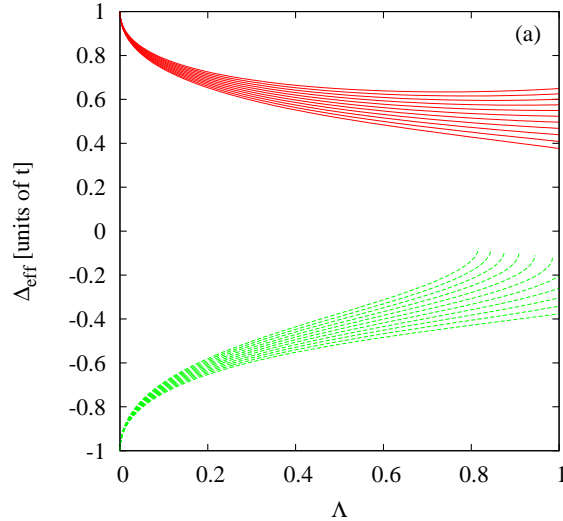


Figure 4.10: Flows of Δ_{eff} at $\mu = 0$ for $V_0 = 2t$. Full (broken) lines have $\Delta_c = (-)t$. The external field increases from 0 to $0.15t$ with increasing final values of the flow. The flow starts at $\Lambda = 0$ and finishes at $\Lambda = 1$.

low-energy modes. Such a divergence can be used as an indicator for an adversely chosen starting point. The flows for positive counterterms (full lines in Fig. 4.10) always attain the stable solution. Calculating the flows as for Fig. 4.10, but for negative values of the external field Δ_{ext} , we obtain the hysteresis curve of Fig. 4.11.

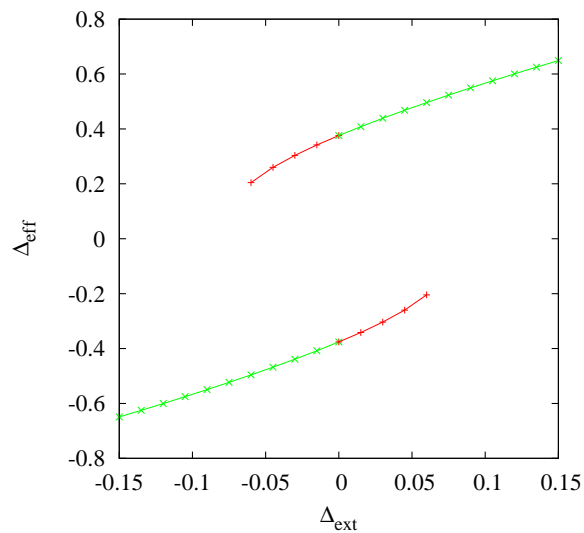


Figure 4.11: Hysteresis effect in an external field. All solutions represent symmetry-broken configurations. Green lines (\times -symbols) represent stable, red lines ($+$ -symbols) metastable configurations.

Chapter 5

Attractive Hubbard model

This chapter has three main goals. First, to study the influence of the $3+1$ anomalous effective interactions arising when Cooper and forward scattering are present in a model. To this end, a reduced model containing only Cooper and forward scattering with zero momentum transfer is solved by a resummation of perturbation theory in section 5.1, which yields analytical formulas for all effective interactions. The same resummation is applied as an approximation to the attractive Hubbard model in two dimensions in section 5.2, allowing us to study the impact of the $3+1$ effective interaction numerically and graphically. The Cooper and forward scattering model is more general in the sense that it permits adjusting the strength of the forward scattering independently of the strength of the Cooper scattering and contains a more general spin structure of the interaction. However, the Hubbard model is more general in the sense that its interaction contains scattering processes with arbitrary momentum transfer. Turning to the fRG treatment, we discuss in section 5.3 the momentum-shell flows of the $3+1$ anomalous effective interactions for the attractive Hubbard model. The second goal is to study fRG flows in the Katanin truncation for a non-mean-field model. This is undertaken in sections 5.3.3 and 5.3.4, comparing the momentum-shell flow with the interaction flow. The third goal is to find results for the superconducting order parameter in the attractive Hubbard model at zero temperature in two dimensions. This is accomplished in section 5.3.5, where we obtain values comparable to the literature by employing the interaction-flow procedure.

5.1 Resummation approach to Cooper and forward scattering

We commence our study of the $3+1$ effective interactions by studying the impact of the inclusion of forward scattering processes on a reduced BCS model for superconductivity. In reduced BCS models where the electrons only interact in the Cooper channel, anomalous effective interactions which have four incoming or four outgoing legs appear in addition to the regular vertices with two incoming and two outgoing legs. As we shall see, the additional inclusion of forward scattering

gives rise to anomalous two-particle effective interactions sporting three incoming or outgoing legs. Origin, strength, and impact of these scattering processes are discussed below.

5.1.1 Fermions with Cooper and forward scattering

To restrict ourselves to the study of a system containing only Cooper and forward scattering, we start from the Hamiltonian

$$H = \sum_{\mathbf{k}} \sum_s \varepsilon_{\mathbf{k}} c_{\mathbf{k}s}^\dagger c_{\mathbf{k}s} \quad (5.1)$$

$$- \frac{1}{N} \sum_{\mathbf{k}_1 \mathbf{k}_2} V_0(\mathbf{k}_1 \mathbf{k}_2) c_{-\mathbf{k}_2 \downarrow}^\dagger c_{\mathbf{k}_2 \uparrow}^\dagger c_{\mathbf{k}_1 \uparrow} c_{-\mathbf{k}_1 \downarrow} \quad (5.2)$$

$$- \frac{1}{2N} \sum_{\mathbf{k}_1 \mathbf{k}_2} \sum_{s_1, s_2} U_0(\mathbf{k}_1 \mathbf{k}_2) c_{\mathbf{k}_1 s_1}^\dagger c_{\mathbf{k}_1 s_1} c_{\mathbf{k}_2 s_2}^\dagger c_{\mathbf{k}_2 s_2} \quad (5.3)$$

$$+ \sum_{\mathbf{k}} \left(\Delta_{\text{ext}}(\mathbf{k}) c_{-\mathbf{k} \downarrow}^\dagger c_{\mathbf{k} \uparrow}^\dagger + \Delta_{\text{ext}}^*(\mathbf{k}) c_{\mathbf{k} \uparrow} c_{-\mathbf{k} \downarrow} \right). \quad (5.4)$$

c and c^\dagger are fermionic annihilation and creation operators, respectively, (5.1) is a kinetic energy term, (5.2) is a singlet-channel Cooper scattering term, (5.3) describes spin-independent forward scattering with zero momentum transfer, and (5.4) describes the coupling of an external pairing field to the system. (5.2) and (5.3) thus form the interaction part of the Hamiltonian.

Passing to a functional integral formulation within the Matsubara formalism at nonzero temperature T as in (2.6) and (3.1), we obtain the grand canonical action

$$S = \sum_k \sum_s (i\omega_n - \xi_{\mathbf{k}}) \bar{\psi}_{ks} \psi_{ks} \quad (5.5)$$

$$+ \sum_{\mathbf{k}_1, \mathbf{k}_2} \sum_{n_1, n_2, n_3} V_0(\mathbf{k}_1 \mathbf{k}_2) \bar{\psi}_{n_1 - \mathbf{k}_2 \downarrow} \bar{\psi}_{n_2 \mathbf{k}_2 \uparrow} \psi_{n_3 \mathbf{k}_1 \uparrow} \psi_{n_4 - \mathbf{k}_1 \downarrow} \quad (5.6)$$

$$+ \sum_{\mathbf{k}_1, \mathbf{k}_2} \sum_{n_1, n_2, n_3} \sum_{s_1, s_2} \frac{1}{2} U_0(\mathbf{k}_1 \mathbf{k}_2) \bar{\psi}_{n_1 \mathbf{k}_1 s_1} \psi_{n_2 \mathbf{k}_1 s_1} \bar{\psi}_{n_3 \mathbf{k}_2 s_2} \psi_{n_4 \mathbf{k}_2 s_2} \quad (5.7)$$

$$- \sum_k \left(\Delta_{\text{ext}}(\mathbf{k}) \bar{\psi}_{-k \downarrow} \bar{\psi}_{k \uparrow} + \Delta_{\text{ext}}^*(\mathbf{k}) \psi_{k \uparrow} \psi_{-k \downarrow} \right), \quad (5.8)$$

where n_4 is chosen so that energy is conserved and ψ and $\bar{\psi}$ are the Grassmann fields matching c and c^\dagger , respectively. The sign is chosen such that $-S$ appears in the exponent of the functional integral for the partition sum, as in (3.1) and (2.6). We substitute

$$\bar{\phi}_{k+} = \bar{\psi}_{k \uparrow}, \quad \phi_{k+} = \psi_{k \uparrow}, \quad \phi_{k-} = \bar{\psi}_{-k \downarrow}, \quad \bar{\phi}_{k-} = \psi_{-k \downarrow}, \quad (5.9)$$

similarly to the general scheme (3.4) outlined in section 3.1, and obtain for the

interaction parts (5.6) and (5.7) of the action:

$$\begin{aligned}
 & - \sum_{\mathbf{k}_1, \mathbf{k}_2} \sum_{n_1, n_2, n_3} \left\{ V_0(\mathbf{k}_1 \mathbf{k}_2) \bar{\phi}_{\mathbf{k}_1 -} \bar{\phi}_{\mathbf{k}_2 +} \phi_{\mathbf{k}_1 +} \phi_{\mathbf{k}_2 -} + \right. \\
 & \left. \sum_{N_1 = \pm, N_2 = \pm} N_1 N_2 \frac{1}{2} U_0(\mathbf{k}_1 \mathbf{k}_2) \bar{\phi}_{\mathbf{k}_1 N_1} \bar{\phi}_{\mathbf{k}_2 N_2} \phi_{\mathbf{k}_1 N_1} \phi_{\mathbf{k}_2 N_2} \right\}, \quad (5.10)
 \end{aligned}$$

where we have suppressed the Matsubara frequencies in the notation for brevity. Note that because we have absorbed the spin degree of freedom into the Nambu index, there is no multiple-counting of degrees of freedom, implying that the compensating factor ν from section 3.1 is 1.

To simplify the necessary antisymmetrization of the vertex, we rewrite (5.10) by furnishing each ϕ with its own momentum/energy and Nambu index, which necessitates introducing additional sums and Kronecker deltas. We organize the four Nambu indices into one multiindex \mathbf{N} , write $(\pm \pm \pm \pm) := \delta_{N_1 \pm} \delta_{N_2 \pm} \delta_{N_3 \pm} \delta_{N_4 \pm}$, and abbreviate $\phi_{k_i N_i} = \phi_i$ as well as $\bar{\phi}_{k_i N_i} = \bar{\phi}_i$. Thereby, (5.10) becomes:

$$\begin{aligned}
 & - \sum_{k_1 \dots k_4, \mathbf{N}} \delta_{n_1 + n_2, n_3 + n_4} \delta_{\mathbf{k}_1 \mathbf{k}_3} \delta_{\mathbf{k}_2 \mathbf{k}_4} \bar{\phi}_1 \bar{\phi}_2 \phi_3 \phi_4 \times \\
 & \quad \left\{ V_0(\mathbf{k}_1 \mathbf{k}_2) (- + + -) + \frac{1}{2} U_0(\mathbf{k}_1 \mathbf{k}_2) N_1 N_2 \delta_{N_1 N_3} \delta_{N_2 N_4} \right\} \\
 & = -\frac{1}{4} \sum_{k_1 \dots k_4, \mathbf{N}} \delta_{n_1 + n_2, n_3 + n_4} \bar{\phi}_1 \bar{\phi}_2 \phi_3 \phi_4 \times \\
 & \quad \left\{ [V_0(\mathbf{k}_1 \mathbf{k}_2) ((- + + -) + (+ - - +))] \right. \\
 & \quad + U_0(\mathbf{k}_1 \mathbf{k}_2) N_1 N_2 \delta_{N_1 N_3} \delta_{N_2 N_4}] \delta_{\mathbf{k}_1 \mathbf{k}_3} \delta_{\mathbf{k}_2 \mathbf{k}_4} \\
 & \quad - [V_0(\mathbf{k}_1 \mathbf{k}_2) ((+ - + -) + (- + - +))] \\
 & \quad \left. + U_0(\mathbf{k}_1 \mathbf{k}_2) N_1 N_2 \delta_{N_1 N_4} \delta_{N_2 N_3}] \delta_{\mathbf{k}_1 \mathbf{k}_4} \delta_{\mathbf{k}_2 \mathbf{k}_3} \right\}.
 \end{aligned}$$

We introduce the bare four-point function,

$$\begin{aligned}
 \mathbb{V}_0(1234) & = \delta_{n_1 + n_2, n_3 + n_4} \left\{ [V_0(\mathbf{k}_1 \mathbf{k}_2) ((- + + -) + (+ - - +))] \right. \\
 & \quad + U_0(\mathbf{k}_1 \mathbf{k}_2) N_1 N_2 \delta_{N_1 N_3} \delta_{N_2 N_4}] \delta_{\mathbf{k}_1 \mathbf{k}_3} \delta_{\mathbf{k}_2 \mathbf{k}_4} \\
 & \quad - [V_0(\mathbf{k}_1 \mathbf{k}_2) ((+ - + -) + (- + - +))] + \\
 & \quad \left. U_0(\mathbf{k}_1 \mathbf{k}_2) N_1 N_2 \delta_{N_1 N_4} \delta_{N_2 N_3}] \delta_{\mathbf{k}_1 \mathbf{k}_4} \delta_{\mathbf{k}_2 \mathbf{k}_3} \right\}, \quad (5.11)
 \end{aligned}$$

where we have written i instead of $k_i N_i$ in the argument of \mathbb{V}_0 . For the calculation of the $\delta_{\mathbf{p}_1 \mathbf{p}_3}$ -part of the effective interaction, the bare four-point function is most conveniently written in matrix form,

$$\mathbb{V}_0(\mathbf{k}_1 \mathbf{k}_2) = \begin{pmatrix} U_0(\mathbf{k}_1 \mathbf{k}_2) & 0 & 0 & -U_0(\mathbf{k}_1 \mathbf{k}_2) \\ 0 & 0 & V_0(\mathbf{k}_1 \mathbf{k}_2) & 0 \\ 0 & V_0(\mathbf{k}_1 \mathbf{k}_2) & 0 & 0 \\ -U_0(\mathbf{k}_1 \mathbf{k}_2) & 0 & 0 & U_0(\mathbf{k}_1 \mathbf{k}_2) \end{pmatrix} \quad (5.12)$$

where momentum and energy conservation are shifted into the diagrammatics, N_1 is paired with N_3 , N_2 with N_4 , and the base

$$\{(--), (-+), (+-), (++)\}$$

illustrated in Fig. 5.7 is used. The notation $(\pm\pm)$ is defined in analogy to the parentheses with four signs introduced above. A contribution proportional to $\delta_{\mathbf{k}_1\mathbf{k}_2}$ is neglected as it lives on a set of degrees of freedom with dimensionality reduced in comparison to the set of degrees of freedom on which \mathbb{V}_0 lives. Note that the rank of \mathbb{V}_0 is three, which makes it possible to reduce the number of equations determining the effective interactions as is done in section 5.1.4.

Rewritten using the substitution (5.9), the quadratic parts (5.5) and (5.8) of the action akin to the quadratic parts (5.1) and (5.4) of the Hamiltonian can be written in a form amenable to the usual treatment of functional integrations via Wick's theorem (Negele and Orland (1998) page 75):

$$\sum_{k_1 k_2, N_1 N_2} \bar{\phi}_1 \phi_2 \delta_{k_1 k_2} \left\{ \underbrace{[i\omega_{n_1} - \xi_{\mathbf{k}_1}]}_{=\mathbb{Q}_{++}}(++) + \underbrace{[i\omega_{n_1} + \xi_{-\mathbf{k}_1}]}_{=\mathbb{Q}_{--}}(--) \right. \\ \left. - \underbrace{\Delta_{\text{ext}}(\mathbf{k}_1)}_{=-\mathbb{Q}_{+-}}(+-) - \underbrace{\Delta_{\text{ext}}^*(\mathbf{k}_1)}_{=-\mathbb{Q}_{-+}}(-+) \right\}.$$

This identifies the matrix \mathbb{Q} from the formalism taking into account symmetry breaking introduced in section 3.1, see (3.3). In order to find an explicit form of the full propagator, we determine the normal and anomalous self-energy in the next section.

5.1.2 Gap equation

Commanding the diagrammatically simple antisymmetrized bare four-point function (5.11)/(5.12), in this section we show by a diagrammatic resummation that mean-field theory is exact in the thermodynamic limit for the Hamiltonian specified by (5.1)+(5.2)+(5.3)+(5.4). We can employ Hugenholtz diagrammatics (see Negele and Orland (1998) chapter 2.3), as there are no anomalous expectation values in the ϕ -fields. Propagators anomalous in the ψ -fields are normal in the ϕ -fields: $\langle \phi_+ \bar{\phi}_- \rangle = \langle \psi \psi \rangle$. Diagrammatically, the perturbation expansion for the self-energy is shown in the first row of Fig. 5.1. It consists of a sum of all diagrams obtained by connecting bubbles via bare interaction vertices. This is due to the following argument, which proceeds in analogy to the one in section 2.1.2. An overlap between two loops removes one integration over all degrees of freedom due to the reduced momentum structure of the interaction (5.2)+(5.3). This diminishes the contribution of such a diagram by a factor proportional to the inverse system size in comparison with the diagrams actually drawn here. The diagrams which contribute in leading order in the system size can thus be resummed as shown in

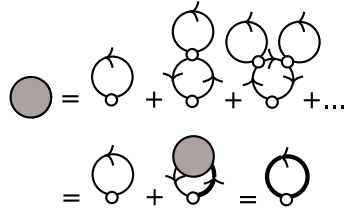


Figure 5.1: Perturbation expansion for the self-energy. Small circles represent bare interactions, lines with arrows represent bare propagators, bold lines with arrows represent full propagators, and filled circles represent the self-energy.

the second row of Fig. 5.1. Translating the last diagram into the language of the ψ -fields via the substitution (5.9), we find self-consistent Hartree-Fock theory, which we draw in Fig. 5.2. The Fock part contributes only in the symmetry-broken



Figure 5.2: The diagrams of the right-hand side of the self-consistency equation for the self-energy in the language of the ψ -fields

case, yielding anomalous self-energies which lead to the anomalous propagators characteristic for the symmetry-broken phase. In section 5.1.3, we see how these anomalous propagators lead to anomalous effective interactions.

To further our control of the self-energy of the system given by the Hamiltonian (5.1)+(5.2)+(5.3)+(5.4), we study the diagrammatic equations obtained above symbolically. Evaluating the diagrams of Fig. 5.1 while suppressing convergence-generating factors in the notation leads to the gap equation

$$\begin{aligned} \Sigma_{N_1 N_2}(p) = & - \sum_{k; M_1, M_2} [\delta_{N_1 N_2} \delta_{M_1 M_2} M_2 N_1 U_0(\mathbf{pk}) \\ & + V_0(\mathbf{pk})(\delta_{N_1 -} \delta_{M_2 +} \delta_{N_2 +} \delta_{M_1 -} + \delta_{N_1 +} \delta_{M_2 -} \delta_{N_2 -} \delta_{M_1 +})] \mathbb{G}_{M_1 M_2}(k), \end{aligned}$$

where volume and temperature factors are absorbed into the summation symbol \sum as we continue to do in the following. The sign stems from the fermion loop. Note that for the one-particle Green's function as well as the self-energy, the first index refers to an outgoing line, while the second refers to an ingoing line. Explicitly distinguishing the case off-diagonal in Nambu space from the case diagonal in Nambu space and inserting convergence-generating factors where necessary, we obtain two distinct equations,

$$\begin{aligned} \Sigma_{\pm\pm}(p) &= \mp \sum_k U_0(\mathbf{pk}) \left[\mathbb{G}_{++}(k) e^{i\omega_n 0^+} - \mathbb{G}_{--}(k) e^{i\omega_n 0^-} \right], \\ \Sigma_{\pm\mp}(p) &= - \sum_k V_0(\mathbf{pk}) \mathbb{G}_{\pm\mp}(k). \end{aligned}$$

Writing $\Delta(p) := -\Delta_{\text{ext}}(\mathbf{p}) - \Sigma_{+-}(p)$, $\Sigma(p) := \Sigma_{++}(p)$, and

$$E(k) := \sqrt{(\xi_{\mathbf{k}} + \Sigma(k))^2 + |\Delta(k)|^2},$$

furthermore assuming $\xi_{\mathbf{k}} = \xi_{-\mathbf{k}}$, and using the base $\{(+), (-)\}$ defined in analogy to the cases for two and four Nambu indices, we find

$$\mathbb{G}(k) = \frac{1}{\omega_n^2 + E(k)^2} \begin{pmatrix} -i\omega_n - \xi_{\mathbf{k}} - \Sigma(k) & \Delta(k) \\ \Delta^*(k) & -i\omega_n + \xi_{\mathbf{k}} + \Sigma(k) \end{pmatrix} \quad (5.13)$$

$$=: \begin{pmatrix} G(k) & F(k) \\ F^*(k) & H(k) \end{pmatrix} \quad (5.14)$$

and

$$\Sigma(p) = - \sum_{\mathbf{k}} U_0(\mathbf{k}\mathbf{p}) \frac{e^{i\omega_n 0+}(-i\omega_n - \xi_{\mathbf{k}} - \Sigma(k)) + e^{i\omega_n 0-}(i\omega_n - \xi_{\mathbf{k}} - \Sigma(k))}{\omega_n^2 + E(k)^2}$$

$$\Delta(p) = -\Delta_{\text{ext}}(\mathbf{p}) + \sum_{\mathbf{k}} V_0(\mathbf{p}\mathbf{k}) \frac{\Delta(k)}{\omega_n^2 + E(k)^2}.$$

The self-energies do not depend on Matsubara frequency since V_0 , U_0 , and Δ_{ext} do not depend on Matsubara frequency. The Matsubara sums can therefore be performed analytically according to (B.6), (B.12), and (B.13). The result is

$$\Delta(\mathbf{p}) = -\Delta_{\text{ext}}(\mathbf{p}) + \sum_{\mathbf{k}} V_0(\mathbf{p}\mathbf{k}) \frac{\Delta(\mathbf{k}) \tanh(\beta E_{\mathbf{k}}/2)}{2E_{\mathbf{k}}} \quad (5.15)$$

$$\Sigma(\mathbf{p}) = - \sum_{\mathbf{k}} U_0(\mathbf{p}\mathbf{k}) \left[1 - \frac{\xi_{\mathbf{k}} + \Sigma(\mathbf{k})}{E_{\mathbf{k}}} \tanh(\beta E_{\mathbf{k}}/2) \right]. \quad (5.16)$$

Setting $U_0 = 0$, (5.15) becomes the superconducting gap equation (see Mahan (2000), page 641). Setting $V_0 = 0$, (5.16) turns into

$$\Sigma(\mathbf{p}) = -2 \sum_{\mathbf{k}} U_0(\mathbf{p}\mathbf{k}) f(\xi_{\mathbf{k}} + \Sigma(\mathbf{k})), \quad (5.17)$$

where $f(E)$ is the usual Fermi function. (5.17) is the Hartree self-energy equation appropriate for the interaction term (5.3). This concludes the section on the gap equations, in which an explicit form of the full propagator was found and self-consistency equations determining the superconducting order parameter as well as the normal self-energy were derived.

5.1.3 Bethe-Salpeter equation

In this section, we determine the effective interaction by a resummation similar in fashion to the resummation for the charge-density wave (CDW) presented in Fig. 2.1 of section 2.1.2. We start by determining the structure of the perturbation expansion for the effective interaction and studying the change in the

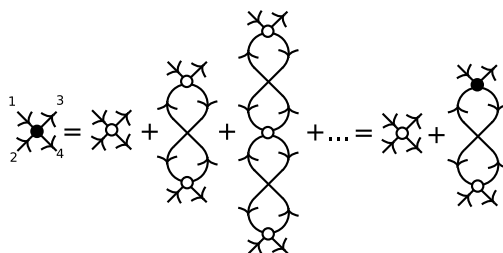


Figure 5.3: Bethe-Salpeter equation for the four-point function. Filled circles represent effective four-point functions, empty circles represent bare four-point functions, lines which have both ends terminating in a vertex represent full propagators, other lines are decorations. Note that the first two indices refer to incoming lines, while the second pair refers to outgoing lines.

diagrammatics caused by the substitution (5.9). In the thermodynamic limit, the perturbation expansion for the effective interaction includes only bubble diagrams which can be resummed into a Bethe-Salpeter equation as shown in figure 5.3. This is due to an argument which is analogous to the arguments presented for the CDW in section 2.1.2 and for the superconducting gap equation in section 5.1.2. The contributions from all other diagrams, notably particle-particle diagrams in ϕ -fields, vanish. Translating the diagrams into the language of the ψ -fields via the substitution (5.9), we find that we are resumming diagrams of the type exemplified in figure 5.4. Our calculation includes chains of bubbles (first example), ladders



Figure 5.4: Examples of the ψ -field diagrams resummed by the ϕ -field Bethe-Salpeter equation

(second example), and connecting parts (third example), forming diagrams such as the fourth example. Adding arrows to the connecting part as in Fig. 5.5, we find effective interactions with an uneven number of incoming arrows in the symmetry-broken phase. These are taken into account automatically in the Bethe-Salpeter

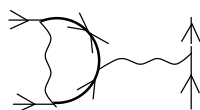


Figure 5.5: Symmetry-broken phase diagram in ψ -field language generating an effective interaction with three incoming arrows

equation in the ϕ -formalism.

Referring to the enlarged version Fig. 5.6 of the loop diagram from Fig. 5.3,

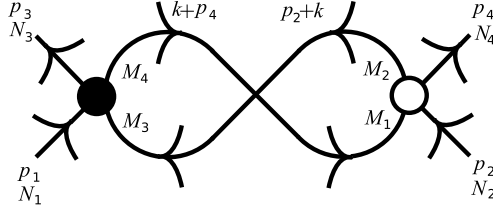


Figure 5.6: Blow-up of the bubble diagram from the right-hand side of the equation in Fig. 5.3.

we can write down the Bethe-Salpeter equation symbolically:

$$\begin{aligned} \mathbb{V}_{\mathbf{N}}(p_1 \dots p_4) = & \mathbb{V}_0 \mathbf{N}(p_1 \dots p_4) - \\ & \sum_{k, \mathbf{M}} \mathbb{V}_{N_1 M_3 N_3 M_4}(p_1, p_2 + k, p_3, p_4 + k) \mathbb{G}_{M_3 M_2}(p_2 + k) \times \\ & \mathbb{G}_{M_1 M_4}(p_4 + k) \mathbb{V}_0 \mathbf{M}_1 N_2 M_2 N_4(p_4 + k, p_2, p_2 + k, p_4), \end{aligned} \quad (5.18)$$

where the momentum conservation of \mathbb{V}_0 is used to simplify the expression. Since propagators are momentum and energy conserving, the full four-point function has the same momentum and energy structure as the bare four-point function. However, the Nambu structure can be different, since propagators do not necessarily conserve the Nambu index. This is how effective interactions with an odd number of incoming arrows are generated in the ϕ -formalism. We neglect the second matrix from (5.12) to calculate the $\delta_{\mathbf{p}_1 \mathbf{p}_3}$ part of \mathbb{V} and denote the Nambu indices in pairs to make the matrix structure as in Fig. 5.7 visible, obtaining

$$\begin{aligned} \mathbb{V}_{N_1 N_3, N_2 N_4}(\mathbf{p}_1 \mathbf{p}_2) = & \mathbb{V}_0 \mathbf{N}_1 N_3, N_2 N_4(\mathbf{p}_1 \mathbf{p}_2) - \\ & \sum_{q, \mathbf{M}} \mathbb{V}_0 \mathbf{M}_1 M_2, N_2 N_4(\mathbf{k} \mathbf{p}_2) \mathbb{G}_{M_1 M_4}(k) \mathbb{G}_{M_3 M_2}(k) \mathbb{V}_{N_1 N_3, M_3 M_4}(\mathbf{p}_1 \mathbf{k}) \\ \stackrel{\text{def}}{=} & \sum_{k, \mathbf{M}} \mathbb{V}_0 \mathbf{M}_1 M_2, N_2 N_4(\mathbf{k} \mathbf{p}_2) \mathbb{L}_{M_3 M_4, M_1 M_2}(k) \mathbb{V}_{N_1 N_3, M_3 M_4}(\mathbf{p}_1 \mathbf{k}). \end{aligned} \quad (5.19)$$

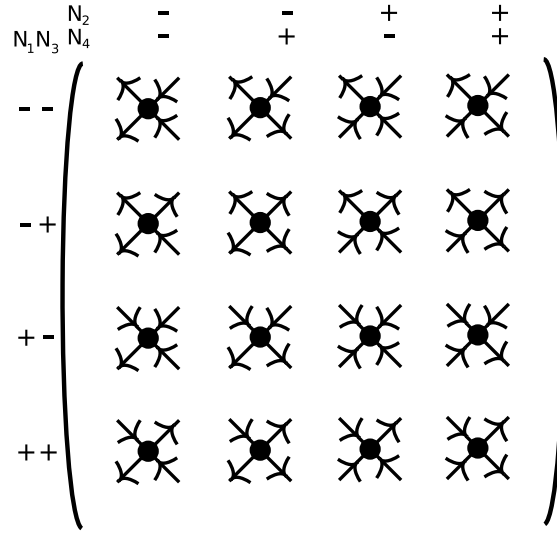
(5.19) becomes

$$\mathbb{V}(\mathbf{p}_1 \mathbf{p}_2) = \mathbb{V}_0(\mathbf{p}_1 \mathbf{p}_2) - \sum_k \mathbb{V}(\mathbf{p}_1 \mathbf{k}) \mathbb{L}(k) \mathbb{V}_0(\mathbf{k} \mathbf{p}_2). \quad (5.20)$$

This determines the effective interaction implicitly. The explicit evaluation is the topic of the sections below.

5.1.4 Redundancies of \mathbb{V}

In this section, the redundancies of \mathbb{V} are analyzed to facilitate its explicit determination below. To carry out the analysis, we study (5.20) component-wise. To

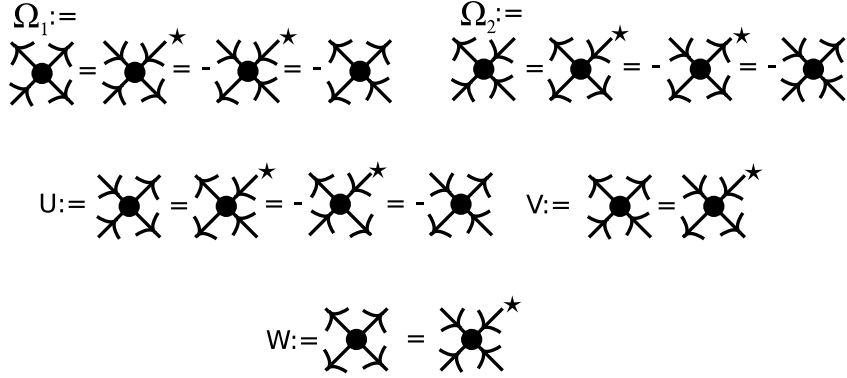

 Figure 5.7: A diagram for every entry of \mathbb{V} .

this end, we consider the entries of $\mathbb{V}(\mathbf{k}_1 \mathbf{k}_2)$ diagrammatically. Their diagrammatic representations are defined in Fig. 5.7. A detailed study of $\mathbb{L}\mathbb{V}_0$ from (5.20) is expedient to further our understanding of the Bethe-Salpeter equation. Neglecting momentum/energy parameters for brevity and using $H^2 = G^{*2}$, we find

$$\begin{aligned}
 \mathbb{L}\mathbb{V}_0 &= \begin{pmatrix} G^{*2} & HF^* & FH & FF^* \\ F^*H & F^{*2} & GH & GF^* \\ HF & HG & F^2 & FG \\ F^*F & F^*G & GF & G^2 \end{pmatrix} \mathbb{V}_0 \\
 &= \begin{pmatrix} -U_0(FF^* - G^{*2}) & V_0FH & V_0F^*H & -U_0(G^{*2} - FF^*) \\ -U_0F^*(G - H) & V_0GH & V_0F^{*2} & -U_0F^*(H - G) \\ -U_0F(G - H) & V_0F^2 & V_0GH & -U_0F(H - G) \\ -U_0(G^2 - F^*F) & V_0FG & V_0F^*G & -U_0(FF^* - G^2) \end{pmatrix}. \quad (5.21)
 \end{aligned}$$

From (5.13), we find $(G - H) \in \mathbb{R}$ and $GH \in \mathbb{R}$ for $\Sigma \in \mathbb{R}$. With this, we see by multiplying the matrix from Fig. 5.7 with (5.21) and studying (5.20) component-wise that the relations from Fig. 5.8 hold. The first matrix from (5.12), constituting the part of the bare interaction relevant for this calculation, also fulfills the relations from Fig. 5.8. With the shorthands introduced in Fig. 5.8, the effective interaction matrix thus simplifies to

$$\mathbb{V} = \begin{pmatrix} U^* & \Omega_2^* & \Omega_2 & -U \\ -\Omega_1 & W^* & V & \Omega_1 \\ -\Omega_1^* & V^* & W & \Omega_1^* \\ -U^* & -\Omega_2^* & -\Omega_2 & U \end{pmatrix}, \quad (5.22)$$


 Figure 5.8: Relations between the components of \mathbb{V}

where parameter-free notation is used for brevity. To remove as many redundancies as possible while preserving the structure of (5.20), we introduce

$$\mathbb{V}^{\text{new}} := \begin{pmatrix} U & \Omega_2 & \Omega_2^* \\ -\Omega_1 & V & W^* \\ -\Omega_1^* & W & V \end{pmatrix}, \quad (5.23)$$

$$\mathbb{L}^{\text{new}} \mathbb{V}_0^{\text{new}} := \begin{pmatrix} G^2 + G^{*2} - 2FF^* & F^*(H - G) & F(H - G) \\ F(H - G) & HG & F^2 \\ F^*(H - G) & F^{*2} & HG \end{pmatrix} \begin{pmatrix} U_0 & 0 & 0 \\ 0 & V_0 & 0 \\ 0 & 0 & V_0 \end{pmatrix} \quad (5.24)$$

$$= \begin{pmatrix} U_0(G^2 + G^{*2} - FF^*) & V_0F^*(H - G) & V_0F(H - G) \\ U_0F(H - G) & V_0HG & V_0F^2 \\ U_0F^*(H - G) & V_0F^{*2} & V_0HG \end{pmatrix}. \quad (5.25)$$

Multiplying (5.23) by (5.25), we obtain the same equations as by multiplying (5.22) by (5.21). This means that the matrix equation

$$\mathbb{V}^{\text{new}}(\mathbf{p}_1\mathbf{p}_2) = \mathbb{V}_0^{\text{new}}(\mathbf{p}_1\mathbf{p}_2) - \sum_k \mathbb{V}^{\text{new}}(\mathbf{p}_1\mathbf{k})\mathbb{L}^{\text{new}}(k)\mathbb{V}_0^{\text{new}}(\mathbf{k}\mathbf{p}_2) \quad (5.26)$$

is equivalent to (5.20). In conclusion, the redundancies of \mathbb{V} allow us to reduce the 16 scalar equations of (5.20) to the nine scalar equations of (5.26).

5.1.5 Momentum-independent scattering

It is possible to solve (5.26) explicitly if we assume that the bare interactions $U_0(\mathbf{p}_1\mathbf{p}_2)$ and $V_0(\mathbf{p}_1\mathbf{p}_2)$ lack momentum-dependence. In this case, (5.26) becomes

$$\mathbb{V}^{\text{new}} = \mathbb{V}_0^{\text{new}} - \mathbb{V}^{\text{new}} \sum_k \mathbb{L}^{\text{new}}(k)\mathbb{V}_0^{\text{new}} \stackrel{\text{def}}{=} \mathbb{V}_0^{\text{new}} - \mathbb{V}^{\text{new}} \mathbb{L}_{\Sigma}^{\text{new}} \mathbb{V}_0^{\text{new}} \quad (5.27)$$

$$\Rightarrow \mathbb{V}^{\text{new}} = \mathbb{V}_0^{\text{new}} (1 + \mathbb{L}_{\Sigma}^{\text{new}} \mathbb{V}_0^{\text{new}})^{-1} = (\mathbb{V}_0^{\text{new}^{-1}} + \mathbb{L}_{\Sigma}^{\text{new}})^{-1} \quad (5.28)$$

We learn from (5.24) that, in components, the inverse of the RHS of (5.28) reads

$$\begin{pmatrix} G^2 + G^{*2} - 2FF^* + (U_0)^{-1} & F^*(H - G) & F(H - G) \\ F(H - G) & HG + V_0^{-1} & F^2 \\ F^*(H - G) & F^{*2} & HG + V_0^{-1} \end{pmatrix}, \quad (5.29)$$

where, for each pair of propagators, summation over all possible values of their omitted momentum and energy arguments is implicit. We choose the following abbreviations for clarity:

$$\begin{aligned} K &:= F(H - G), \\ L/V_0 &:= HG + V_0^{-1}, \\ M/U_0 &:= G^2 + G^{*2} - 2FF^* + (U_0)^{-1}. \end{aligned}$$

(5.29) then reads

$$\begin{pmatrix} M/U_0 & K^* & K \\ K & L/V_0 & F^2 \\ K^* & F^{*2} & L/V_0 \end{pmatrix}. \quad (5.30)$$

L/V_0 and M/U_0 are not optimal as abbreviations; however, this notation keeps the bare couplings in plain sight and makes it easier to study special cases later on. In order to invert (5.29), we calculate the cofactor matrix:

$$\begin{pmatrix} (L/V_0)^2 - F^{*2}F^2 & -(KL/V_0 - K^*F^2) & KF^{*2} - K^*L/V_0 \\ -(K^*L/V_0 - F^{*2}K) & ML/U_0V_0 - KK^* & -(F^{*2}M/U_0 - K^{*2}) \\ K^*F^2 - KL/V_0 & -(F^2M/U_0 - K^2) & ML/U_0V_0 - KK^* \end{pmatrix}, \quad (5.31)$$

which is the transpose of the adjugate matrix $\text{adj}(5.29)$. We note from (5.15) that $\Delta(\mathbf{p})$ is independent of momentum if $V_0(\mathbf{p}_1\mathbf{p}_2)$ is; and that therefore, $F^2F^{*2} = |F^2|^2$ and $K^*F = KF^*$ in this section. Reading off

$$\begin{aligned} &\det(\mathbb{V}^{-1}) \\ &= ((L/V_0)^2 - |F^2|^2)M/U_0 - K(K^*L/V_0 - F^{*2}K) + K^*(K^*F^2 - KL/V_0) \\ &= (L/V_0 - |F^2|)(L/V_0 + |F^2|)M/U_0 - 2|K|^2(L/V_0 - |F^2|) \\ &= (L/V_0 - |F^2|) [(L/V_0 + |F^2|)M/U_0 - 2|K|^2] \end{aligned} \quad (5.32)$$

from (5.30) and (5.31), we identify the Goldstone boson's divergence-creating influence by writing out the first factor of (5.32):

$$\begin{aligned} L/V_0 - |F^2| &= GH + V_0^{-1} - |F^2| \\ &= V_0^{-1} - \sum_q \frac{1}{\omega_n^2 + E_{\mathbf{q}}^2} \\ &= -\frac{\Delta_{\text{ext}}}{V_0\Delta}. \end{aligned} \quad (5.33)$$

See the definition of the matrix Green's function (5.13) and (5.14) for the second and the gap equation (5.15) for the second step.

We conclude the inversion of (5.29) by combining the adjugate matrix (see (5.31) and following text), the determinant (5.32), and the relation (5.33) through the matrix inversion formula

$$\mathbb{A}^{-1} = \frac{1}{\det \mathbb{A}} \text{adj}(\mathbb{A})$$

to obtain:

$$\begin{aligned} U &= \frac{L/V_0 + |F^2|}{(L/V_0 + |F^2|)M/U_0 - 2|K|^2} = U_0 \frac{L + V_0|F^2|}{(L + V_0|F^2|)M - 2U_0V_0|K|^2} \\ \Omega_1 &= \frac{K}{(L/V_0 + |F^2|)M/U_0 - 2|K|^2} = U_0V_0 \frac{K}{(L + V_0|F^2|)M - 2U_0V_0|K|^2} \\ \Omega_2 &= \frac{-K^*}{(L/V_0 + |F^2|)M/U_0 - 2|K|^2} = U_0V_0 \frac{-K^*}{(L + V_0|F^2|)M - 2U_0V_0|K|^2} \\ V &= \frac{-\Delta(ML/U_0 - V_0KK^*)}{\Delta_{\text{ext}} [(L/V_0 + |F^2|)M/U_0 - 2|K|^2]} = V_0 \frac{\Delta}{\Delta_{\text{ext}}} \frac{U_0V_0|K|^2 - ML}{(L + V_0|F^2|)M - 2U_0V_0|K|^2} \\ W &= \frac{V_0\Delta(F^{*2}M/U_0 - K^{*2})}{\Delta_{\text{ext}} [(L/V_0 + |F^2|)M/U_0 - 2|K|^2]} = V_0^2 \frac{\Delta}{\Delta_{\text{ext}}} \frac{F^{*2}M - U_0K^{*2}}{(L + V_0|F^2|)M - 2U_0V_0|K|^2} \end{aligned}$$

We realize that Ω_1 and Ω_2 are finite in the symmetry-broken phase because their numerators remain finite. This prevents us from neglecting them in further calculations. Setting $U_0 = 0$, U , Ω_1 , and Ω_2 vanish as expected, while the expressions for V and W turn into the usual random-phase approximation expressions for the normal and anomalous effective Cooper interaction. This concludes the study of the model combining Cooper with forward scattering defined by (5.1)+(5.2)+(5.3)+(5.4).

5.2 Resummation approach to the attractive Hubbard model

5.2.1 Hamiltonian

In this section, we study the attractive Hubbard model in two dimensions employing the approach developed in sections 5.1.1-5.1.3 as an approximation. formalism and method developed in the preceding section 5.1 for a system incorporating Cooper and forward scattering. Our goals are to study the Nambu structure of the effective interaction, to numerically gauge the impact of the effective interactions with an odd number of incoming legs, and to study the momentum and energy dependence of the effective interaction, analyzing collective modes in the process. The Hubbard Hamiltonian reads

$$H = \sum_{\mathbf{k}s} \xi_{\mathbf{k}} c_{\mathbf{k}s}^\dagger c_{\mathbf{k}s} - \frac{U_0}{N} \sum_{\mathbf{k}_1 \mathbf{k}_2 \mathbf{k}_3} c_{\mathbf{k}_1 \uparrow}^\dagger c_{\mathbf{k}_3 \uparrow} c_{\mathbf{k}_2 \downarrow}^\dagger c_{\mathbf{k}_1 + \mathbf{k}_2 - \mathbf{k}_3 \downarrow}. \quad (5.34)$$

We also add an external singlet-pairing field term

$$\sum_{\mathbf{k}} \left(\Delta_{\text{ext}}(\mathbf{k}) c_{-\mathbf{k}\downarrow}^\dagger c_{\mathbf{k}\uparrow}^\dagger + \Delta_{\text{ext}}^*(\mathbf{k}) c_{\mathbf{k}\uparrow} c_{-\mathbf{k}\downarrow} \right), \quad (5.35)$$

which is sent to zero after the calculations. The tight-binding dispersion relation

$$\xi_{\mathbf{k}} = -2t(\cos k_x + \cos k_y) - 4t' \cos k_x \cos k_y - \mu \quad (5.36)$$

includes hopping between nearest neighbors with amplitude t and hopping between next-nearest neighbors with amplitude t' . We pass to a functional integral representation (cf. (5.5)-(5.8)) and employ the substitution (5.9) to obtain

$$S = \sum_k (\bar{\phi}_{k+} \quad \bar{\phi}_{k-}) \begin{pmatrix} i\omega_n - \xi_{\mathbf{k}} & -\Delta_{\text{ext}}^*(\mathbf{k}) \\ -\Delta_{\text{ext}}(\mathbf{k}) & i\omega_n + \xi_{\mathbf{k}} \end{pmatrix} \begin{pmatrix} \phi_{k+} \\ \phi_{k-} \end{pmatrix} + U_0 \sum_{k_1 k_2 k_3} \bar{\phi}_{k_1+} \bar{\phi}_{k_3-k_1-k_2,-} \phi_{k_3+} \phi_{-k_2-}, \quad (5.37)$$

where $k = (i\omega_n, \mathbf{k})$ and volume as well as temperature factors are implicitly contained in the summation symbol \sum , a practice we also apply in the following. Antisymmetrizing the interaction part yields

$$U_0 \sum_{1\dots 4} \delta_{k_1+k_2, k_3+k_4} \underbrace{(\delta_{N_1+} \delta_{N_2-} - \delta_{N_2+} \delta_{N_1-}) (\delta_{N_3+} \delta_{N_4-} - \delta_{N_4+} \delta_{N_3-})}_{(++)(-)-(-+)(-+)-(-+)(-+)+(--)(++)} \bar{\phi}_1 \bar{\phi}_2 \phi_3 \phi_4, \quad (5.38)$$

where i , if used as an index, is short for $(k_i N_i)$, and we have exchanged 2 and 4 in comparison with (5.37). As a matrix according to the Nambu base from figure 5.7, the antisymmetrized bare interaction reads

$$U_0 \begin{pmatrix} 0 & 0 & 0 & 1 \\ 0 & 0 & -1 & 0 \\ 0 & -1 & 0 & 0 \\ 1 & 0 & 0 & 0 \end{pmatrix} \delta_{k_1+k_2, k_3+k_4}. \quad (5.39)$$

5.2.2 Resummation approach

We employ the gap equation (5.15) as an approximation for the true superconducting gap equation in the following. The diagonal self energy is absorbed in the chemical potential, $\mu \rightarrow \mu - \Sigma$. We employ the Bethe-Salpeter equation from Fig. 5.3 as it treats superconductivity and forward scattering, which are the most important scattering processes at low temperatures (Metzner et al. (1998)). The blow-up from Fig. 5.6 is shown for the Hubbard model in Fig. 5.9. Evaluating the

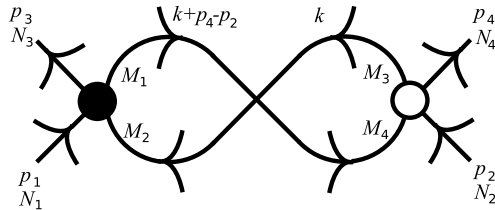


Figure 5.9: The loop diagram from figure 5.6 for the Hubbard model

diagrams yields the symbolic Bethe-Salpeter equation

$$\mathbb{U}(1234) = \mathbb{U}_0(1234) - \sum_{\substack{q \\ N'_1 \dots M_4}} \mathbb{U}_{N_1 M_2 N_3 M_1}(p_1, k, p_3) \times \quad (5.40)$$

$$\mathbb{U}_{0 M_4 N_2 M_3 N_4}(k + p_4 - p_2, p_2, k) \mathbb{G}_{M_1 M_4}(k + p_4 - p_2) \mathbb{G}_{M_3 M_2}(k),$$

where as a parameter, $i = 1 \dots 4$ is short for $p_i N_i$. Through the introduction of the loop matrix

$$\mathbb{L}_{M_2 M_1, M_4 M_3}(k, p) := \mathbb{G}_{M_1 M_4}(k + p) \mathbb{G}_{M_3 M_2}(k) \quad (5.41)$$

and by exploiting momentum and energy conservation $p_1 + p_2 = p_3 + p_4$ while setting $p := p_1 - p_3$, (5.40) can be rewritten as

$$\mathbb{U}(p_1 \dots p_4) = \mathbb{U}_0 - \sum_q \mathbb{U}(p_1, k, p_3, k + p) \mathbb{L}(k, p) \mathbb{U}_0, \quad (5.42)$$

where the Nambu indices of \mathbb{U} and \mathbb{U}_0 are organized into pairs as in Fig. 5.7. $\mathbb{U}(p_1 \dots p_4)$ only depends on p in this approximation, as can be seen by solving for \mathbb{U} . Finally, we obtain

$$\mathbb{U}(p) = \left(\mathbb{U}_0^{-1} + \sum_q \mathbb{L}(k, p) \right)^{-1}. \quad (5.43)$$

Using the symbols from (5.13),

$$\mathbb{L} = \begin{pmatrix} HH & HF^* & FH & FF^* \\ F^*H & F^*F^* & GH & GF^* \\ HF & HG & FF & FG \\ F^*F & F^*G & GF & GG \end{pmatrix}, \quad (5.44)$$

where for each matrix entry it is understood that $k + p$ is plugged into the first and k into the second factor, implying that the order of the two propagators is fixed in this case. Furthermore, a star in (5.44) implies that the complex conjugate be taken, but only of the gap amplitude in the numerator of the corresponding propagator.

5.2.3 No Nambu rank reduction

A simplification as given by the relations in figure 5.8 is not possible in the Hubbard model case. This is because the order of the propagators in the entries of \mathbb{L} cannot be reversed due to their differing arguments and because \mathbb{U}_0 is nonzero only on the counter-diagonal. We study this fact in more detail in the following.

We first show which simplifications still apply. Writing

$$\mathbb{U} = \begin{pmatrix} X^* & \Omega_3 & \Omega_2 & U \\ -\Omega_4^* & W^* & V & \Omega_1 \\ -\Omega_1^* & V^* & W & \Omega_4 \\ U^* & -\Omega_2^* & -\Omega_3^* & X \end{pmatrix}, \quad (5.45)$$

we see that our labels are consistent with (5.42) by proceeding as in section 5.1.4. The stars in (5.45) only imply to take the complex conjugate of the gap amplitude.

For (5.42) to reduce to an equation for 3×3 matrices, there can only be three distinct entries in each line of \mathbb{U} : at least one entry must be expressible through one of the others under sign reversal or complex conjugation. We consider the first line of \mathbb{U} . The inequality sign \neq in the following means inequality even if overall signs and imaginary-part signs are disregarded. Plugging $\mathbb{U}(k_1 \dots k_4) = \mathbb{U}(k_1 - k_3)$ as well as the loop matrix (5.44) into the resummation equation (5.42), we find that $X^* \neq \Omega_3 \neq U \neq \Omega_2$ and $X^* \neq \Omega_2 \neq U \neq \Omega_3$. $U \neq X$ follows from the presence of a U_0 -term – due to the counter-diagonal structure of the bare interaction (5.39) – in the equation for U but not in the equation for X . $\Omega_2 \neq \Omega_3$ is due to $GH \neq HG$, that is the non-commutativity of the propagator products in (5.44). We have thus shown that the first line of \mathbb{U} cannot be simplified because of the Nambu structure of \mathbb{U}_0 and the fixed order of the propagators in \mathbb{L} , substantiating our claim from this section's first paragraph.

5.2.4 Numerical setup

To obtain a deeper understanding of the structure of the effective interaction, we solve (5.43) numerically in the following. The Matsubara sums in (5.43) can be performed analytically. This operation proceeds similarly for all components of \mathbb{L} , as the poles are the same in all cases. These poles are determined by the denominator

$$D := [(\omega_n + \nu_m)^2 + E_{\mathbf{k}+\mathbf{p}}^2] (\omega_n^2 + E_{\mathbf{k}}^2)$$

of the products of Green's functions (5.13) in the loop matrix \mathbb{L} , where the summation is over ω_n and \mathbf{k} . Note that ν_m , as a difference between two fermionic Matsubara frequencies, is a bosonic Matsubara frequency, $\nu_m \in 2\pi T\mathbb{Z}$. The denominator D can be factorized into

$$D = [i(\omega_n + \nu_m) + E_{\mathbf{p}+\mathbf{k}}] [i(\omega_n + \nu_m) - E_{\mathbf{p}+\mathbf{k}}] [i\omega_n + E_{\mathbf{k}}] [i\omega_n - E_{\mathbf{k}}].$$

By the residue theorem, we obtain

$$\begin{aligned} T \sum_{\omega_n} \frac{g(i\omega_n)}{D} &= \frac{f(-i\nu_m - E_{\mathbf{p}+\mathbf{k}})g(-i\nu_m - E_{\mathbf{p}+\mathbf{k}})}{-2E_{\mathbf{p}+\mathbf{k}}(-i\nu_m - E_{\mathbf{p}+\mathbf{k}} + E_{\mathbf{k}})(-i\nu_m - E_{\mathbf{k}} - E_{\mathbf{p}+\mathbf{k}})} \\ &+ \frac{f(-i\nu_m + E_{\mathbf{p}+\mathbf{k}})g(-i\nu_m + E_{\mathbf{p}+\mathbf{k}})}{2E_{\mathbf{p}+\mathbf{k}}(-i\nu_m + E_{\mathbf{p}+\mathbf{k}} + E_{\mathbf{k}})(-i\nu_m + E_{\mathbf{p}+\mathbf{k}} - E_{\mathbf{k}})} \\ &+ \frac{f(-E_{\mathbf{q}})g(-E_{\mathbf{q}})}{-2E_{\mathbf{k}}(i\nu_m + E_{\mathbf{p}+\mathbf{k}} - E_{\mathbf{k}})(i\nu_m - E_{\mathbf{p}+\mathbf{k}} - E_{\mathbf{k}})} \\ &+ \frac{f(E_{\mathbf{q}})g(E_{\mathbf{q}})}{2E_{\mathbf{k}}(i\nu_m + E_{\mathbf{p}+\mathbf{k}} + E_{\mathbf{k}})(i\nu_m - E_{\mathbf{p}+\mathbf{k}} + E_{\mathbf{k}})}, \end{aligned} \quad (5.46)$$

where $f(x) = (\exp(x/T) + 1)^{-1}$ is the Fermi distribution and $g(x)$ is any smooth function of order smaller than x^3 for large x . Explicit expressions for the individual

bubbles are listed in appendix C. The remaining integration over the Brillouin zone and the matrix inversion on the right-hand side of (5.43) are performed numerically. In the following, a system with $t' = t/6$, $\mu = -1.5t$, $U_0 = 2t$, $\Delta_{\text{ext}} = 10^{-4}t$, and $T = 0.035t$ is assumed. This choice of parameters corresponds to an approximately quarter-filled system far below its mean-field critical temperature. We employ an external field $\Delta_{\text{ext}} = 10^{-4}t$. This keeps the numerics well-behaved having no appreciable influence away from $\mathbf{p} = 0$.

5.2.5 Numerical results: momentum space

We commence by discussing the numerical results for the static part, $\nu = 0$. To provide an overview, we plot in Fig. 5.10 and 5.11 the normal part V and the

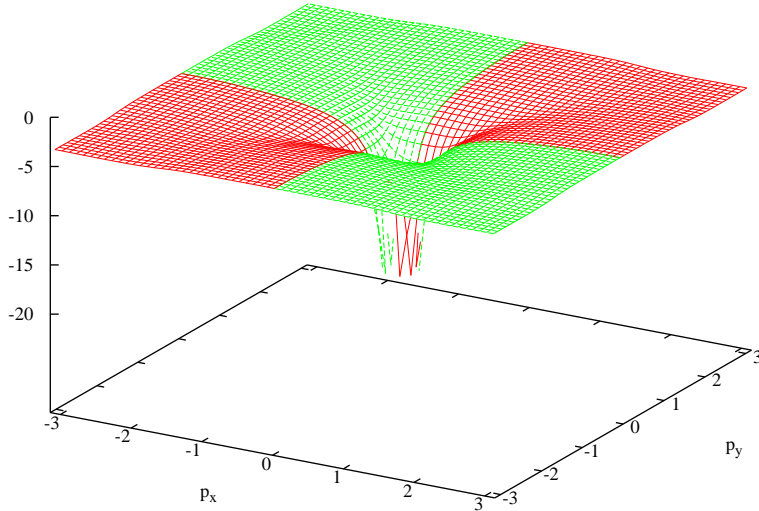


Figure 5.10: Momentum-dependence of the static part of the normal Cooper-channel effective interaction V in units of t

anomalous part W of the Cooper channel effective interaction (see (5.45)). We are particularly interested in the impact of the Ω_i on the effective interactions. To gauge this impact, we study the difference between V calculated by fully solving (5.43) and V calculated by setting all loops combining normal and anomalous propagators to zero. This is equivalent to setting the Ω_i to zero, because besides generating the Ω_i , these loops are only involved in the feedback of the Ω_i onto the other effective interactions. We abbreviate by $V_{\text{with } \Omega}$ the normal Cooper-channel effective interaction if the Ω_i are taken into account, and by $V_{\text{w/o } \Omega}$ otherwise. A plot of the difference relative to $V_{\text{w/o } \Omega}$ is shown in Fig. 5.12. The change induced by including the Ω_i is smaller than 5% in magnitude and restricted to large and very small momenta. Only about a quarter of the available phase space shows an appreciable change in the magnitude of V . For very small momenta, the inclusion of the Ω_i suppresses V in magnitude, but only by 2%. Studying the large-momentum part of $V_{\text{with } \Omega}$ and $V_{\text{w/o } \Omega}$ plotted in Fig. 5.13 reveals that the inclusion of the Ω_i actually enhances the magnitude of the normal Cooper channel effective interaction

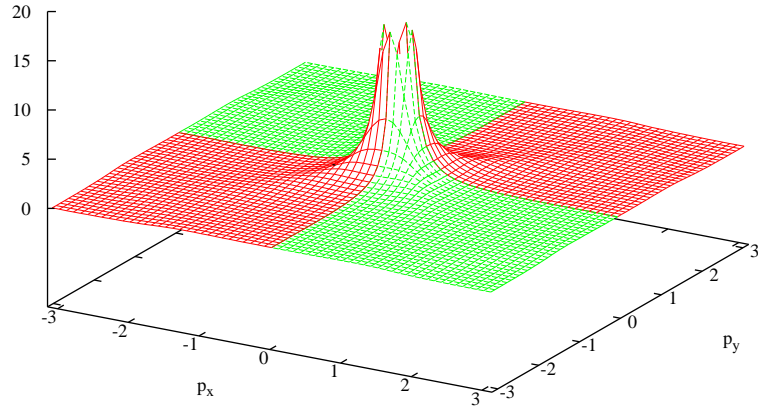


Figure 5.11: Momentum-dependence of the static part of the anomalous Cooper-channel effective interaction W in units of t

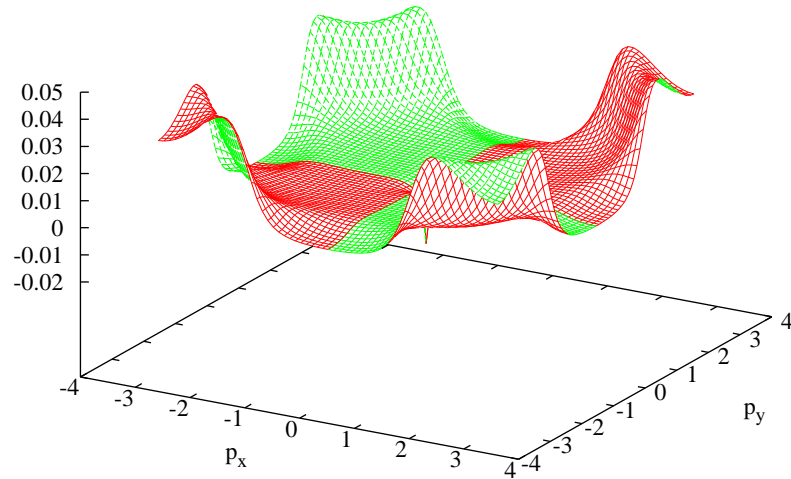


Figure 5.12: Change of the normal Cooper channel effective interaction through the inclusion of the Ω_i , $(V_{w/o \Omega} - V_{with \Omega})/V_{w/o \Omega}$

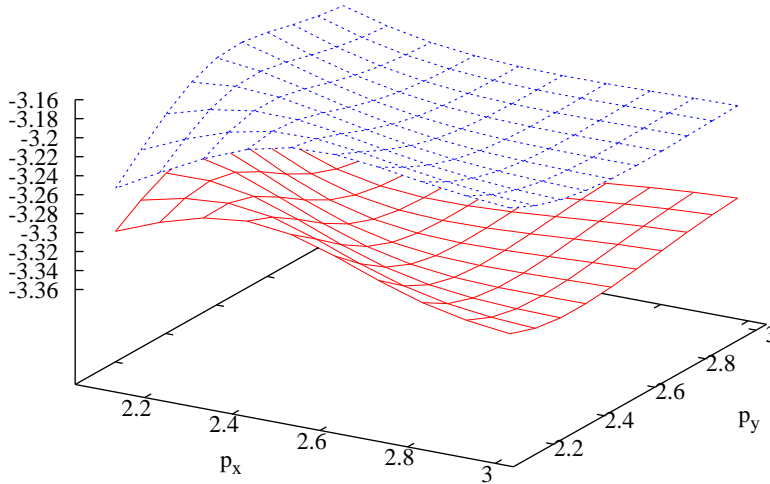


Figure 5.13: Normal Cooper-channel effective interaction V with (lower) and without (upper) the Ω_i .

for large momenta.

We examine the change in the anomalous Cooper channel effective interaction, W , attaching labels as above. This is plotted in Fig. 5.14. W is strongly suppressed

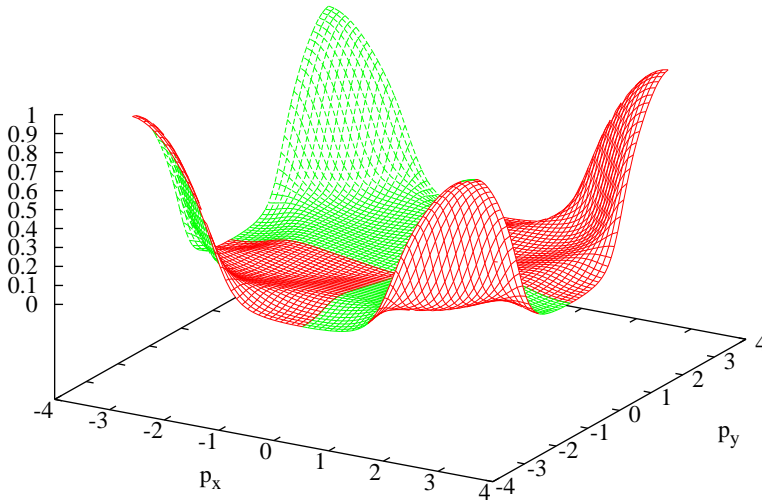


Figure 5.14: Change of the anomalous Cooper channel effective interaction through the inclusion of the Ω_i , $(W_{w/o \Omega} - W_{with \Omega})/W_{w/o \Omega}$

by the inclusion of the Ω_i , especially for large momenta along the Brillouin zone diagonal, while the suppression for very small momenta is only about 2%, as for V . Along the crystal axes, W changes by up to 10%. The large change along the Brillouin zone diagonal is due to the almost complete suppression of the large-momentum W along the diagonal by the introduction of the Ω_i . This suppression is clearly seen in Fig. 5.15. It is notable that while V is enhanced by the Ω_i in certain parts of the Brillouin zone, W is everywhere suppressed or unchanged. It

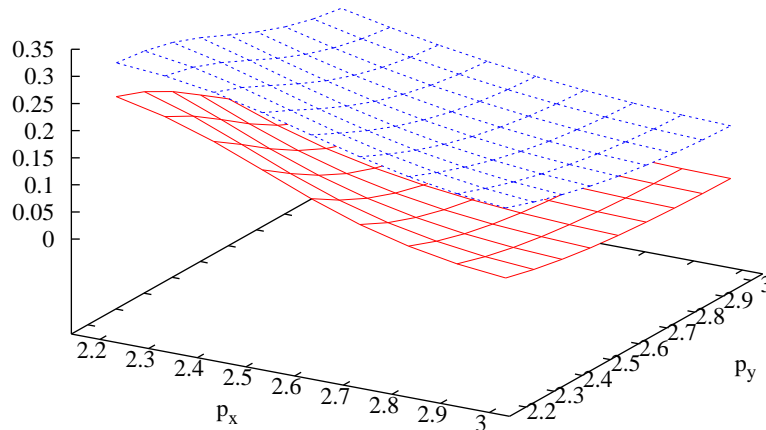


Figure 5.15: Comparison of $W_{\text{with } \Omega}$ (lower) and $W_{\text{w/o } \Omega}$ (upper) for large momenta along the BZ diagonal

is also notable that the absolute value of the suppression of W for large momenta along the diagonal is quite similar to the absolute value of the enhancement of V . This implies a transfer of weight from W to V , that is, from anomalous to normal Cooper channel effective interactions.

Approximative expression To study the collective modes associated with the symmetry-breaking, we examine the small-momentum behavior of the effective interaction. An approximate dispersion of the collective modes can be determined by approximating the effective interaction components as rational functions of energy and momenta. We start by comparing our momentum-space data for V and W to the function

$$\frac{\alpha}{\Delta_{\text{ext}} + \beta |\mathbf{p}|^2} + \gamma, \quad (5.47)$$

with $\alpha, \beta \in \mathbb{R}$ to be determined. Fig. 5.16 shows the comparison for V . Fig. 5.17 does likewise for W , but setting $\alpha = 0.2870$ and $\gamma = 0$. For the small-momentum region displayed, (5.47) is an excellent approximation for V and W . Scrutinizing large momenta (not shown here), it becomes clear that the approximation is much less good, but still acceptable. Overall, (5.47) is a good approximation for both V and W provided that α , β , and γ are chosen correctly. This means that for small $|\mathbf{p}|$, the leading contribution to the denominators of V and W is of second order.

5.2.6 Numerical results: frequency space

To gauge the impact of the inclusion of the Ω_i on the energy-dependence of V and W , we consider the $\mathbf{p} = 0$ part of the vertex. The real and imaginary parts of the normal V and anomalous Cooper vertices W , both for the case with and for the case without Ω_i , are plotted in figure 5.18. As we discern from figure 5.19, the maximum change in the normal Cooper-channel vertex upon inclusion of the Ω_i is almost 30%. This maximum change occurs in the real part for $\nu_m = \pm 2\pi T$. The

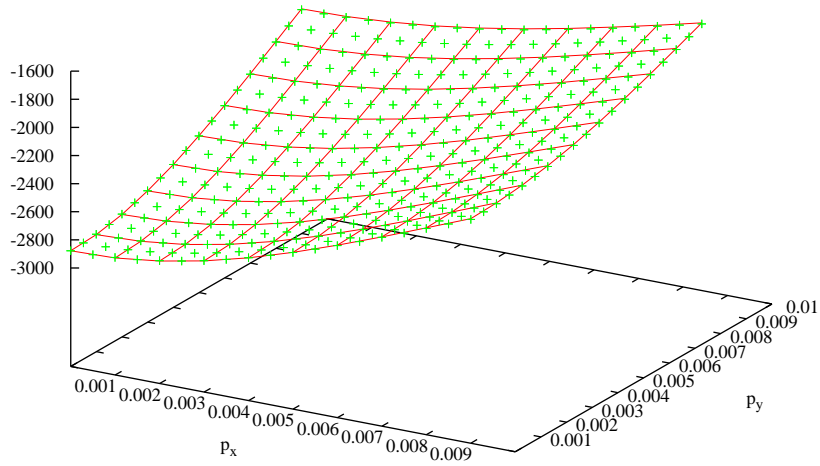


Figure 5.16: V in units of t calculated numerically (red lines) in comparison with the approximation (5.47) using $\alpha = -0.2874t^2$, $\beta = 0.45t$, and $\gamma = -3.294t$ (green crosses).

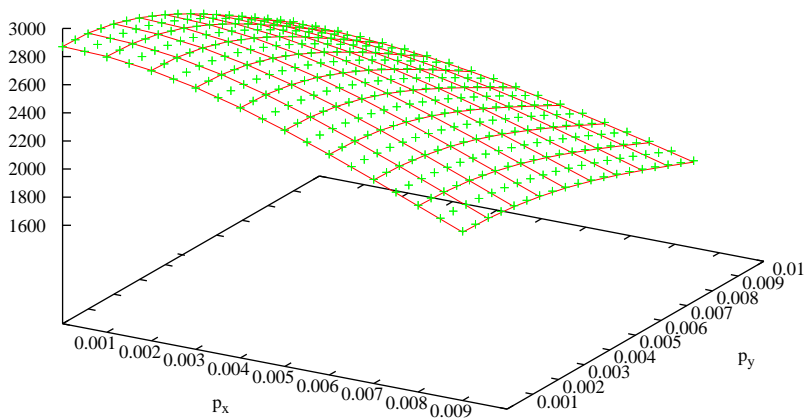


Figure 5.17: W in units of t calculated numerically (red lines) in comparison with the approximation (5.47) using $\alpha = 0.2870t^2$, $\beta = 0.45t$, and $\gamma = 0$ (green crosses).

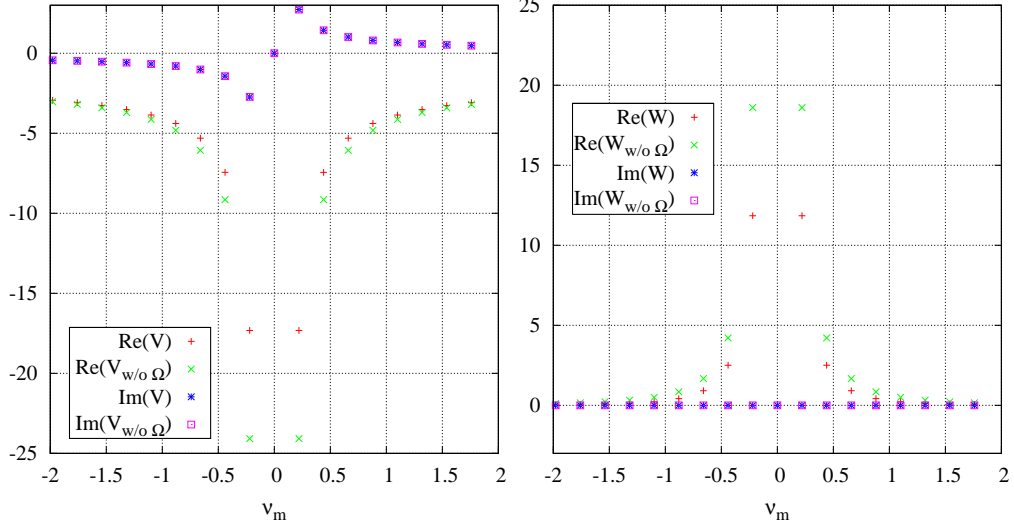


Figure 5.18: Energy dependence of $V = V_{\text{with } \Omega}$ and $V_{\text{w/o } \Omega}$, $W = W_{\text{with } \Omega}$ and $W_{\text{w/o } \Omega}$, all in units of t

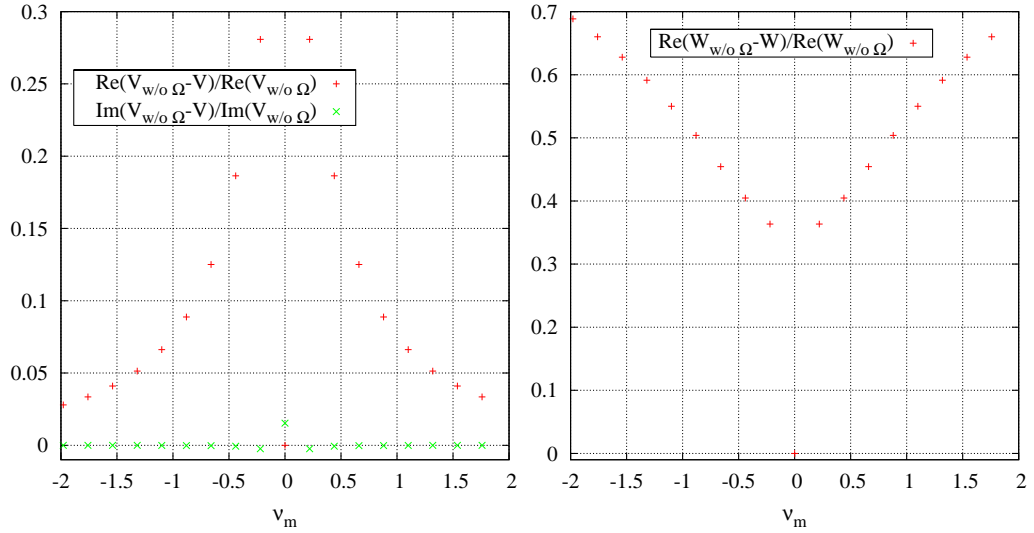


Figure 5.19: The energy-dependent change of the normal and anomalous Cooper-channel vertices upon introduction of the Ω_i , ν_m in units of t

vertex for $\nu_m = 0$ does not change and neither does the imaginary part for any ν_m . (The value at $\nu_m = 0$ in the left-hand graph of figure 5.19 is due to numerical inaccuracy.)

Turning to the right-hand graph, we find that for the imaginary part of the anomalous Cooper channel effective interaction W , the effect of including the Ω_i is negligible: $\text{Im}(W)$ vanishes always. The real part, however, while unchanged for $\nu_m = 0$, is strongly suppressed for ν_m having finite magnitude. This suppression grows with $|\nu_m|$ and attains almost 70% for the largest-magnitude Matsubara frequency considered here. This is due to $\text{Re}(W_{\text{with } \Omega})$ approaching 0 much faster than $\text{Re}(W_{\text{w/o } \Omega})$ for large ν_m . Overall, the effect of the Ω_i on the energy dependence of the normal and anomalous Cooper effective interaction is sizable.

Analytic expressions To complete our study of the Ω_i 's impact on the dispersion relation for the collective modes present in the symmetry-broken state, we search an approximate expression for the energy dependence of V and W . To this end, we extend the expression (5.47) by adding to the denominator:

$$\frac{\alpha}{\Delta_{\text{ext}} + \beta_p |\mathbf{p}|^2 + \beta_\nu \nu_m^2} + \gamma \quad (5.48)$$

Fig. 5.20 shows the result of least-squares fitting (Levenberg (1944); Marquardt (1963)) (5.48) via β_ν to the numerical data for $\text{Re}V$ and W . α was determined

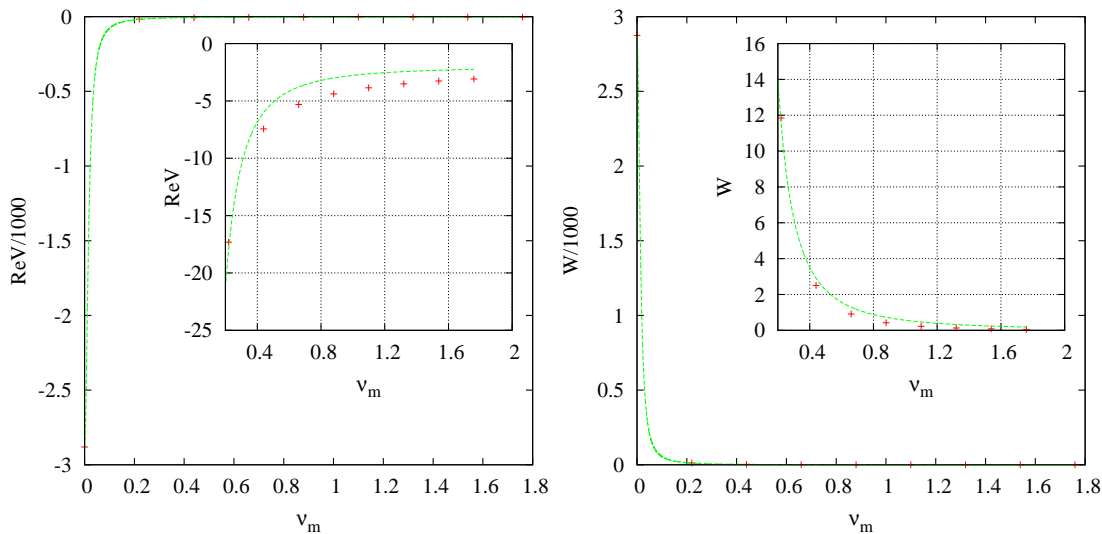


Figure 5.20: Fitting (5.48) to the Matsubara-frequency dependence of $\text{Re}V$ (left) and W (right), everything in units of t . Crosses correspond to numerical results, lines to the fitted functions. $\alpha = -0.2880t$, $\beta_\nu = 0.37t^{-1}$, and $\gamma = -2t$ were used for V , $\alpha = 0.2874t$, $\beta_\nu = 0.51t^{-1}$, and $\gamma = 0$ for W .

from the value at $\nu_m = 0$ of $\text{Re}V$ and W , respectively. γ was manually set to 0 for W and to $-2t$ for V . For small Matsubara frequencies, we obtain a good fit. This implies a linear dispersion relation for the collective modes at small energies, as in the case without the Ω_i , see Popov (1991).

We take the imaginary part of V into account in our approximations by adding to the numerator of (5.48):

$$\frac{\alpha + \epsilon i \nu_m}{\Delta_{\text{ext}} + \beta_p |\mathbf{p}|^2 + \beta_\nu \nu_m^2} + \gamma. \quad (5.49)$$

From Fig. 5.21, we learn that (5.49) fits the data quite well. Numerical calculations

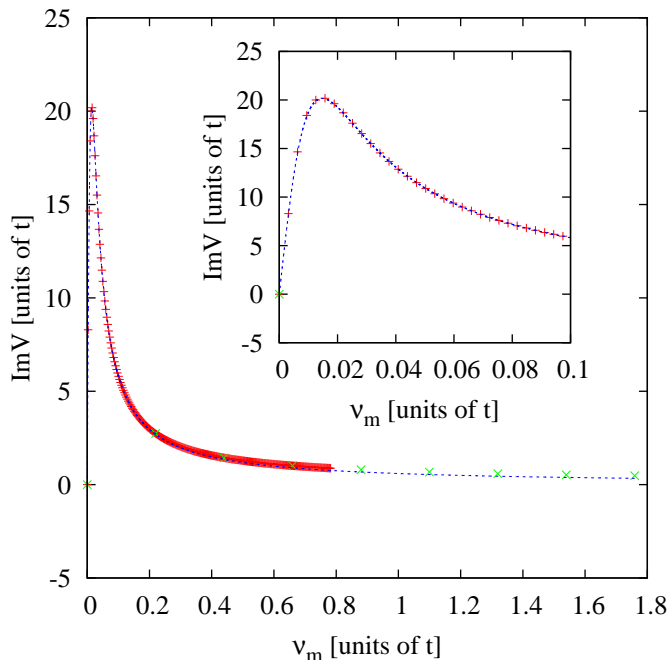


Figure 5.21: Fitting (5.49) to $\text{Im}(V)$ $\epsilon \approx 0.30t$, values represented by red crosses calculated at a lower temperature for verification purposes

at much lower temperature show that the Matsubara-frequency dependence of V and W does not change at lower temperature. This implies that our calculations are approximately equivalent to calculations at $T = 0$.

5.2.7 Combinations of effective interactions

In general, it is convenient to work with as small a number of divergent quantities as possible. Since our calculations so far have shown that $V \approx -W$ at $\mathbf{p} = \nu_m = 0$, we combine V and W into $V+W$ and $V-W$. This can be interpreted as separating the amplitude from the phase mode as discussed in section 4.1.1. Only the phase mode shows the divergence for $\mathbf{p} = \nu_m = 0$, while the amplitude mode is massive in the symmetry-broken regime.

Momentum dependence We analyze the momentum dependence of $V - W$ and $V + W$ at $\nu_m = 0$ as is done for V and W individually above. The amplitude-mode contribution $V + W$ is fitted to

$$\frac{1}{\beta |\mathbf{p}|^2 + A} + \gamma, \quad (5.50)$$

see Fig. 5.22. The fit reproduces the numerically-calculated behavior. For small

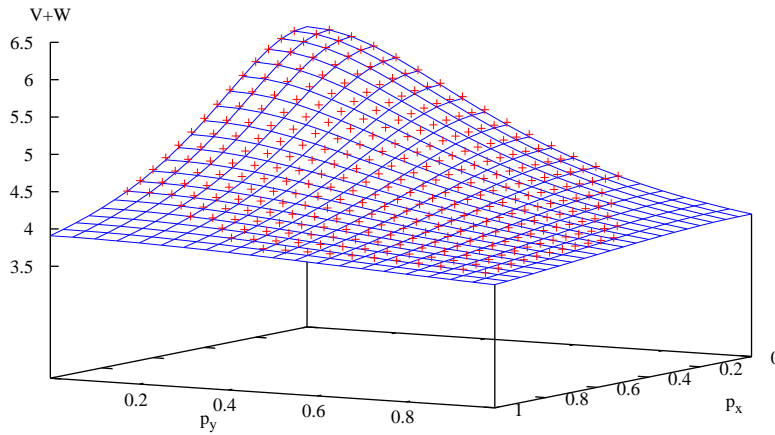


Figure 5.22: Fitting (5.50) to $V+W$ plotted in units of t . $A \approx -0.37t^2$, $\beta = -1.32t$, $\gamma \approx -3.32t$

momenta, the agreement is better, while for larger momenta, deviations become larger, but vanish along the diagonal. This is due to an anisotropy in the numerical data which is not captured by the approximation (5.50).

For $V - W$, we proceed by fitting (5.47) to the numerically-obtained data. We plot the result in figure 5.23. We see that the numerical data is reproduced by

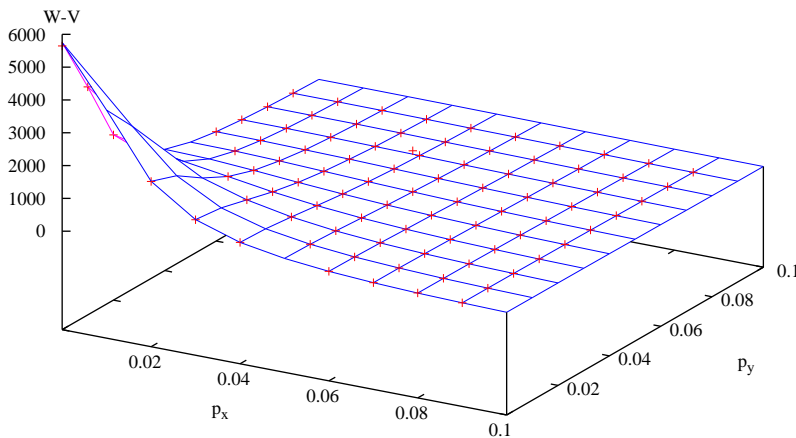


Figure 5.23: Fitting (5.47) to $V - W$ (plotted in units of t and with inverted sign for easier evaluation). $\alpha \approx -0.57t^2$, $\beta = 0.46t$, $\gamma = -3.33t$

the rational function (5.47). For intermediate momenta along the diagonal, the fit is not optimal as deviations of up to 25% occur. The situation is better for large momenta, where deviations of about 10% are common.

Energy dependence The energy dependence of $V + W$ and $V - W$ is to be included in the approximate formula (5.50) in the spirit of the modification turning (5.47) into (5.48), e.g. by adding $\beta_\nu \nu_m^2$ to the denominator. For $V + W$ which

is interpreted as the amplitude mode, this presents a challenge. We consider the approximation function

$$\frac{t^2}{\beta_p |\mathbf{p}|^2 + \beta_\nu \nu_m^2 + \alpha} + \gamma. \quad (5.51)$$

Contemplating the left-hand graph of figure 5.24, we become aware of a shoulder

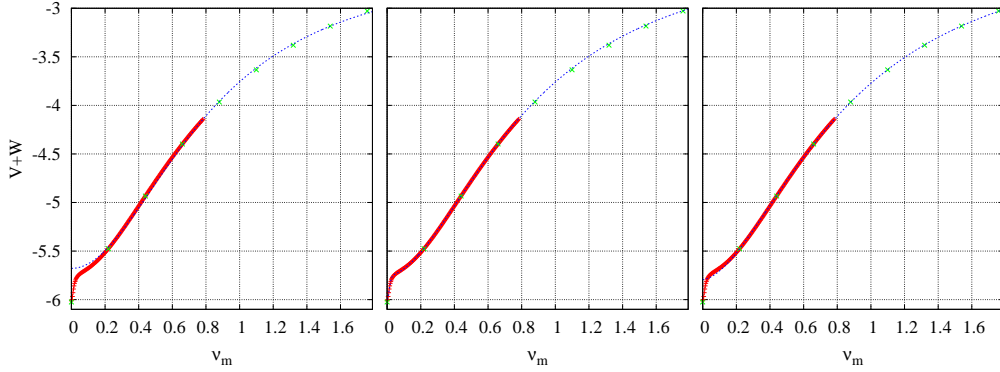


Figure 5.24: Matsubara-frequency dependence of $V + W$ calculated at two temperatures far below T_c . The blue lines are least-squares fits of (from left to right) (5.51), (5.52), (5.53). The parameters used in the fits are, from left to right, $\{\beta_\nu = -0.47t^{-1}, \alpha = -0.31t, \gamma = -2.50t\}$, $\{\beta_\nu = -0.40t^{-1}, \alpha = -0.29t, \gamma = -2.31t, \alpha_{\text{exp}} = 0.24t, \beta_{\text{exp}} = 3030t^{-2}\}$, $\{\beta_\nu = -0.37t^{-1}, \alpha = -0.28t, \gamma = -2.23t, r = 1.72\}$

close to zero frequency, which is not captured by (5.51). We employ the alternative approximation function

$$\frac{t^2}{\beta_p |\mathbf{p}|^2 + \beta_\nu \nu_m^{1.8} + \alpha} + \gamma - \alpha_{\text{exp}} e^{-\beta_{\text{exp}} \nu_m^2} \quad (5.52)$$

As seen from the middle graph of figure 5.24, the numerical data is reproduced including the shoulder. In order to reduce the number of free parameters compared to (5.52) but improve the fit compared to (5.51), we study the third alternative

$$\frac{t^2}{\beta_p |\mathbf{p}|^2 + \beta_\nu \nu_m^r + \alpha} + \gamma, \quad (5.53)$$

which is expanded in comparison to (5.48) and (5.51) in that the exponent of ν_m in the denominator is not fixed. This yields the right-most graph. Again, the important value at $\nu_m = 0$ is underestimated, albeit less so than in the left-hand plot. We note that the best fits (5.52) and (5.53) are obtained for an exponent of ν_m different from 2 in the denominator. As the exponent of $|\mathbf{p}|$ was 2, this implies a small change in the linearity of the dispersion of the amplitude mode.

The unmodified ansatz (5.48) already reproduces the numerically-obtained results for $V - W$ upon properly adjusting the parameters, as Fig. 5.25 illustrates. The agreement is good for small Matsubara frequencies. In the inset, we see that

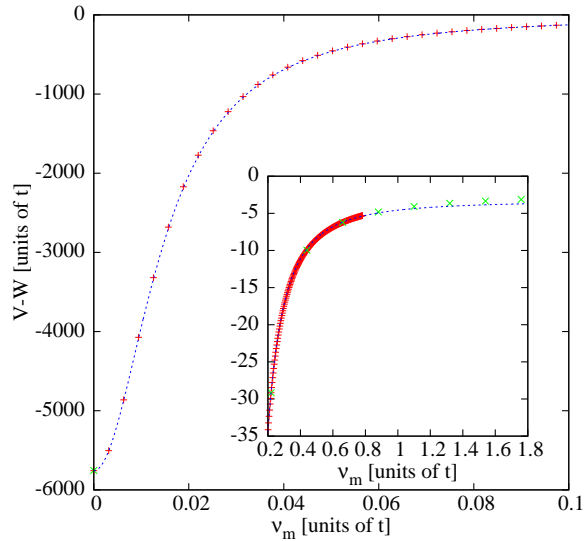


Figure 5.25: Fitting (5.48) to $V - W$. $\alpha = -0.58t^2$, $\beta = 0.46t$, $\gamma = -3.33t$

the large-frequency behavior is not captured optimally, which is due to our choice of γ , having taken it from the fit in figure 5.23. However, the exponent 2 for ν_m is confirmed by the fit. This confirms the linearity of the dispersion relation of the Goldstone mode connected to $V - W$.

The imaginary part of V is present in both $V + W$ and $V - W$. Since the imaginary part of W is zero, the imaginary part of the linear combinations is the same as the imaginary part of V and can be approximated accordingly.

This concludes our resummation study of the attractive Hubbard model including the anomalous non-Cooper vertices Ω_i . The study has provided an overview of the momentum, energy, and Nambu index dependence of the effective interaction. Furthermore, we have learned that the inclusion of effective interactions with an odd number of inwards-pointing legs leads to quantitative changes in certain cases. However, no qualitative differences have become apparent in our analysis. We note in particular that the dispersion relation of the massless Goldstone mode is linear as expected.

5.3 Renormalization group

The one-particle irreducible (1PI) scheme (section 3) of the functional renormalization group (fRG) is applied in the Katanin truncation (section 3.6) to the attractive Hubbard model as given by the Hamiltonian (5.34). Due to the numerical complexity of the problem, the effective interactions as well as the self-energy must be approximated. In the approximation chosen, we neglect the normal self-energy and assume the anomalous self-energy to be equal to its value at zero energy and the effective interactions to be equal to their value at zero energy for all energies. To take into account the momentum dependence, the Brillouin zone is split into patches, each of which is bisected by the Fermi surface. All momenta in a given

patch are projected onto the midpoint of the Fermi surface in the same patch. For symmetry-broken situations, the approximation for the energy dependence as well as the placement of the sampling points on the Fermi surface correspond to an overestimation of the effective interaction strength. This leads to a divergence of the flow if a momentum cutoff with an insufficiently strong external pairing field or an interaction flow with an insufficiently strong counterterm is employed. The divergence problem can be remedied by employing the interaction flow and including a counterterm for the anomalous self-energy as exemplified for a reduced model in section 4.2.

5.3.1 Flow equations

In this section, we derive an explicit analytic form of the Katanin-truncated (see section 3.6) one-particle irreducible functional renormalization group flow equations (see section 3.5) for the Hubbard model (5.34) including superconductivity according to (5.9). To accomplish this, we need the explicit form of the Green's functions. This can be obtained from the Green's function (5.13) by multiplying both self-energy components Δ , Σ as well as the Green's function by the cutoff function χ . It reads

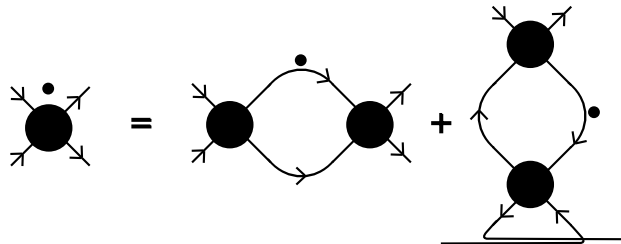
$$\mathbb{G}(k) = \frac{\chi(k)}{\omega_n^2 + E(k)^2} \begin{pmatrix} -i\omega_n - \xi_{\mathbf{k}} - \chi(k)\Sigma(k) & \chi(k)\Delta(k) \\ \chi\Delta^*(k) & -i\omega_n + \xi_{\mathbf{k}} + \chi(k)\Sigma(k) \end{pmatrix} \quad (5.54)$$

$$=: \begin{pmatrix} G(k) & F(k) \\ F^*(k) & H(k) \end{pmatrix}, \quad (5.55)$$

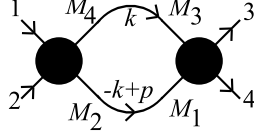
where

$$E(k) = \sqrt{(\xi_{\mathbf{k}} + \chi(k)\Sigma(k))^2 + |\chi(k)\Delta(k)|^2}.$$

In order to obtain an analytic expression treatable with numerical methods, we consider the flow equation



derived in section 3. In the following, we construct an analytical expression corresponding to the particle-particle diagram on the right-hand side. Note that because of the renaming (5.9) of particles into holes and vice versa in the introduction of the Nambu index, the particle-particle diagram here does not correspond to the electronic particle-particle channel, but is a part of the electronic particle-hole channel in the symmetric phase. We assign labels to the particle-particle diagram



abbreviating $p_i N_i$ as i and defining $p := p_1 + p_2$. Employing the diagrammatic rules from section 3.5 yields

$$-\frac{1}{8} \sum_{k, \mathbf{M}} \mathbb{U}_{N_1 N_2 M_4 M_2}(p_1, p_2, k) \mathbb{U}_{M_3 M_1 N_3 N_4}(k, -k + p, p_3) \times \partial_\Lambda [\mathbb{G}_{M_3 M_4}(k) \mathbb{G}_{M_1 M_2}(-k + p)], \quad (5.56)$$

where \mathbb{U} stands in for γ_2 . A factor $1/2$ beyond the diagrammatic rules appears because of the replacement $\mathbb{G}\mathbb{S} \rightarrow \partial_\Lambda \mathbb{G}\mathbb{G}/2$ from the Katanin truncation. We would like to bring (5.56) into a form suitable for numerical evaluation. In particular, it is our goal to place the origin of the integration domain symmetrically with respect to the integrand's maxima. We consider the case where all external energies are zero. For the interaction flow scheme, these maxima are located at the momenta \mathbf{k} with $\xi_{\mathbf{k}} = 0$ or $\xi_{\mathbf{k}+\mathbf{p}} = 0$ due to the energy denominators of the Green's functions. For the momentum-shell cutoff scheme, the maxima occur on the line where the cutoff Λ is equal to the dispersion $\xi_{\mathbf{k}}$ or $\xi_{-\mathbf{k}+\mathbf{p}}$. We rewrite the scale derivative of the propagators in (5.56):

$$\partial_\Lambda (\mathbb{G}_{M_3 M_4}(k) \mathbb{G}_{M_1 M_2}(-k + p)) = \dot{\mathbb{G}}_{M_3 M_4}(k) \mathbb{G}_{M_1 M_2}(-k + p) + \mathbb{G}_{M_3 M_4}(k) \dot{\mathbb{G}}_{M_1 M_2}(-k + p) \quad (5.57)$$

In a momentum-shell cutoff scheme, the dotted term's weight is concentrated around the momentum shells on which the cutoff Λ equals the energy $\xi_{\mathbf{k}}$ or $\xi_{\mathbf{k}+\mathbf{p}}$, respectively, as argued above. Placing the origin of the Brillouin zone at $\mathbf{k} = 0$, we note that this placement is asymmetric with the weight distribution of the second term on the right-hand side of (5.57). We therefore shift the origin in this integration by shifting the integration variable $k \rightarrow -k + p$, and also exchange the Nambu index names $M_1 \leftrightarrow M_3$, $M_2 \leftrightarrow M_4$ in the summation, yielding

$$\mathbb{G}_{M_3 M_4}(k) \dot{\mathbb{G}}_{M_1 M_2}(-k + p) \rightarrow \dot{\mathbb{G}}_{M_3 M_4}(k) \mathbb{G}_{M_1 M_2}(-k + p). \quad (5.58)$$

The differentiation has moved from one Green's function to the other. We thus find that the integrand of (5.56) consists of two terms:

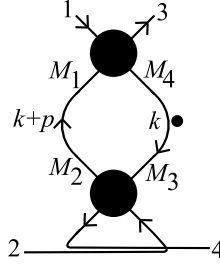
$$\mathbb{U}_{N_1 N_2 M_4 M_2}(p_1, p_2, k) \mathbb{U}_{M_3 M_1 N_3 N_4}(k, -k + p, p_3) \dot{\mathbb{G}}_{M_3 M_4}(k) \mathbb{G}_{M_1 M_2}(-k + p) + \mathbb{U}_{N_1 N_2 M_2 M_4}(p_1, p_2, -k + p) \mathbb{U}_{M_1 M_3 N_3 N_4}(-k + p, k, p_3) \dot{\mathbb{G}}_{M_3 M_4}(k) \mathbb{G}_{M_1 M_2}(-k + p). \quad (5.59)$$

These terms are identical due to the antisymmetry of \mathbb{U} . Therefore, we use

$$\text{PP}(1234) := -\frac{1}{4} \sum_{k, \mathbf{M}} \mathbb{U}_{N_1 N_2 M_4 M_2}(p_1, p_2, k) \mathbb{U}_{M_3 M_1 N_3 N_4}(k, -k + p, p_3) \times \dot{\mathbb{G}}_{M_3 M_4}(k) \mathbb{G}_{M_1 M_2}(-k + p) \quad (5.60)$$

for the numerical treatment, where $i = 1 \dots 4$ as arguments abbreviate $N_i p_i$. Note that for zero energy, the sign of the argument of the Green's function can be inverted. This allows us to use the same routines for the calculation of this product of Green's functions as for the calculation of the particle-hole contributions.

We turn to the particle-hole diagram



containing the contributions of the electronic particle-particle channel. Employing the diagrammatic rules of section 3.5 leads to the expression

$$\frac{1}{2} \sum_{k, \mathbf{M}} \mathbb{U}_{M_3 N_2 M_2 N_4}(k, p_2, k+q) \mathbb{U}_{N_1 M_1 N_3 M_4}(p_1, k+q, p_3) \times \partial_\Lambda [\mathbb{G}_{M_3 M_4}(k) \mathbb{G}_{M_1 M_2}(k+q)], \quad (5.61)$$

where $q := p_3 - p_1$. A factor $1/2$ beyond the diagrammatic rules appears because of the replacement $\mathbb{G}\mathbb{S} \rightarrow \partial_\Lambda \mathbb{G}\mathbb{G}$, as for the particle-particle diagram. Note that (5.61) needs to be antisymmetrized with respect to the incoming four-momenta p_1, p_2 and Nambu indices N_1, N_2 . We treat the differentiation of (5.61) as in (5.57) and (5.59) to obtain

$$\begin{aligned} & \mathbb{U}_{M_1 N_2 M_4 N_4}(k-q, p_2, k) \mathbb{U}_{N_1 M_3 N_3 M_2}(p_1, k, p_3) \dot{\mathbb{G}}_{M_3 M_4}(k) \mathbb{G}_{M_1 M_2}(k-q) + \\ & \mathbb{U}_{M_3 N_2 M_2 N_4}(k, p_2, k+q) \mathbb{U}_{N_1 M_1 N_3 M_4}(p_1, k+q, p_3) \dot{\mathbb{G}}_{M_3 M_4}(k) \mathbb{G}_{M_1 M_2}(k+q). \end{aligned} \quad (5.62)$$

Plugging (5.62) into (5.61) yields

$$\begin{aligned} \text{PH}(1234) := & \frac{1}{2} \sum_{k, \mathbf{M}} \mathbb{U}_{M_1 N_2 M_4 N_4}(k-q, p_2, k) \mathbb{U}_{N_1 M_3 N_3 M_2}(p_1, k, p_3) \\ & \times \dot{\mathbb{G}}_{M_3 M_4}(k) \mathbb{G}_{M_1 M_2}(k-q) + \\ & \mathbb{U}_{M_3 N_2 M_2 N_4}(k, p_2, k+q) \mathbb{U}_{N_1 M_1 N_3 M_4}(p_1, k+q, p_3) \\ & \times \dot{\mathbb{G}}_{M_3 M_4}(k) \mathbb{G}_{M_1 M_2}(k+q), \end{aligned} \quad (5.63)$$

where i as an argument abbreviates $N_i p_i$. The full symbolic flow equation thus reads

$$\dot{\mathbb{U}}(1234) = 4\text{PP}(1234) + 2\text{PH}(1234) - 2\text{PH}(2134), \quad (5.64)$$

where the antisymmetrization of the particle-hole term is denoted explicitly. The Matsubara sums in the integrands appearing on the right-hand side can be evaluated explicitly if we restrict ourselves to energy-independent couplings and self-energies. The resulting expressions are listed in appendix C without scale differentiation, which will be carried out numerically.

To find a more explicit form of the flow equation (3.29) for the self-energy, we employ (4.6) to obtain

$$\begin{aligned}\dot{\Sigma}_{N_1 N_2}(p) &= \sum_{k, M_1 M_2} \mathbb{U}_{M_1 N_2 M_2 N_1}(k, p, k) \mathbb{S}_{M_1 M_2}(k) \\ &= \sum_{k, M_1 M_2} \mathbb{U}_{M_1 N_2 M_2 N_1}(k, p, k) \dot{\chi}(k) \frac{\partial \mathbb{G}_{M_1 M_2}}{\partial \chi}(k)\end{aligned}\quad (5.65)$$

Since \mathbb{U} is assumed to be independent of energy, (5.65) shows that no energy dependence of Σ is generated in the flow. We can therefore do the Matsubara sums analytically, and list the result in appendix D. This concludes our derivation of the one-particle irreducible renormalization group flow equations for the Hubbard model in the Katanin truncation.

5.3.2 Numerical setup

We would like to solve the flow equations (5.65) and (5.64) numerically at $T = 0$. To reach this goal, we need to develop an implementation which runs in appropriate timeframes on the computers of 2007. The numerical complexity of the flow equations is determined by the discretization used for the effective interaction \mathbb{U} . We engage in a thought experiment to gauge the numerical complexity of the problem. Suppose that we choose to represent each momentum argument of \mathbb{U} by taking into account $L_{\mathbf{k}}$ distinct values. Similarly, we represent a Matsubara frequency argument by L_{ω} distinct values. Without exploiting the symmetries of \mathbb{U} , we note that we have to store $L_{\mathbf{k}}^3 L_{\omega}^3$ values, and, more importantly, to solve an integro-differential equation for as many flowing variables. Let's assume that $L_{\mathbf{k}} = 100$, $L_{\omega} = 10$, and that we need 100 discrete steps for the integration of the differential equation, at each of which an integral kernel requiring 100 floating point operations must be evaluated 1000 times to obtain a sufficiently accurate estimate of the integration over the Brillouin zone. There are also 16 combinations of the four Nambu indices, bringing the total number of floating point operations necessary to 10^{17} , implying that a current machine doing 1000 million floating point operations per second would take ten thousand days to finish a single fRG integration. This is a rough estimate, and experience suggests that such integrations may take even longer in reality due to administrative overheads.

To curb the number of floating point operations necessary for the integration of the flow equations, we drop the energy-dependence of \mathbb{U} , assuming $\mathbb{U}(\omega_1, \omega_2, \omega_3) = \mathbb{U}(0, 0, 0)$ for all energies ω_i . This means in particular that the total energy of the particles involved in the interaction as well as their energy difference are zero. This implies that we are treating the part of the effective interaction most singular in the energies as representative for the whole effective interaction, overestimating its total weight and therefore also the tendency towards symmetry breaking of the physical system.

A parametrization taking into account partially the momentum dependence of the effective interaction is the so-called ‘‘patching’’ as described for example

by Rohe (2005). The Brillouin zone is split into patches as shown in Fig. 5.26. The functional value of the effective interaction at the mid-angle of the patch

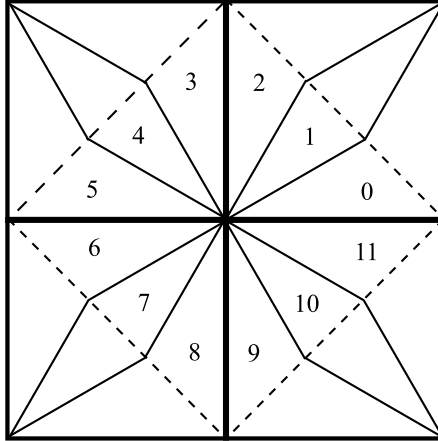


Figure 5.26: Patching of the Brillouin zone used with varying total number of patches in the numerical calculations. Every patch covers the same angle.

and on the Fermi surface is assumed to be also valid for all other momenta in the patch. Thus taking only the momentum dependence along the Fermi surface into account is motivated by the finding that the dependence perpendicular to the Fermi surface is irrelevant in the RG sense for the momentum-shell flow without symmetry-breaking (Shankar (1991, 1994)).

For the self-energy, we choose an analogous parametrization as for the effective interaction \mathbb{U} . This implies an overestimation of the order parameter leading to a suppression of the flow of the effective interaction due to the removal of small energy denominators in the loops of (5.64). Furthermore, we neglect the effect of the normal self-energy by setting it to zero in the flow. This has the important consequence that the Fermi surface does not shift in the flow. In particular, phenomena such as symmetry-breaking Fermi surface deformations (Metzner et al. (2003); Yamase and Kohno (2000); Yamase et al. (2005)) are therefore ignored.

The integration of the bubble integrals of appendix C is simplified numerically by our choice of the Brillouin zone origin in section 5.3.1. We split each patch into subpatches according to the Gaussian integration rule and integrate over the lines separating the subpatches. As these lines run perpendicular to the lines of maximum weight of the bubble integrands and the patches are slim, a small number (5-7) of lines per patch suffices to approximate the integral over the patch to the desired accuracy. Furthermore, the parts of each line where the integrand is maximal are the vicinity of the Fermi surface and the vicinity of the points where the kinetic energy of an internal line equals the cutoff. For these regions, we choose a significantly finer mesh for the integration as for the rest of the line.

We turn to the symmetries of the problem to further reduce its numerical complexity. The symmetry of the Brillouin zone under reflections along the k_x -axis, k_y -axis and the diagonal allows us to consider one of the momentum arguments of \mathbb{U} only in the Brillouin zone's first octant. Time reversal symmetry implies that

flipping all Nambu indices of the effective interaction leaves it invariant if there is an even number of + indices, and leads to a factor -1 if there is an odd number of + indices. The antisymmetry of \mathbb{U} under the exchange of the outgoing or incoming legs implies that we can choose to consider only one of the Nambu index combinations $(+-)$, $(-+)$. For $(--)$ and $(++)$, we need to consider only one half of the possible momentum combinations. We ignore the simplification possible by exploiting spin rotation invariance because after employing the above simplifications, spin rotation invariance only reduces the number of flowing couplings by another $\sim 20\%$. This discussion of the effect of symmetries on the numerical complexity concludes the setup of the numerical calculation.

5.3.3 Momentum-shell flows

We numerically integrate the flow equations (5.64) and (5.65) as outlined in section 5.3.2, employing a soft momentum-shell cutoff

$$\chi(\Lambda, \xi) = 1 - \frac{1}{e^{\alpha(|\xi|-\Lambda)/\Lambda} + 1}. \quad (5.66)$$

Our results do not depend on α , which adjusts the sharpness of the cutoff. Our main goal is to obtain a decent approximation for the superconducting order parameter Δ , which is given by the anomalous part of the self-energy. We include an initial order parameter in the flow as in section 4, depicting the resulting flow of the order parameter in Fig. 5.27. On the left, we plot a flow for which the

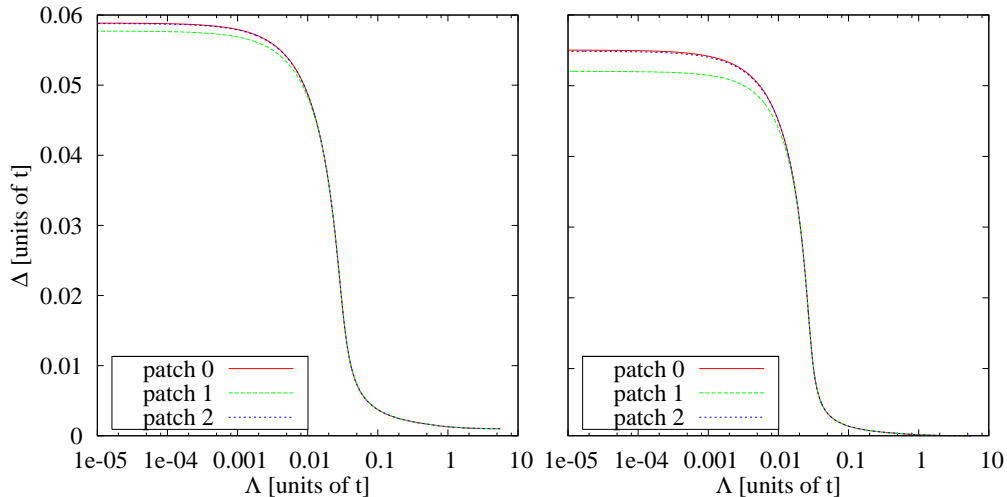


Figure 5.27: Momentum-shell flow of the order parameter. Twelve patches, quarter filling: $\mu = -1.41t$, $t' = -0.1t$; $U_0 = 1.5t$, $\Delta_{\text{ext}} = 10^{-3}t$ (left), $\Delta_{\text{ext}} = 5 \times 10^{-4}t$ (right).

maximum effective interaction is four times the bandwidth. Due to the limited phase space of this maximum effective interaction, this is still a well-controlled flow. However, from Fig. 4.3 in section 4.1.5 on flows for the charge-density-wave

mean-field problem, we learn that if the initial order parameter is about 1% of the final order parameter value, the error in the final order parameter as compared to the case of spontaneous symmetry breaking is already $\sim 20\%$. To check the internal consistency of our method, we note that by solving the BCS gap equation in the presence of a momentum-shell cutoff, the rule $\Delta = 2\Lambda_c$ can be inferred. The results of Reiss (2006) confirm this for the attractive Hubbard model. In our case, $\Lambda_c \approx 0.025t$, and we therefore expect an order parameter magnitude $\Delta \approx 0.05t$. The fRG yields $\Delta \approx 0.06t$ for $\Delta_{\text{ext}} \approx 0.02\Delta$, a deviation in the expected range. Reiss et al. (2007) find $\Delta \approx 0.026t$ and a corresponding Λ_c for similar parameters. In section 5.3.4, we see that the method used by Reiss et al. (2007) yields results agreeing better with the results obtained here for other fillings. To study the influence of the external field, we half the strength of the initial order parameter and plot the resulting flow of the order parameter on the right side of Fig. 5.27. While the final value of the order parameter is closer to the result estimated from the critical scale, the effective interaction has exceeded ten times the system's bandwidth in the flow.

If we employ too small an external field, the method breaks down. To illustrate this, we plot in Fig. 5.28 the relationship between a Cooper-channel effec-

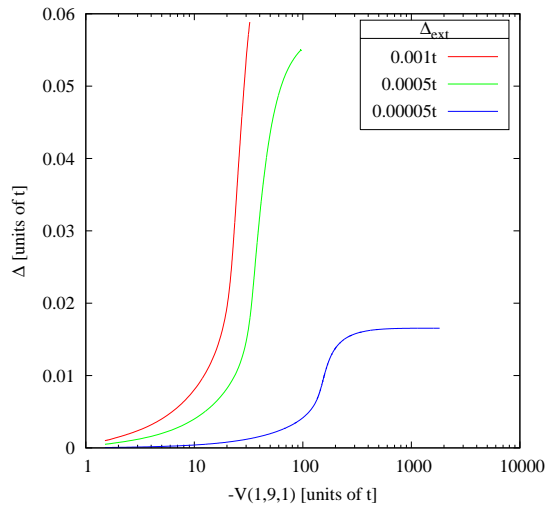


Figure 5.28: Magnitude of the order parameter in the flow against the Cooper-channel effective interaction in the flow, which starts at the bottom left of each graph and terminates at the top right. Twelve patches, quarter filling: $\mu = -1.41t$, $t' = -0.1t$; $U_0 = 1.5t$, Δ_{ext} varies, numbers in parentheses are patch numbers to be understood within the Nambu formalism (see text).

tive coupling and the order parameter for various external fields. The notation $A(P_1, P_2, P_3)$ for the momentum dependence of the effective interaction A , where $A \in \{U, X, V, W, \Omega_i\}$ in accordance with (5.45), is to be understood in the following way. Each P_i denotes the patch number of the i th momentum parameter of the matrix element A of \mathbb{U} from (5.45). Note that a negative Nambu index N_i reverses the sign of the i th momentum in comparison to the usual convention. The

notation properly defined, we note that for small external fields, beyond a certain magnitude of the effective interaction the increase of the effective interaction in the flow is not countered by an appropriate increase in the order parameter. The effective interaction diverges while the order parameter is essentially constant. This implies that the divergence is due to the unstable $\dot{V} \sim V^2$ structure of the effective interaction flow equation. The divergence prevents us from considering arbitrarily small external fields.

We consider the flow of the effective interactions to obtain an understanding of their relative importance in the system. From our resummation studies in section 5.2, we have learned that the Goldstone phase mode $V - W$ dominates for zero momentum transfer in the Nambu formalism, which is equivalent to zero total momentum if we transform back to the original ψ fields according to (5.9). In Fig. 5.29, we plot several flows from this channel. They dominate in magnitude

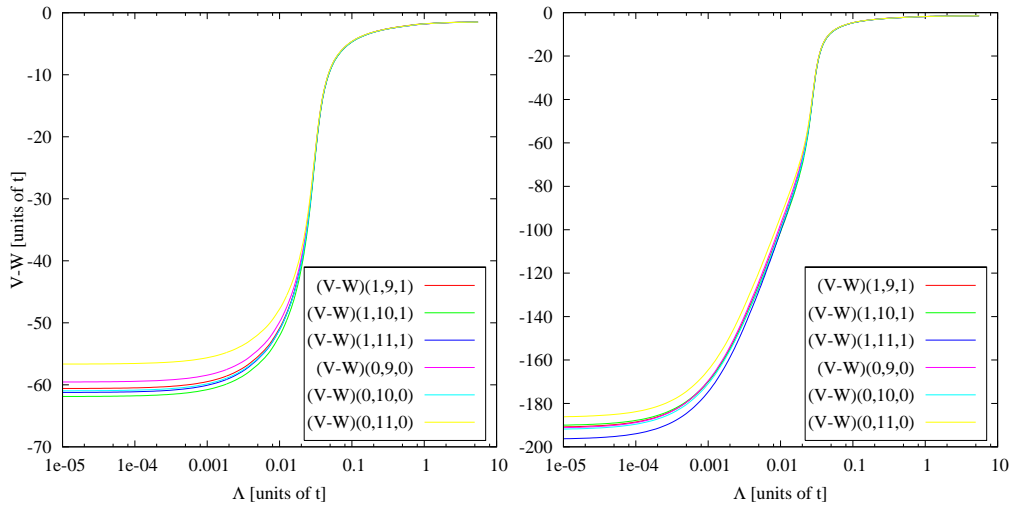


Figure 5.29: Momentum-shell flows of the effective interaction $V - W$ associated with the Goldstone mode. Twelve patches, quarter filling: $\mu = -1.41t$, $t' = -0.1t$; $U_0 = 1.5t$, $\Delta_{\text{ext}} = 10^{-3}t$ (left), $\Delta_{\text{ext}} = 5 \times 10^{-4}t$ (right), numbers in parentheses are patch numbers to be understood within the Nambu formalism.

all other effective interaction flows, including those not shown in the figure, and exhibit a spread of $\sim 10\%$ under variation of the momentum combination which decreases with decreasing external field. They are quite similar to the flows found by Salmhofer et al. (2004).

Complementing the phase mode is the amplitude mode. The effective interaction corresponding to the amplitude mode was found to drive the order parameter flow. Its flows are plotted in Fig. 5.30. The behavior is largely as expected from the discussion in section 4.1.4, exhibiting a peak at a certain scale which becomes sharper with decreasing Δ_{ext} and a saturation for small scales at a value smaller in magnitude than the maximal magnitude in the flow. The final value averaged over the momentum combinations in the figure is only weakly dependent on the strength of the external field. We discuss the flows for small external fields in

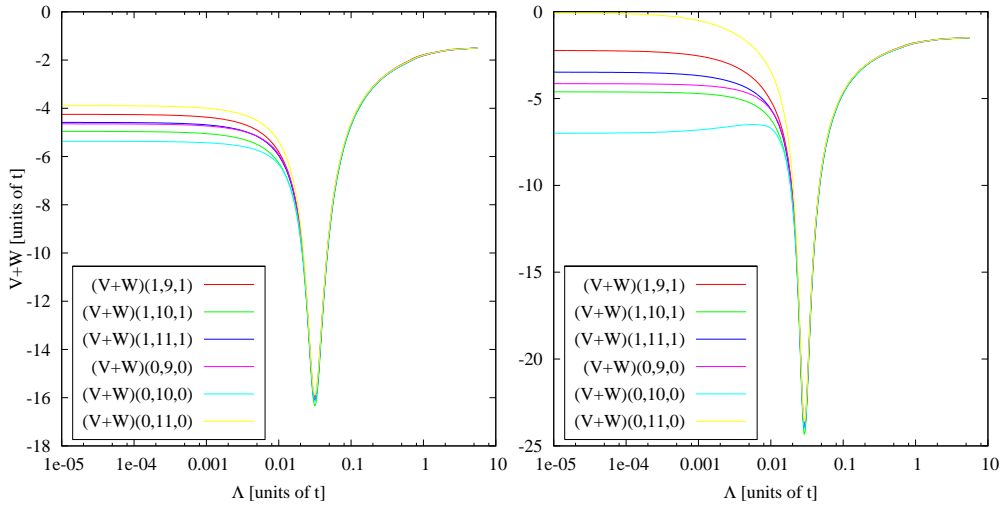


Figure 5.30: Momentum-shell flows of the effective interaction $V + W$ associated with the amplitude mode. Twelve patches, quarter filling: $\mu = -1.41t$, $t' = -0.1t$; $U_0 = 1.5t$, $\Delta_{\text{ext}} = 10^{-3}t$ (left), $\Delta_{\text{ext}} = 5 \times 10^{-4}t$ (right), numbers in parentheses are patch numbers to be understood within the Nambu formalism.

more detail. There is a peculiar non-monotonicity below Λ_c of individual flows, exemplified by the flow for patches $(0,10,0)$ in the right graph. This entails that the arguments of section 4.1.4 are not strictly true for the Hubbard model at very small external fields. However, the deviation from the predicted behavior is slight. We note that the final magnitude of $V + W$ is very small for certain momentum combinations. The last two observations lead us to investigate the spread of the final values, and we find that they vary by almost 100% about their average. The average, however, is quite similar to the average at larger external fields, a behavior which is comparable to the mean-field situation where the final value is only very weakly dependent on the external field, see Fig. 4.3 (bottom). It is noteworthy that the qualitative deviations from the mean-field model flows only appear if the weakness of the external field has already led to effective interactions much larger than the system's bandwidth.

We plot the flow of selected X (see \mathbb{U} from (5.45)) in Fig. 5.31. This selection includes the flows of the maximal and minimal final X as well as all X for which the first momentum is in the same Brillouin zone quadrant and the second and third momenta are the same as for the maximum and minimum case. We see that these effective interactions diverge for zero momentum transfer if Δ_{ext} is sent to zero. Note that this does not change into zero total momentum upon transformation to the ψ fields from (5.9) as for $V + W$ and $V - W$. Maximal and minimal final values are approximately equal in modulus for small Δ_{ext} , as their sum barely changes with decreasing Δ_{ext} . The divergence is an order of magnitude weaker than the divergence in the Cooper channel.

Since U (see \mathbb{U} from (5.45)) is related to V through symmetries, we finally study the $3 + 1$ effective interactions by plotting the flow of the maximal and minimal

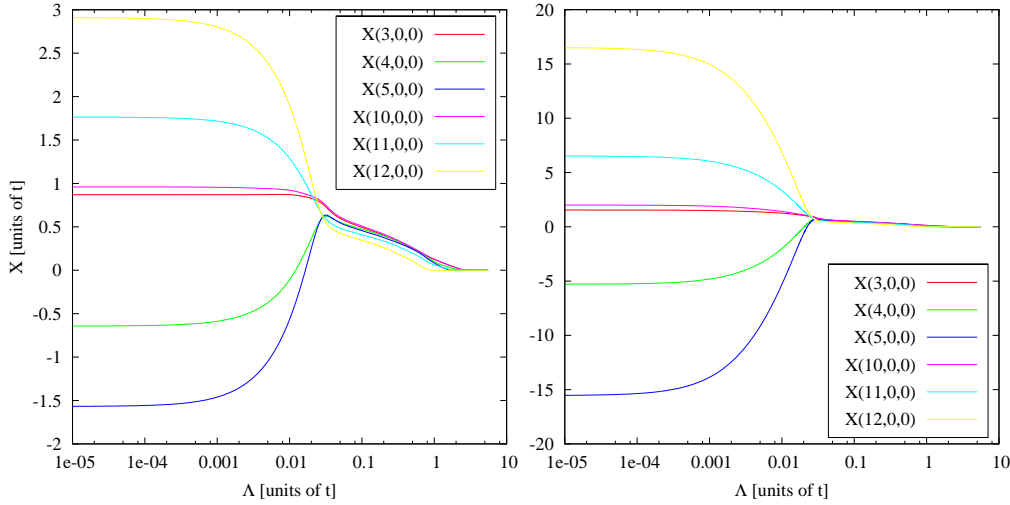


Figure 5.31: Momentum-shell flow of the maximal, minimal, and surrounding X . Twelve patches, quarter filling: $\mu = -1.41t$, $t' = -0.1t$; $U_0 = 1.5t$, $\Delta_{\text{ext}} = 10^{-3}t$ (left), $\Delta_{\text{ext}} = 5 \times 10^{-4}t$ (right). Parameters of X are patch numbers to be understood in the Nambu formalism.

final Ω_i in Fig. 5.32. Ω_2 and Ω_4 are not plotted as they can be obtained from Ω_1 and Ω_3 by exploiting time-reversal invariance and the antisymmetry of \mathbb{V} under commutation of the first or the second pair of parameters. We observe that while the momentum combinations in the figure imply that the 3+1 effective interactions peak for zero momentum transfer, this does not change into zero total momentum upon transformation to the ψ fields from (5.9) as for $V + W$ and $V - W$. We note that the final value of both Ω_1 and Ω_3 is singularly dependent on Δ_{ext} . As this final value increases with decreasing Δ_{ext} , the relative difference between Ω_1 and Ω_3 becomes less pronounced. It is possible that this difference is an artifact of our parametrization which places the first three momentum arguments of the effective interaction on the Fermi surface, but not necessarily the fourth. The Ω_i are comparable in strength to the X , which also diverge for zero momentum transfer. Comparing the magnitude of the 3 + 1 effective interactions with the amplitude and phase mode studied before, we find the phase mode to be orders of magnitude stronger. The amplitude mode is weaker as it is unchanged by reducing the external field, while Ω_1 and Ω_3 both diverge. We see in Fig. 5.33 that the 3 + 1 linear combinations also diverge if the external field is sent to zero. These divergences indicate that the 3 + 1 effective interactions are not completely negligible. However, as they remain much smaller in the flow than both V and W , their exclusion or inclusion is unlikely to cause qualitatively different behavior.

We conclude our investigation of the momentum-shell flow and study the dependence of the order parameter Δ on the bare interaction U_0 and the chemical potential μ in the attractive Hubbard model at zero temperature employing the interaction flow. This yields results closer to the ones published previously by Reiss et al. (2007); Reiss (2006).

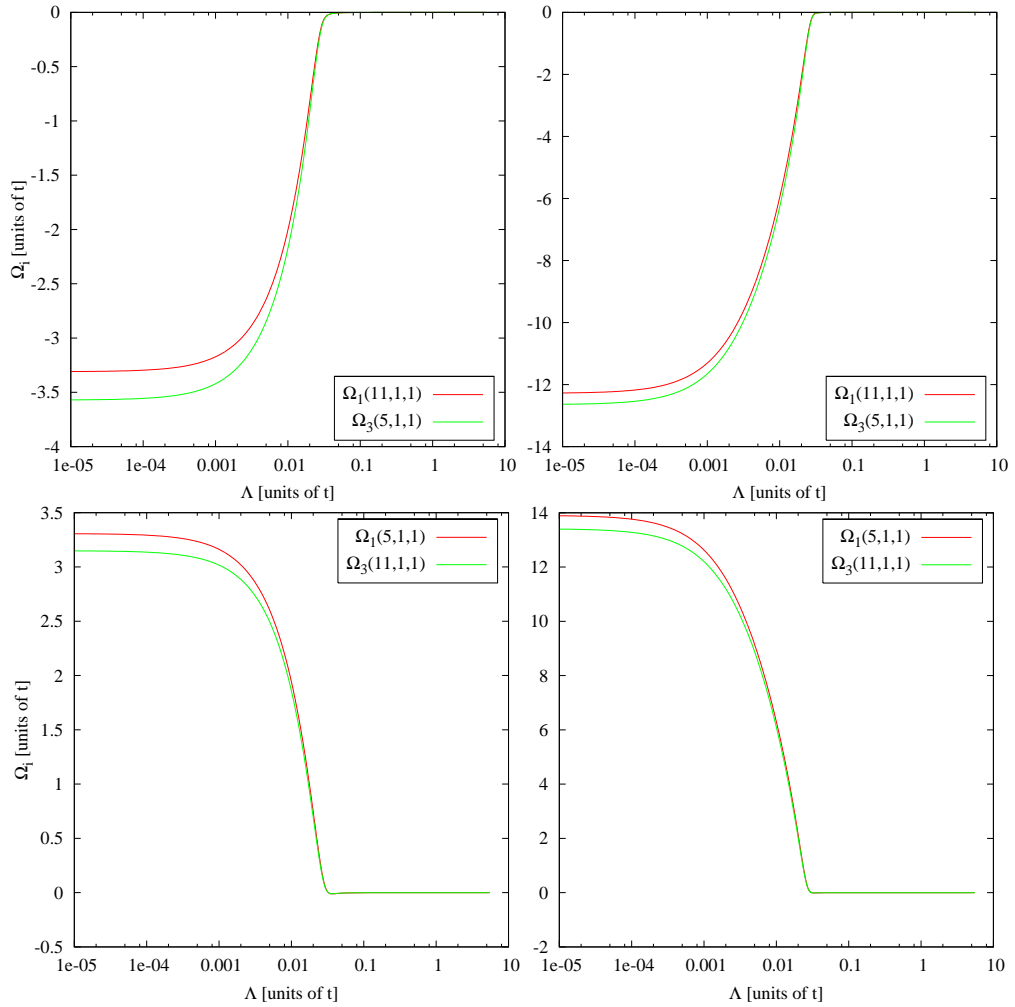


Figure 5.32: Momentum-shell flow of the maximum Ω_i . Twelve patches, quarter filling: $\mu = -1.41t$, $t' = -0.1t$; $U_0 = 1.5t$, $\Delta_{\text{ext}} = 10^{-3}t$ (left), $\Delta_{\text{ext}} = 5 \times 10^{-4}t$ (right). Parameters of Ω_i are patch numbers to be understood in the Nambu formalism.

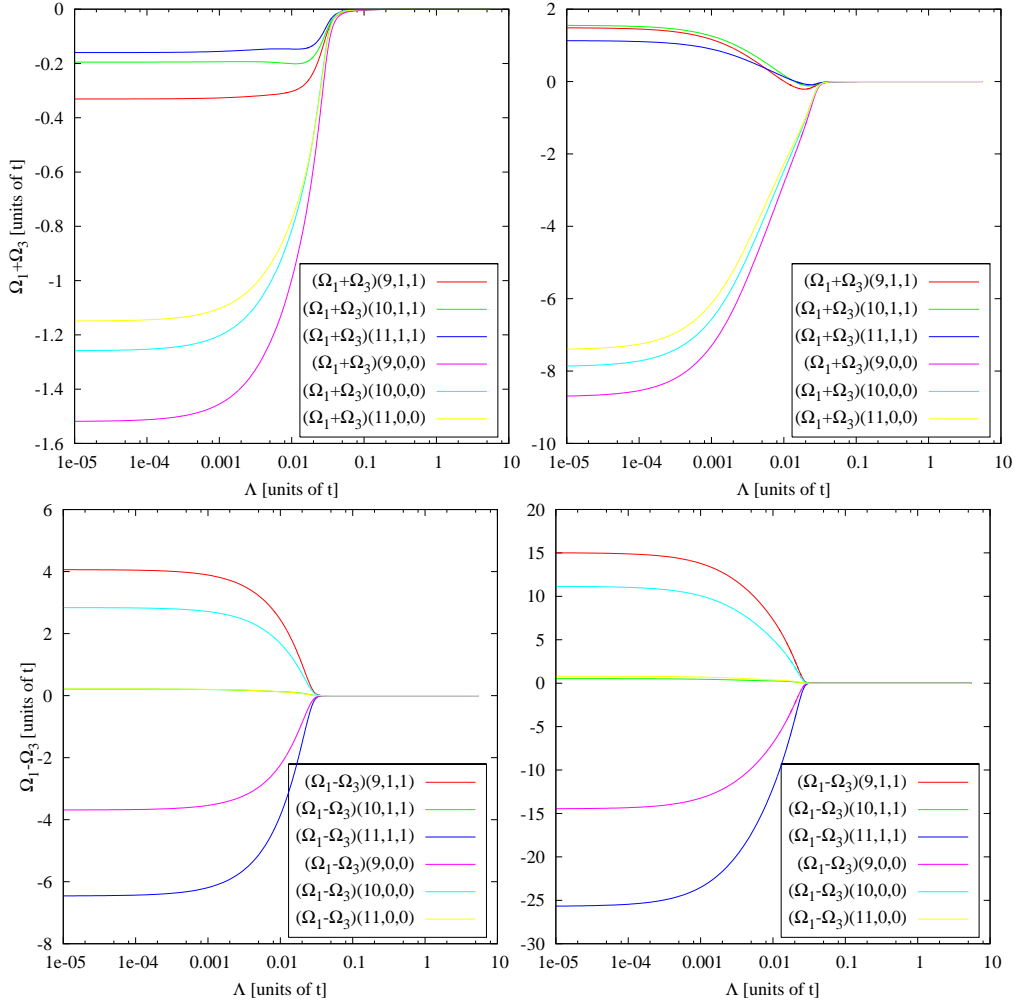


Figure 5.33: Momentum-shell flow of linear combinations of the 3 + 1 effective interactions. Twelve patches, quarter filling: $\mu = -1.41t$, $t' = -0.1t$; $U_0 = 1.5t$, $\Delta_{\text{ext}} = 10^{-3}t$ (left), $\Delta_{\text{ext}} = 5 \times 10^{-4}t$ (right). Numbers in parentheses are patch numbers to be understood as parameters of the effective interaction in the Nambu formalism.

5.3.4 Interaction flows

We numerically integrate the flow equations (5.64) and (5.65) as outlined in section 5.3.2, employing the interaction flow (Honerkamp et al. (2004)) and including a counterterm as in section 4.2. The cutoff function is characterized by

$$\chi(\Lambda) = \sqrt{\Lambda}$$

as in (4.11). This is equivalent to turning on the interaction linearly from 0 at $\Lambda = \Lambda_i = 0$ to its bare value U_0 at $\Lambda = \Lambda_f = 1$. The anomalous part of the Green's function (5.54) is considered to stem from an external field Σ_i and a counterterm Δ_c , the difference between the two constituting an effective external field Δ_{eff} , in analogy to (2.14). The cut-off Green's function is given schematically as

$$\mathbb{G}^{-1} = \frac{\mathbb{Q}_0 + \Delta_c}{\chi} - \Sigma, \quad (5.67)$$

where the counterterm has been taken into account as part of the bare propagator, while Σ_i will be included as the initial condition for the anomalous self-energy.

In Fig. 5.34 we show examples of the flow of the effective order parameter Δ_{eff}

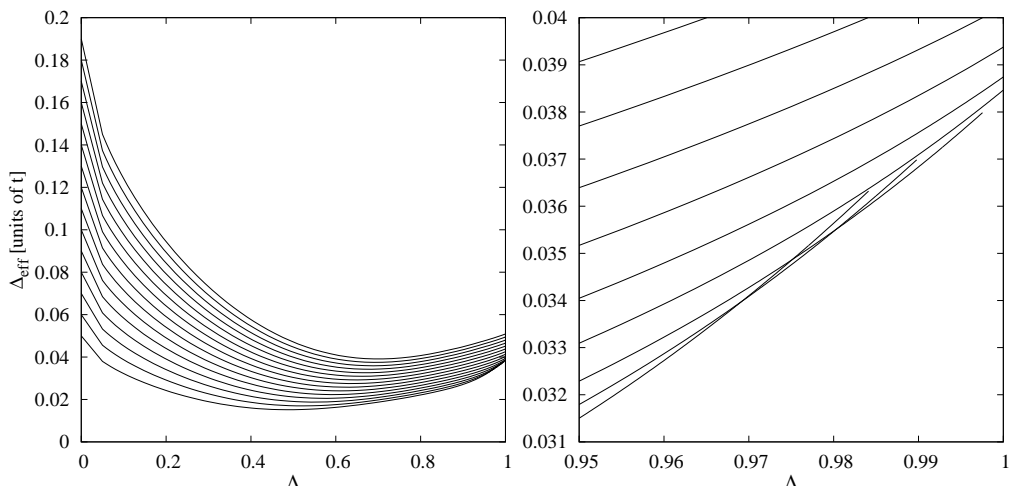


Figure 5.34: Interaction flows of $\Delta_{\text{eff}} = \Delta_c - \chi\Sigma_{+-}$ for patch 1 at $U_0 = 1.5t$, $t' = -0.1t$, $\mu = -1.41t$ (quarter filling), Δ_c from $0.05t$ to $0.19t$

for varying counterterms. The flows terminate if the maximum effective interaction exceeds four times the bandwidth, i.e. if the flow leaves the weak-coupling regime, or if Λ reaches $\Lambda_f = 1$. We see in the left diagram that the flows no longer converge onto a single strong attractor as for the mean-field case pictured in Fig. 4.9. Studying the final 5% of the flow shown in the right plot of Fig. 5.34 reveals that there exists a set of small counterterms for which the flows cross, leaving the weak-coupling regime, and a minimum counterterm for which the flow ends at $\Lambda_f = 1$. The flows for counterterms whose strength is just beyond this minimum counterterm terminate closer to each other than do the flows for larger counterterms. The minimum counterterm is approximately twice as strong as the final

order parameter value obtained in the minimum counterterm flow. The behavior described above is interpreted as being analogous to the strong-attractor behavior in the mean-field case. The overestimation of the order parameter value for larger counterterms is attributed to the overestimation of the gap in the flow due to the neglect of the order parameter's energy dependence and momentum dependence perpendicular to the Fermi surface. Consequently, we choose the minimum order parameter obtainable by terminating the flow at Λ_f in the weak-coupling regime as our approximation for the physical order parameter. Note that this final value is approximately 20% smaller than the final value obtained with the momentum-shell method in section 5.3.3, which is biased by a finite, albeit small, external field.

5.3.5 Order parameter for superconductivity

Fig. 5.35 shows the strength of the superconducting order parameter Δ versus

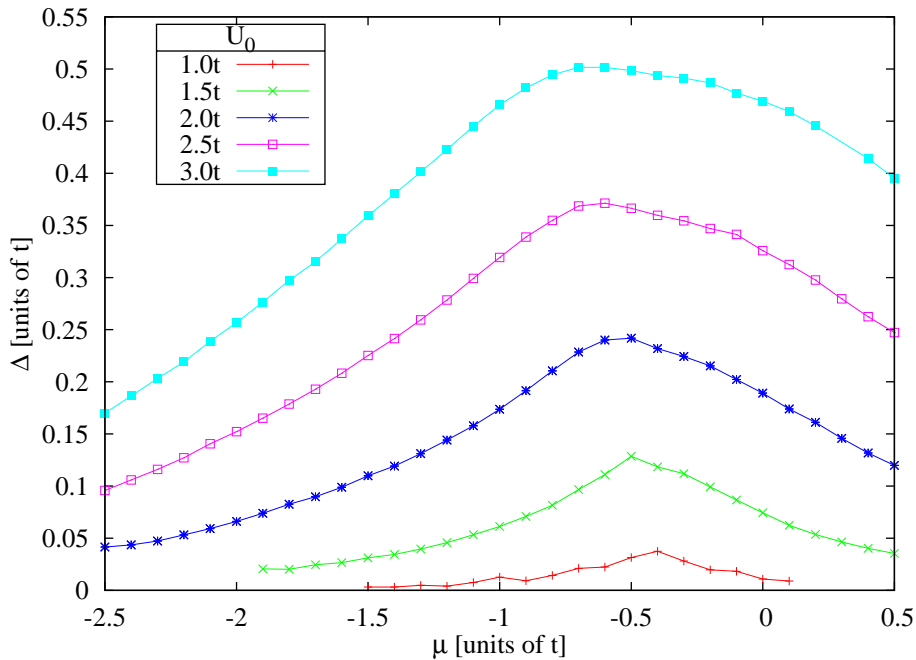


Figure 5.35: Strength of the superconducting order parameter Δ for varying interaction strength U_0 and chemical potential μ , $t' = -0.1t$

the chemical potential as calculated using the interaction flow method including a counterterm as outlined in section 5.3.4. For small bare coupling U_0 , Δ is maximal if the van Hove points lie on the bare Fermi surface, which is the case for $\mu = 4t'$. For larger bare coupling, the maximum gradually shifts to smaller μ .

We study the dependence of the order parameter on the bare coupling U_0 . In Fig. 5.36, we plot three situations: quarter filling, half filling with $t' = -0.1t$, and half filling with $t' = 0$. We compare with the mean-field gap equation (5.15) adapted to the Hubbard model. The lines in the figures result from least-squares

fitting

$$\Delta = \alpha \exp\left(-\frac{\beta}{U_0}\right)$$

to the numerical data at small U_0 via α , β , which works well only away from van Hove filling. The fluctuations neglected in mean-field have been found to have a suppressing effect on the order parameter. The situation has been studied for the extended Hubbard model by van Dongen (1991), for the attractive Hubbard model by Martín-Rodero and Flores (1992), and for fermions moving in a continuous space with an attractive contact interaction by Kuchiev and Sushkov (1996). The values obtained here are quite similar to those obtained by Reiss et al. (2007); Metzner et al. (2006); Reiss (2006), where the suppression factor varies between 1.5 for $U_0 = 3t$ and 3 for $U_0 = 0.5t$ at half filling and $t' = -0.1t$. However, we note that at small couplings, we observe a drop in the gap renormalization $\Delta_{\text{MF}}/\Delta_{\text{RG}}$ for half filling and finite t' and infinite values – suppressed in the figure – for quarter filling and finite t' at small coupling. This is due to numerical problems in resolving such small order parameters as appear for small U_0 . Note that in the half-filled case, hot spots where the Fermi surface intersects the umklapp surface exist, as discussed by Rohe and Metzner (2005); Rohe (2005). In the case of $\mu = t' = 0$, our results agree better with Reiss et al. (2007), but the gap renormalization we obtain is smaller for small couplings. Note that in this case, the Brillouin zone forms a diamond exhibiting zero curvature. The perfect nesting encountered in this situation leads to a degeneracy of density waves and superconductivity (Scalettar et al. (1989)).

In the following, we compare the values of the order parameter we calculate with values of the order parameter calculated with other methods. Table 5.1 compares our fRG results to results obtained by Reiss (2006) using a combination

U [t]	fRG	fRG and MF	random field
1.0	0.04	0.03	0.06
1.5	0.11	0.10	0.09
2.0	0.23	0.21	0.13
2.5	0.35	0.36	0.16
3.0	0.48	0.52*	0.19
3.5	0.62	n.a.	0.22

Table 5.1: Superconducting order parameter Δ in units of t for $t' = 0$, half filling, comparing fRG results to results from a combination of fRG and mean field (MF) as well as from the random field method. *: value obtained using linear extrapolation.

of symmetric-phase fRG and mean field (MF) calculations as well as to results obtained by Gyorffy et al. (1991) using a random-field method. While the agreement with the results obtained using the combination of fRG and mean field is very good, the random field method yields comparable values only coincidentally. It predicts a linear dependence of the order parameter on the bare interaction U_0 for weak up to intermediate coupling. However, in the parameter range studied, it yields the same order of magnitude for the order parameter as the fRG. Table 5.2

compares our results to results by Reiss (2006) for finite t' . While the values are

U [t]	fRG	fRG and MF
1.0	0.02	0.02
1.5	0.11	0.07
2.0	0.22	0.15
2.5	0.35	0.26
3.0	0.49*	0.38

Table 5.2: Superconducting order parameter Δ in units of t for $t' = -0.1t$, $\mu = -0.2612t$ (half filling), comparing fRG results to results from a combination of fRG and MF. *: value obtained using linear extrapolation.

of the same order of magnitude, the results obtained by employing only the fRG are larger by between 20 – 30%.

This concludes the numerical study of the flow equations, showing that it is feasible to obtain reasonable order parameter values for the attractive Hubbard model from them. Furthermore, we have confirmed for weak coupling the strength of the order parameter suppression by fluctuations found in previous studies (Martín-Rodero and Flores (1992); Reiss (2006)), which is approximately 50% for a wide range of parameters.

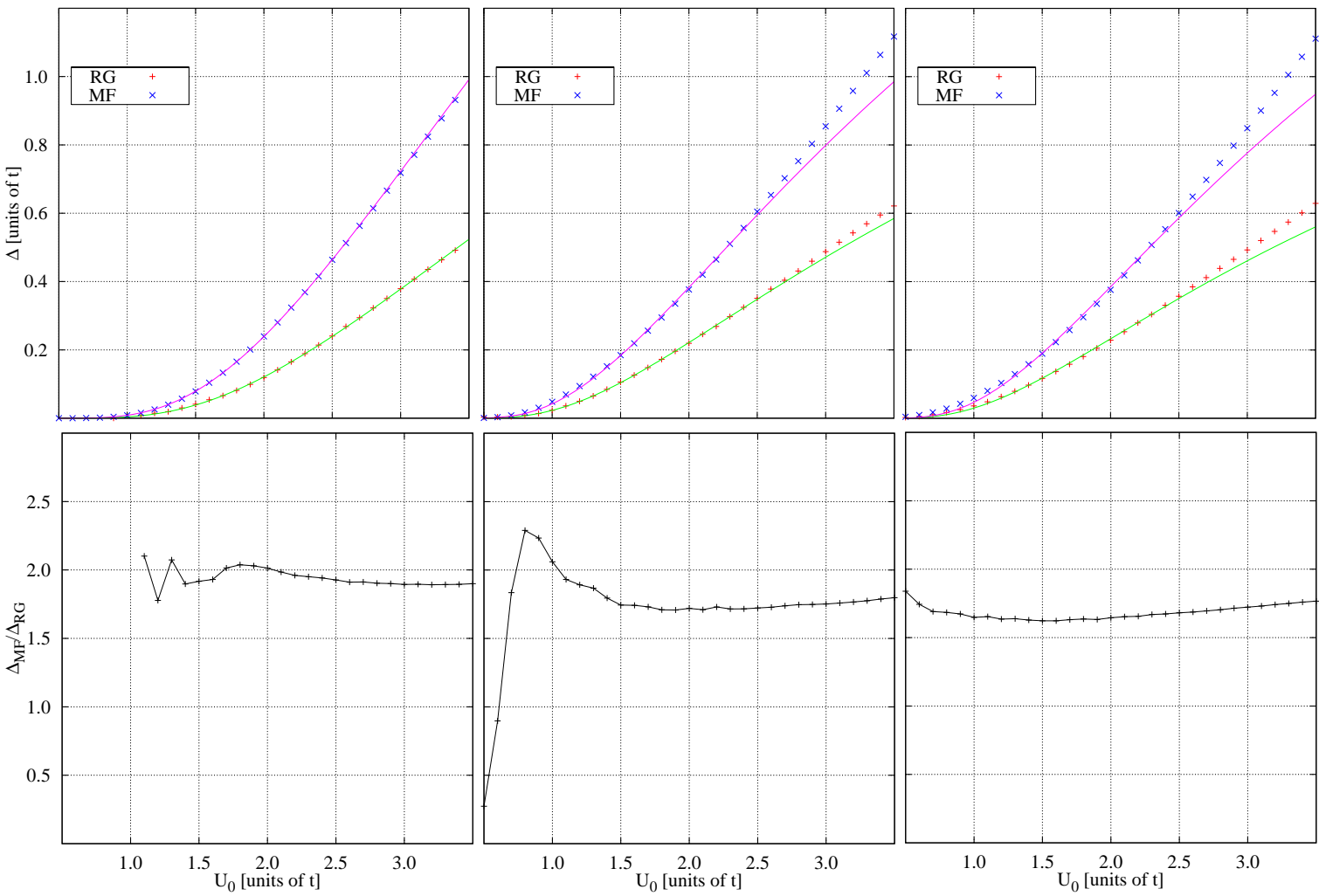


Figure 5.36: Dependence of the superconducting gap on the effective interaction, $t' = -0.1t$ left and center, $t' = 0$ right, $\mu = -1.41t$, $\mu = -0.2612t$, $\mu = 0$ from left to right

Chapter 6

Conclusions

In this work, two new procedures for calculating order parameters in models of itinerant interacting fermions exhibiting spontaneous symmetry breaking were implemented. At the heart of both procedures is the one-particle irreducible functional renormalization group (fRG) method for fermions in a truncation due to Katanin (2004) which solves mean-field models exactly. The method works by solving a set of coupled integro-differential equations for the effective interaction(s) and the order parameter(s) derived from an exact functional differential equation for the effective action. The solution connects initial values that can be read off from a model's definition with the fully renormalized effective values. The first procedure, employing a momentum-shell cutoff and a small external symmetry-breaking field, is an extension of a procedure suggested by Salmhofer et al. (2004) to the breaking of a discrete symmetry at finite and zero temperature, and finally to a non-mean-field model at zero temperature. It was presented here using a generalization of the Nambu formalism that makes it natural to take into account all anomalous effective interactions arising in the symmetry-broken phase. The second procedure combines an interaction flow with a counterterm for the order parameter and was introduced here. It was presented using the same generalized Nambu formalism. In both cases, a family of effective actions is generated in the flow. For the momentum-shell cutoff case, these actions constitute solutions for systems in a constant external symmetry-breaking field where only modes whose kinetic energy exceeds a cutoff scale decreasing in the flow are taken into account. For the interaction-flow case, the effective actions constitute solutions for systems whose bare interaction is the flow parameter in an external symmetry-breaking field which is decreasing in the flow. While the former approach delivers results for only one of possibly many stable, metastable, and unstable equilibrium configurations, the latter approach can treat all of them. By adjusting the initial external symmetry-breaking field which is completely or partly offset at the end of the flow by an appropriate counterterm, we chose the configuration of interest. This also makes it possible to scan the thermodynamic potential landscape of the system for minima corresponding to stable and metastable configurations. This permits the study of spontaneous first-order phase transitions and hysteresis effects, both of which were outside the reach of the fermionic fRG before.

We have illustrated the interaction-flow procedure by the example of a reduced charge-density-wave (CDW) model, which exhibits a first-order phase transition beyond which the lattice translational symmetry – which is discrete – is spontaneously broken. The model is solved exactly by the fRG in the truncation employed here as well as by mean-field theory. For the fRG, this is reflected in the occurrence of one strong attractor for each stable and each metastable configuration, reproducing exact results at zero external field. Flows for all counterterms terminate at one of these attractors. The CDW model also exhibits a second-order phase transition in a certain parameter range. We have studied this transition using both the momentum-shell procedure in a small external field as well as the newly-introduced interaction-flow procedure with a counterterm. As the model is solved exactly, both methods yield the same results. However, a major difference was found in the shape of the flows, with the momentum-shell procedure producing a maximum of the effective interaction at the scale which is critical for zero external field. In contrast, in the interaction-flow procedure the maximal value of the effective interaction is reached only at the end of the flow. The critical-scale maximum also represents a key difference to the momentum-shell treatment of continuous-symmetry breaking by Salmhofer et al. (2004), where the flow of at least one effective interaction saturates at its maximum value in the symmetry-broken phase. While the height of the effective interaction maximum in both cases is singularly dependent on the external field, the saturation value for discrete-symmetry breaking is independent of it. This implies that no collective mode arises as expected for the discrete-symmetry breaking case. The flow of the effective interaction matches the flow of an effective interaction combination present in the fRG flow for continuous-symmetry breaking. We have found that while the maximal effective interaction value is suppressed by increasing the external field, deviations of the order parameter magnitude from the value for spontaneous symmetry breaking grow as the external field is increased for the momentum-shell procedure. This indicates that in our approach for non-mean-field models, a compromise for the strength of the external field must be found to obtain reasonable values from the momentum-shell procedure. This necessity may stem from the discretization, the numerical implementation, the truncation, or any combination of these three factors.

As a precursor study to the application of the method to a more complicated model, a resummation scheme taking into account Cooper and forward scattering by summing up ladders, bubble chains, and all combinations of the two has been developed. The main focus of this study were anomalous effective interactions with an odd number of incoming legs, arising from the above-mentioned combinations of bubbles and ladders and dubbed “3 + 1” effective interactions. To study their influence, the generalized Nambu formalism taking into account anomalous effective interactions was adapted to the case of superconductivity. A reduced model incorporating Cooper and forward scattering processes has been solved exactly. Explicit formulas for all effective interactions have been found and analyzed, especially with regard to the Goldstone mode. The resummation scheme has also been

applied as an approximation to the two-dimensional attractive Hubbard model. Numerical calculations have shown that if one neglects the $3 + 1$ vertices, the effective interactions change only slightly for the momentum combinations most relevant for symmetry-breaking. However, effective interactions for other momentum combinations exhibit changes varying from complete disregard for the $3 + 1$ effective interactions to total suppression by them. The qualitative properties of collective modes were found to be unchanged by the $3 + 1$ effective interactions, as expected.

To study the utility of the fRG procedures for more complicated situations, we have applied both the external-field and the counterterm variant to the attractive Hubbard model at zero temperature, which exhibits superconducting order. In the former case, we have studied the flow of the order parameter as well as of the various effective interactions in detail. We have found that the order parameter saturates at reasonable values even if there are effective interactions in the flow whose magnitude exceeds ten times the bandwidth. However, if the external field is chosen too small thus allowing the effective interactions to grow beyond a certain threshold, the flow of the order parameter stops while the effective interactions diverge at a critical scale. For larger external fields, the effective interaction associated with the Goldstone mode as well as the effective interaction driving the order parameter flow have been found to behave as for the case of the mean-field models. However, $3 + 1$ anomalous effective interactions were shown to arise in the flow for the attractive Hubbard model. These effective interactions diverge in the forward-scattering channel if the external field is sent to zero, but more slowly than the effective interaction associated with the phase mode in the Cooper channel.

For the interaction-flow case, while the strong-attractor behavior from the mean-field models is not reproduced, we have found a clustering of final values for a certain set of counterterms. Together with a limit on the strength of the effective interaction, this allows us to select reasonable results. We have shown such results for the order parameter for a range of interaction strengths and fillings. We have found that especially for half filling and vanishing next-nearest neighbor hopping, our results are very close to results found previously using a combination of fRG and mean-field analysis by Reiss (2006). Away from half-filling, our method consistently yields a larger order parameter than the earlier calculations. The reduction factor comparing the order parameter we calculate to the pure-mean-field result varies between 1.7 and 2.2. This is quite close to approximate values found in the nineties. The procedure newly assembled in this thesis has thus been successfully applied to a lattice model with itinerant fermions and on-site attractive interaction in the superconducting phase.

Anhang A

Deutsche Zusammenfassung

In der vorliegenden Arbeit werden zwei neue Prozeduren zur näherungsweise Bestimmung der mit Symmetriebrechung in Systemen mit itineranten, wechselwirkenden Fermionen assoziierten Ordnungsparameter implementiert. Beide basieren auf der Methode der einteilchenirreduziblen funktionalen Renormierungsgruppe (fRG) für Fermionen in der Trunkierung von Katanin (2004). Diese löst Modelle exakt, wenn sie auch durch Molekularfeldtheorie exakt gelöst werden. Ihr wesentlicher Bestandteil ist ein Satz gekoppelter Integro-Differentialgleichungen für die effektiven Wechselwirkungen und die Ordnungsparameter, der aus einer exakten funktionalen Differentialgleichung für die effektive Wirkung hergeleitet wird (Salmhofer and Honerkamp (2001)). Diese Gleichungen verbinden aus Modelldefinitionen bekannte Anfangsbedingungen mit voll renormierten effektiven Werten. Die erste Prozedur, die einen Impulsschalenfluss und ein kleines äußeres symmetriebrechendes Feld einsetzt, ist eine Erweiterung der von Salmhofer et al. (2004) vorgeschlagenen Prozedur auf endliche Temperaturen, Brechung diskreter Symmetrie und durch Molekularfeldtheorie nicht exakt lösbare Modelle. Sie wird hier unter Benutzung einer Verallgemeinerung des Nambu-Formalismus präsentiert, die alle bei Symmetriebrechung auftretenden anomalen effektiven Zweiteilchenwechselwirkungen berücksichtigt. Die zweite Prozedur kombiniert einen Wechselwirkungsfluss mit einem Gegenterm für den Ordnungsparameter und wird hier eingeführt. In beiden Fällen wird im Fluss eine Schar effektiver Wirkungen generiert. Beim Impulsschalenfluss sind diese effektiven Wirkungen Lösungen für Systeme, bei denen nur Freiheitsgrade berücksichtigt werden, deren kinetische Energie oberhalb einer im Fluss sinkenden Schwelle liegt. Außerdem beziehen sich die Lösungen auf das System in einem kleinen, im Fluss konstanten, symmetriebrechenden äußeren Feld. Beim Wechselwirkungsfluss mit Gegenterm ist die nackte Wechselwirkung der Flussparameter und es ergeben sich Lösungen für ein äußeres Feld, das mit dem Fluss fällt. Während die erste Variante nur ein Ergebnis für eine bestimmte Gleichgewichtskonfiguration ergibt, kann die letztere Resultate für beliebige stabile, metastabile oder labile Gleichgewichtskonfigurationen des Systems liefern. Durch Einstellung des Anfangswert des externen Feldes, das am Ende des Flusses ganz oder teilweise vom Gegenterm kompensiert wird, erfolgt die Auswahl der zu untersuchenden Konfiguration. So ist es möglich, die Landschaft des thermodyna-

mischen Potentials in Abhängigkeit vom Ordnungsparameter zu rastern und auch unbekannte stabile oder metastabile Gleichgewichtskonfigurationen aufzuspüren. Damit wird das Studium von spontanen Phasenübergängen erster Ordnung sowie von Hystereseffekten möglich, die bisher mit der Methode der fermionischen funktionalen Renormierungsgruppe nicht behandelt werden konnten. Ebenso wird die direkte Untersuchung der Situation bei verschwindendem äußeren Feld möglich.

Die Prozedur mit Wechselwirkungsfluss wird am Beispiel eines reduzierten Ladungsdichtewellenmodells illustriert, in dem bei ausreichend niedriger Temperatur und in einem bestimmten Füllungsbereich eine diskrete Symmetrie spontan gebrochen wird. Dieses Modell wird sowohl von der fRG in der hier verwendeten Trunkierung wie auch durch Molekularfeldtheorie exakt gelöst. Für jeden stabilen oder metastabilen Gleichgewichtszustand zeigt sich ein starker Attraktor. Flüsse für beliebige Gegenterme innerhalb eines bestimmten Bereichs enden alle an dem selben Attraktor, und jeder Fluss endet an einem der physikalischen Attraktoren. Sowohl für verschwindendes als auch für endliches externes Feld werden exakte Ergebnisse reproduziert. Das selbe Modell zeigt auch einen Phasenübergang zweiter Ordnung in einem bestimmten Parameterbereich. Der Übergang wird in der vorliegenden Arbeit sowohl mit Hilfe der Impulsschalenprozedur und einem kleinen externen symmetriebrechenden Feld als auch mit der Prozedur mit Wechselwirkungsfluss und einem Gegenterm untersucht. Da das Modell in beiden Fällen exakt gelöst wird, sind die Ergebnisse in allen Situationen, in denen beide Prozeduren funktionieren, identisch. Ein deutlicher Unterschied findet sich aber in der Form der Flüsse. Die Impulsschalenprozedur weist ein deutliches Maximum der effektiven Wechselwirkung an der Skala auf, die bei verschwindendem externen Feld kritisch ist. Im Gegensatz dazu wird bei der Wechselwirkungsstärkenprozedur der Maximalwert der effektiven Wechselwirkung erst am Ende des Flusses erreicht. Ein wesentlicher Unterschied zur Behandlung der Brechung einer kontinuierlichen Symmetrie mit der Impulsschalenprozedur zeigt sich im Sättigungsverhalten des Flusses für kleine Skalen. Während es bei Brechung einer kontinuierlichen Symmetrie eine effektive Wechselwirkung gibt, die bei ihrem Maximalwert sättigt und eine, die zu einem wesentlich kleineren Wert konvergiert, gibt es bei Brechung einer diskreten Symmetrie nur die letztere. Bei dieser hängt zwar die Höhe des Maximums im Fluss singular von der Stärke des externen Feldes ab, der Endwert ist von ihr aber unbeeinflusst. Dies impliziert, dass im Grundzustand keine kollektive Mode auftritt, wie es bei Brechung einer diskreten Symmetrie auch erwartet wird. Der Fluss der effektiven Wechselwirkung im Fall der Brechung einer diskreten Symmetrie entspricht aber dem Fluss einer effektiven Wechselwirkung im Fall der Brechung einer kontinuierlichen Symmetrie. Bei Brechung einer kontinuierlichen Symmetrie tritt eine weitere effektive Wechselwirkung auf, die mit einer Phasen- oder Goldstone-Mode assoziiert wird. Als treibender Faktor für den Fluss des Ordnungsparameters erweist sich in beiden Fällen die *nicht* mit der Goldstone-Mode assoziierte effektive Wechselwirkung. Dementsprechend sättigt die Steigung des Ordnungsparameterflusses für kleine Skalen, so dass ein Endwert in Abhängigkeit vom externen Feld ermittelt werden kann. Während das Maximum der effektiven

Wechselwirkung im Fluss durch Erhöhung der Stärke des externen Felds unterdrückt wird, steigt die Abweichung der Stärke des Ordnungsparameters vom Wert für spontane Symmetriebrechung dadurch. Bei unserer Herangehensweise für die Impulsschalenprozedur müssen für die Wahl der Stärke des externen Feldes beide Effekte berücksichtigt werden, wenn Modelle, für welche die Methode nicht exakt ist, untersucht werden sollen.

Als Vorstudie zur Anwendung der Methode auf ein nicht-reduziertes Modell, für welches keine exakten Ergebnisse zu erwarten sind, wird eine Resummierung der Störungstheorie für die effektive Wechselwirkung vorgenommen. Diese Resummierung berücksichtigt Prozesse im Cooper- und Vorwärtsstreuungskanal durch Summation von Leitern, Blasenketten und allen Kombinationen daraus. Die Untersuchung dient hauptsächlich dem Verständnis der anomalen Wechselwirkungen mit einer ungeraden Anzahl einlaufender Beinchen und Ihrer Bedeutung. Sie entstehen durch die oben beschriebenen Kombinationen aus Leitern und Blasenketten und werden als effektive $3 + 1$ Wechselwirkungen bezeichnet. Ein reduziertes Modell, das sowohl Cooper- als auch Vorwärtsstreuungsprozesse beinhaltet, wird durch die Resummierung exakt gelöst. Es ergeben sich Formeln für alle effektiven Wechselwirkungen, die insbesondere im Hinblick auf die Goldstone-Mode analysiert werden. Die Resummierung wird außerdem als Näherung auf das attraktive Hubbard-Modell in zwei Dimensionen am absoluten Nullpunkt angewandt. Numerische Rechnungen zeigen, dass der Einfluss der effektiven $3 + 1$ Wechselwirkungen bei denjenigen Impulskombinationen, die für die Supraleitung ausschlaggebend sind, schwach ist. Bei anderen Impulskombinationen variiert ihr Einfluss von völliger Unwichtigkeit bis zu völliger Unterdrückung der entsprechenden effektiven Wechselwirkung. Die qualitativen Eigenschaften der kollektiven Moden sind wie erwartet unbeeinflusst von den effektiven $3 + 1$ Wechselwirkungen.

Um die Nützlichkeit der neuen fRG-Prozeduren für nicht-reduzierte Modelle zu untersuchen, werden beide Varianten auf das attraktive Hubbard-Modell in zwei Dimensionen am absoluten Nullpunkt angewandt. Das Modell zeigt dort supraleitende Ordnung. Für die Impulsschalenprozedur werden die Flüsse des Ordnungsparameters und der verschiedenen effektiven Wechselwirkungen analysiert. Der Ordnungsparameter konvergiert zu realistischen Werten, auch wenn die effektiven Wechselwirkungen Maximalwerte annehmen, die ein Zehnfaches der Bandbreite des Systems übersteigen. Allerdings divergieren die effektiven Wechselwirkungen bei einer kritischen Skala, wenn das externe Feld zu klein gewählt wird. In dieser Situation fließt der Ordnungsparameter mit steigender effektiver Wechselwirkung jenseits eines kritischen Werts für diese nicht mehr. Die Divergenz beschränkt sich auf die mit der Goldstone-Mode assoziierte effektive Wechselwirkung, während die den Ordnungsparameter treibende effektive Wechselwirkung entsprechend dessen Verhalten nicht weiter fließt. Für größere externe Felder verhalten sich beide effektive Wechselwirkungen wie in den reduzierten Modellen, die durch Molekularfeldtheorie exakt gelöst werden. Allerdings treten im Fluss für das attraktive Hubbard-Modell effektive $3 + 1$ Wechselwirkungen auf. Diese divergieren im Vorwärtsstreuungskanal wenn das externe Feld gegen Null geht, aber langsamer als die

effektiven Wechselwirkungen, die der Goldstone-Mode im Cooper-Kanal zugeordnet sind.

Bei der Umsetzung der Prozedur mit Wechselwirkungsfluss existiert kein starker Attraktor wie im Fall des Ladungsdichtewellenmodells. Allerdings häufen sich die Endwerte für den Ordnungsparameter für Gegenterme aus einem bestimmten Intervall. Diese Häufung ergibt zusammen mit einer Beschränkung der maximalen effektiven Wechselwirkung ein Kriterium für die Auswahl eines Resultats für den Ordnungsparameter. Die so gewonnenen Ergebnisse sind für verschiedene chemische Potentiale und Wechselwirkungsstärken dargestellt. Insbesondere für halbe Füllung ähneln die ermittelten Werte stark denen, die mit einer Kombination aus fRG und Molekularfeldrechnung gefunden wurden. Abseits halber Füllung liefert die hier verwendete Methode konsistent größere Ergebnisse für den Ordnungsparameter als die kombinierte Rechnung. Der Reduktionsfaktor, der die Unterdrückung des Ordnungsparameters in der fRG-Rechnung im Vergleich zur reinen Molekularfeldrechnung misst, variiert zwischen 1,7 und 2,2. Dies entspricht den Näherungswerten, die in den Neunzigern gefunden wurden. Die neu vorgestellte fRG-Prozedur ist damit erfolgreich als Näherung auf ein bisher nicht exakt gelöstes festkörperphysikalisches Modell mit Symmetriebrechung angewandt worden.

Die Arbeit gliedert sich wie folgt. In Kapitel 2 wird mit Hilfe der Molekularfeldtheorie das Ladungsdichtewellenmodell auf Phasenübergänge erster und zweiter Ordnung untersucht. Die funktionale Renormierungsgruppe wie auch die Katanin-Trunkierung und die Notation zur Behandlung von im Rahmen von Symmetriebrechungen auftretenden anomalen effektiven Wechselwirkungen werden in Kapitel 3 eingeführt. Kapitel 4 enthält die Lösung des Ladungsdichtewellenmodells mittels beider Renormierungsgruppenprozeduren. Die Symmetriebrechung im attraktiven Hubbard-Modell wird in Kapitel 5 sowohl mit beiden Renormierungsgruppenprozeduren als auch mittels einer Resummierung der Störungstheorie behandelt. Ebenso werden dort die effektiven $3 + 1$ Wechselwirkungen an einem reduzierten Modell mit Cooper- und Vorwärtsstreuung ohne Impulsübertrag sowie am attraktiven Hubbard-Modell studiert.

Appendix B

Matsubara sums

$A, B \geq 0$, $\omega_n = (2n + 1)\pi T = (2n + 1)\pi/\beta$, $n_F(x) = \frac{1}{\exp(x/T)+1}$.

$$T \sum_n \frac{1}{\omega_n^2 + A^2} \frac{1}{\omega_n^2 + B^2} = \frac{1}{A^2 - B^2} \left(\frac{\tanh(\beta B/2)}{2B} - \frac{\tanh(\beta A/2)}{2A} \right) \quad (\text{B.1})$$

$$T \sum_n \frac{\omega_n}{\omega_n^2 + A^2} \frac{\omega_n}{\omega_n^2 + B^2} = \frac{1}{2(A^2 - B^2)} (A \tanh(\beta A/2) - B \tanh(\beta B/2)) \quad (\text{B.2})$$

$$T \sum_n \frac{1}{(\omega_n^2 + A^2)^2} = \frac{\tanh(\beta A/2)}{4A^3} - \frac{\beta}{8A^2 \cosh^2(\beta A/2)} \quad (\text{B.3})$$

$$T \sum_n \frac{\omega_n^2}{(\omega_n^2 + A^2)^2} = \frac{\tanh(\beta A/2)}{4A} + \frac{\beta}{8 \cosh^2(\beta A/2)} \quad (\text{B.4})$$

$$T \sum_n \frac{1}{(i\omega_n + A)^2} = -\frac{1}{4T \cosh^2(\beta A/2)} \quad (\text{B.5})$$

$$T \sum_n \frac{1}{\omega_n^2 + A^2} = \frac{\tanh(\beta A/2)}{2A} \quad (\text{B.6})$$

$$T \sum_n \frac{\omega_n^2}{(\omega_n^2 + A^2)^3} = \frac{1}{16A} \left\{ \frac{\beta^2 \tanh(\beta A/2)}{2 \cosh^2(\beta A/2)} - \frac{\beta}{2A \cosh^2(\beta A/2)} + \frac{\tanh(\beta A/2)}{A^2} \right\} \quad (\text{B.7})$$

$$T \sum_n \frac{1}{(\omega_n^2 + A^2)^3} = \frac{1}{16A^3} \left\{ \frac{3 \tanh(\beta A/2)}{A^2} - \frac{3\beta}{2A \cosh^2(\beta A/2)} - \frac{\beta^2 \tanh(\beta A/2)}{2 \cosh^2(\beta A/2)} \right\} \quad (\text{B.8})$$

$\delta > 0$ in the following.

$$T \sum_n \frac{\exp(i\omega_n \delta)}{\omega_n^2 + A^2} = \frac{\sinh[(\beta/2 - \delta)A]}{2A \cosh(\beta A/2)} \quad (\text{B.9})$$

$$T \sum_n \frac{(i\omega_n + A) \exp(i\omega_n \delta)}{\omega_n^2 + A^2} = -\exp(A\delta) \frac{1}{\exp(\beta A) + 1} = -T \sum_n \frac{\exp(i\omega_n \delta)}{i\omega_n - A} \quad (\text{B.10})$$

$$T \sum_n \frac{(i\omega_n - A) \exp(i\omega_n \delta)}{\omega_n^2 + A^2 + B^2} = \frac{1}{2} \left[\frac{\exp(\delta \sqrt{A^2 + B^2})}{\exp(\beta \sqrt{A^2 + B^2}) + 1} \left(\frac{A}{\sqrt{A^2 + B^2}} - 1 \right) - \frac{\exp(-\delta \sqrt{A^2 + B^2})}{\exp(-\beta \sqrt{A^2 + B^2}) + 1} \left(\frac{A}{\sqrt{A^2 + B^2}} + 1 \right) \right] \quad (\text{B.11})$$

$$\xrightarrow{\delta \rightarrow 0} -\frac{A}{2\sqrt{A^2 + B^2}} \tanh(\beta \sqrt{A^2 + B^2}/2) - \frac{1}{2} \quad (\text{B.12})$$

$$T \sum_n \frac{(i\omega_n - A) \exp(-i\omega_n \delta)}{\omega_n^2 + A^2 + B^2} \xrightarrow{\delta \rightarrow 0} -\frac{A}{2\sqrt{A^2 + B^2}} \tanh(\beta \sqrt{A^2 + B^2}/2) + \frac{1}{2} \quad (\text{B.13})$$

$$T \sum_n \frac{1}{\omega_n^2 + Ai\omega_n - B} = \frac{1}{\sqrt{A^2 - 4B}} \left[n_F \left(\frac{1}{2} (A - \sqrt{A^2 - 4B}) \right) - n_F \left(\frac{1}{2} (A + \sqrt{A^2 - 4B}) \right) \right] \quad (\text{B.14})$$

$$T \sum_n \frac{1}{(\omega_n^2 - AB + i\omega_n(A+B))^2} = \frac{1}{(A-B)^2} \left[\frac{2}{A-B} (n_F(B) - n_F(A)) + n'_F(A) + n'_F(B) \right] \quad (\text{B.15})$$

$$T \sum_n \frac{\omega_n^2}{(\omega_n^2 - AB + i\omega_n(A+B))^2} = \frac{1}{(A-B)^2} \left[2 \frac{A^2 n_F(A) - B^2 n_F(B)}{A-B} - 2(A n_F(A) + B n_F(B)) - A^2 n'_F(A) - B^2 n'_F(B) \right] \quad (\text{B.16})$$

$$T \sum_n \frac{i\omega_n}{(\omega_n^2 - AB + i\omega_n(A+B))^2} = \frac{A+B}{(A-B)^3} [n_F(B) - n_F(A)] + \frac{1}{(A-B)^2} [A n'_F(A) + B n'_F(B)] \quad (\text{B.17})$$

Appendix C

Bubble integrands

The bubble integrands below are obtained by Matsubara summing according to (5.46) the products (5.44) of Green's functions (5.13). This operation is performed analytically under the assumption that the self-energy does not depend on frequency, which is in general an approximation. Note that when these expressions are to be used in a renormalization group flow, the cutoff function employed therein must be frequency-independent. Similarly, note for the following formulas that Δ and Σ are to be considered differently in different situations. For a renormalization group flow without counterterm, they are to be multiplied by the cutoff function, and the whole expression must be multiplied by the two cutoff functions corresponding to the two convoluted propagators. If there is a counterterm Δ_c present, Δ must be replaced by $\chi\Delta - \Delta_c$, and the multiplication with χ is necessary as above.

$$\begin{aligned}
 & T \sum_{\omega_n} H(k)H(k+p) = \\
 & - \frac{1}{e^{E_{\mathbf{k}+\mathbf{p}}/T} + 1} \frac{(E_{\mathbf{k}+\mathbf{p}} - (\xi_{\mathbf{k}+\mathbf{p}} + \Sigma_{\mathbf{k}+\mathbf{p}}))(-i\nu_m + E_{\mathbf{k}+\mathbf{p}} - (\xi_{\mathbf{k}} + \Sigma_{\mathbf{k}}))}{2E_{\mathbf{k}+\mathbf{p}}(i\nu_m - E_{\mathbf{k}+\mathbf{p}} + E_{\mathbf{k}})(-i\nu_m + E_{\mathbf{k}+\mathbf{p}} + E_{\mathbf{k}})} \\
 & + \frac{1}{e^{-E_{\mathbf{k}+\mathbf{p}}/T} + 1} \frac{(-E_{\mathbf{k}+\mathbf{p}} - (\xi_{\mathbf{k}+\mathbf{p}} + \Sigma_{\mathbf{k}+\mathbf{p}}))(-i\nu_m - E_{\mathbf{k}+\mathbf{p}} - (\xi_{\mathbf{k}} + \Sigma_{\mathbf{k}}))}{2E_{\mathbf{k}+\mathbf{p}}(i\nu_m + E_{\mathbf{k}+\mathbf{p}} + E_{\mathbf{k}})(-i\nu_m - E_{\mathbf{k}+\mathbf{p}} + E_{\mathbf{k}})} \\
 & - \frac{1}{e^{E_{\mathbf{k}}/T} + 1} \frac{(E_{\mathbf{k}} + i\nu_m - (\xi_{\mathbf{k}+\mathbf{p}} + \Sigma_{\mathbf{k}+\mathbf{p}}))(E_{\mathbf{k}} - (\xi_{\mathbf{k}} + \Sigma_{\mathbf{k}}))}{2E_{\mathbf{k}}(-i\nu_m + E_{\mathbf{k}+\mathbf{p}} - E_{\mathbf{k}})(i\nu_m + E_{\mathbf{k}+\mathbf{p}} + E_{\mathbf{k}})} \\
 & + \frac{1}{e^{-E_{\mathbf{k}}/T} + 1} \frac{(-E_{\mathbf{k}} + i\nu_m - (\xi_{\mathbf{k}+\mathbf{p}} + \Sigma_{\mathbf{k}+\mathbf{p}}))(-E_{\mathbf{k}} - (\xi_{\mathbf{k}} + \Sigma_{\mathbf{k}}))}{2E_{\mathbf{k}}(-i\nu_m + E_{\mathbf{k}+\mathbf{p}} + E_{\mathbf{k}})(i\nu_m + E_{\mathbf{k}+\mathbf{p}} - E_{\mathbf{k}})}
 \end{aligned}$$

$$\begin{aligned}
 & T \sum_{\omega_n} F(k+p)G(k) = \\
 & - \frac{\Delta_{\mathbf{k}+\mathbf{p}}}{e^{E_{\mathbf{k}+\mathbf{p}}/T} + 1} \frac{i\nu_m - E_{\mathbf{k}+\mathbf{p}} - (\xi_{\mathbf{k}} + \Sigma_{\mathbf{k}})}{2E_{\mathbf{k}+\mathbf{p}}(i\nu_m - E_{\mathbf{k}+\mathbf{p}} + E_{\mathbf{k}})(-i\nu_m + E_{\mathbf{k}+\mathbf{p}} + E_{\mathbf{k}})} \\
 & + \frac{\Delta_{\mathbf{k}+\mathbf{p}}}{e^{-E_{\mathbf{k}+\mathbf{p}}/T} + 1} \frac{i\nu_m + E_{\mathbf{k}+\mathbf{p}} - (\xi_{\mathbf{k}} + \Sigma_{\mathbf{k}})}{2E_{\mathbf{k}+\mathbf{p}}(i\nu_m + E_{\mathbf{k}+\mathbf{p}} + E_{\mathbf{k}})(-i\nu_m - E_{\mathbf{k}+\mathbf{p}} + E_{\mathbf{k}})} \\
 & - \frac{\Delta_{\mathbf{k}+\mathbf{p}}}{e^{E_{\mathbf{k}}/T} + 1} \frac{-E_{\mathbf{k}} - (\xi_{\mathbf{k}} + \Sigma_{\mathbf{k}})}{2E_{\mathbf{k}}(-i\nu_m + E_{\mathbf{k}+\mathbf{p}} - E_{\mathbf{k}})(i\nu_m + E_{\mathbf{k}+\mathbf{p}} + E_{\mathbf{k}})} \\
 & + \frac{\Delta_{\mathbf{k}+\mathbf{p}}}{e^{-E_{\mathbf{k}}/T} + 1} \frac{E_{\mathbf{k}} - (\xi_{\mathbf{k}} + \Sigma_{\mathbf{k}})}{2E_{\mathbf{k}}(-i\nu_m + E_{\mathbf{k}+\mathbf{p}} + E_{\mathbf{k}})(i\nu_m + E_{\mathbf{k}+\mathbf{p}} - E_{\mathbf{k}})}
 \end{aligned}$$

$$\begin{aligned}
 & T \sum_{\omega_n} F(k+p)F^*(k) = \\
 & - \frac{\Delta_{\mathbf{k}+\mathbf{p}}\Delta_{\mathbf{k}}^*}{e^{E_{\mathbf{k}+\mathbf{p}}/T} + 1} \frac{1}{2E_{\mathbf{k}+\mathbf{p}}(i\nu_m - E_{\mathbf{k}+\mathbf{p}} + E_{\mathbf{k}})(-i\nu_m + E_{\mathbf{k}+\mathbf{p}} + E_{\mathbf{k}})} \\
 & + \frac{\Delta_{\mathbf{k}+\mathbf{p}}\Delta_{\mathbf{k}}^*}{e^{-E_{\mathbf{k}+\mathbf{p}}/T} + 1} \frac{1}{2E_{\mathbf{k}+\mathbf{p}}(i\nu_m + E_{\mathbf{k}+\mathbf{p}} + E_{\mathbf{k}})(-i\nu_m - E_{\mathbf{k}+\mathbf{p}} + E_{\mathbf{k}})} \\
 & - \frac{\Delta_{\mathbf{k}+\mathbf{p}}\Delta_{\mathbf{k}}^*}{e^{E_{\mathbf{k}}/T} + 1} \frac{1}{2E_{\mathbf{k}}(-i\nu_m + E_{\mathbf{k}+\mathbf{p}} - E_{\mathbf{k}})(i\nu_m + E_{\mathbf{k}+\mathbf{p}} + E_{\mathbf{k}})} \\
 & + \frac{\Delta_{\mathbf{k}+\mathbf{p}}\Delta_{\mathbf{k}}^*}{e^{-E_{\mathbf{k}}/T} + 1} \frac{1}{2E_{\mathbf{k}}(-i\nu_m + E_{\mathbf{k}+\mathbf{p}} + E_{\mathbf{k}})(i\nu_m + E_{\mathbf{k}+\mathbf{p}} - E_{\mathbf{k}})}
 \end{aligned}$$

Appendix D

Tadpole integrands

$$T \sum_{\omega_n} G(i\omega_n, \mathbf{k}) = \frac{1}{2} - (\xi_{\mathbf{k}} + \Sigma_{\mathbf{k}}) \frac{\tanh(E_{\mathbf{k}}/2T)}{2E_{\mathbf{k}}}$$

We assume $\Sigma_{-\mathbf{k}} = \Sigma_{\mathbf{k}}$ and $\Delta_{-\mathbf{k}} = \Delta_{\mathbf{k}}$.

$$T \sum_{\omega_n} H(i\omega_n, \mathbf{k}) = \frac{1}{2} + (\xi_{\mathbf{k}} + \Sigma_{\mathbf{k}}) \frac{\tanh(E_{\mathbf{k}}/2T)}{2E_{\mathbf{k}}}$$

$$T \sum_{\omega_n} F(i\omega_n, \mathbf{k}) = \frac{\Delta_{\mathbf{k}}}{2E_{\mathbf{k}}} \tanh(E_{\mathbf{k}}/2T)$$

Bibliography

- A. ALTLAND and B. SIMONS: *Condensed Matter Field Theory*; Cambridge University Press (2006)
- J. V. ALVAREZ and J. GONZÁLEZ: ‘Weak-coupling phases of the attractive $t-t'$ Hubbard model at the Van Hove filling’; *Europhys. Lett.* **44**: 641 (1998); doi:10.1209/epl/i1998-00520-y; URL <http://stacks.iop.org/0295-5075/44/641>
- S. ANDERGASSEN: *Functional renormalization group analysis of Luttinger liquids with impurities*; Ph.D. thesis; Universität Stuttgart (2006)
- S. ANDERGASSEN, T. ENSS, and V. MEDEN: ‘Kondo physics in transport through a quantum dot with Luttinger-liquid leads’; *Phys. Rev. B* **73**: 153308 (2006); doi:10.1103/PhysRevB.73.153308; URL <http://link.aps.org/abstract/PRB/v73/e153308>
- P. W. ANDERSON: ‘The Resonating Valence Bond State in La₂CuO₄ and Superconductivity’; *Science* **235**: 1196 (1987); doi:10.1126/science.235.4793.1196; URL <http://www.sciencemag.org/cgi/content/abstract/235/4793/1196>
- T. BAIER, E. BICK, and C. WETTERICH: ‘Temperature dependence of antiferromagnetic order in the Hubbard model’; *Phys. Rev. B* **70**: 125111 (2004); doi:10.1103/PhysRevB.70.125111
- T. BAIER, E. BICK, and C. WETTERICH: ‘Antiferromagnetic gap in the Hubbard model’; *Phys. Lett. B* **605**: 144 (2005); doi:10.1016/j.physletb.2004.11.022
- J. BARDEEN, L. N. COOPER, and J. R. SCHRIEFFER: ‘Theory of Superconductivity’; *Phys. Rev.* **108**: 1175 (1957); doi:10.1103/PhysRev.108.1175
- J. G. BEDNORZ and K. A. MÜLLER: ‘Possible high T_c superconductivity in the Ba-La-Cu-O system’; *Zeitschr. f. Phys. B* **64**: 189 (1986); doi:10.1007/BF01303701
- G. BENFATTO and G. GALLAVOTTI: ‘Renormalization-group approach to the theory of the Fermi surface’; *Phys. Rev. B* **42**: 9967 (1990); doi:10.1103/PhysRevB.42.9967

- B. BERGERHOFF, F. FREIRE, D. F. LITIM, S. LOLA, and C. WETTERICH: ‘Phase diagram of superconductors from nonperturbative flow equations’; *Phys. Rev. B* **53**: 5734 (1996); doi:10.1103/PhysRevB.53.5734
- C. CASTELLANI, C. DI CASTRO, F. PISTOLESI, and G. C. STRINATI: ‘Infrared Behavior of Interacting Bosons at Zero Temperature’; *Phys. Rev. Lett.* **78**: 1612 (1997); doi:10.1103/PhysRevLett.78.1612
- R. R. DOS SANTOS: ‘Spin gap and superconductivity in the three-dimensional attractive Hubbard model’; *Phys. Rev. B* **50**: 635 (1994); doi:10.1103/PhysRevB.50.635
- N. DUPUIS: ‘Renormalization group approach to interacting fermion systems in the two-particle-irreducible formalism’; *Eur. Phys. J. B* **48**: 319 (2005); doi:10.1140/epjb/e2005-00409-7
- T. ENSS: *Renormalization, Conservation Laws and Transport in Correlated Electron Systems*; Ph.D. thesis; Universität Stuttgart (2005)
- T. ENSS, V. MEDEN, S. ANDERGASSEN, X. BARNABE-THERIAULT, W. METZNER, and K. SCHONHAMMER: ‘Impurity and correlation effects on transport in one-dimensional quantum wires’; *Phys. Rev. B* **71**: 155401 (2005); doi:10.1103/PhysRevB.71.155401; URL <http://link.aps.org/abstract/PRB/v71/e155401>
- J. FELDMAN, M. SALMHOFER, and E. TRUBOWITZ: ‘Perturbation Theory around nonnested fermi surfaces. I. Keeping the fermi surface fixed’; *J. Statist. Phys.* **84**: 1209 (1996)
- J. FELDMAN, M. SALMHOFER, and E. TRUBOWITZ: ‘Regularity of the moving Fermi surface: RPA contributions’; *Comm. Pure. Appl. Math.* **51**: 1133 (1998)
- J. FELDMAN, M. SALMHOFER, and E. TRUBOWITZ: ‘Regularity of interacting nonspherical Fermi surfaces: The full self-energy’; *Comm. Pure. Appl. Math.* **52**: 273 (1999)
- J. FELDMAN, M. SALMHOFER, and E. TRUBOWITZ: ‘An inversion theorem in Fermi surface theory’; *Comm. Pure. Appl. Math.* **53**: 1350 (2000)
- J. FELDMAN and E. TRUBOWITZ: ‘Perturbation Theory for Many Fermion Systems’; *Helv. Phys. Acta* **63**: 156 (1990)
- J. FELDMAN and E. TRUBOWITZ: ‘The Flow of an Electron-Phonon System to the Superconducting State’; *Helv. Phys. Acta* **64**: 213 (1991)
- H. C. FU, C. HONERKAMP, and D.-H. LEE: ‘Renormalization group study of the electron-phonon interaction in high- T_c cuprates’; *Europhys. Lett.* **75**: 146 (2006); doi:10.1209/epl/i2006-10082-0

- M. GAUDIN: ‘Sur le développement de la grande fonction de partition pour des systèmes de particules identiques’; *Nucl. Phys.* **20**: 513 (1960)
- R. GERSCH, C. HONERKAMP, D. ROHE, and W. METZNER: ‘Fermionic renormalization group flow into phases with broken discrete symmetry: charge-density wave mean-field model’; *Eur. Phys. J. B* **48**: 349 (2005); doi:10.1140/epjb/e2005-00416-8
- R. GERSCH, C. HONERKAMP, D. ROHE, and W. METZNER: ‘Fermionic Renormalization Group Flow at All Scales: Breaking a Discrete Symmetry’; in ‘LECTURES ON THE PHYSICS OF HIGHLY CORRELATED ELECTRON SYSTEMS X: Tenth Training Course in the Physics of Correlated Electron Systems and High Tc Superconductors’, (edited by F. MANCINI and A. AVELLA); pp. 236–244; AIP, Melville, New York (2006a); doi:10.1063/1.2222271; URL <http://link.aip.org/link/?APC/846/236/1>
- R. GERSCH, J. REISS, and C. HONERKAMP: ‘Fermionic functional renormalization-group for first-order phase transitions: a mean-field model’; *New J. Phys.* **8**: 320 (2006b); doi:10.1088/1367-2630/8/12/320
- G. GRÜNER and A. ZETTL: ‘Charge density wave conduction: A novel collective transport phenomenon in solids’; *Phys. Rep.* **119**: 117 (1985); doi:10.1016/0370-1573(85)90073-0
- M. C. GUTZWILLER: ‘Correlation of Electrons in a Narrow s Band’; *Phys. Rev.* **137**: A1726 (1965); doi:10.1103/PhysRev.137.A1726
- B. L. GYORFFY, J. B. STAUNTON, and G. M. STOCKS: ‘Pairing, condensation, and superconductivity described by a Hubbard model with an attractive interaction’; *Phys. Rev. B* **44**: 5190 (1991); doi:10.1103/PhysRevB.44.5190
- C. J. HALBOTH: *Niederenergie-Eigenschaften zweidimensionaler Fermi-Systeme*; Ph.D. thesis; RWTH Aachen (1999)
- C. J. HALBOTH and W. METZNER: ‘d-Wave Superconductivity and Pomeranchuk Instability in the Two-Dimensional Hubbard Model’; *Phys. Rev. Lett.* **85**: 5162 (2000); doi:10.1103/PhysRevLett.85.5162
- C. J. HALBOTH and W. METZNER: ‘Renormalization-group analysis of the two-dimensional Hubbard model’; *Phys. Rev. B* **61**: 7364 (2000); doi:10.1103/PhysRevB.61.7364
- J. E. HIRSCH: ‘Two-dimensional Hubbard model: Numerical simulation study’; *Phys. Rev. B* **31**: 4403 (1985); doi:10.1103/PhysRevB.31.4403
- F. HÖFLING, C. NOWAK, and C. WETTERICH: ‘Phase transition and critical behavior of the $d=3$ Gross-Neveu model’; *Phys. Rev. B* **66**: 205111 (2002); doi:10.1103/PhysRevB.66.205111

- C. HONERKAMP, D. ROHE, S. ANDERGASSEN, and T. ENSS: ‘Interaction flow method for many-fermion systems’; *Phys. Rev. B* **70**: 235115 (2004); doi:10.1103/PhysRevB.70.235115
- C. HONERKAMP and M. SALMHOFER: ‘Temperature-flow renormalization group and the competition between superconductivity and ferromagnetism’; *Phys. Rev. B* **64**: 184516 (2001); doi:10.1103/PhysRevB.64.184516
- C. HONERKAMP, M. SALMHOFER, N. FURUKAWA, and T. M. RICE: ‘Breakdown of the Landau-Fermi liquid in two dimensions due to umklapp scattering’; *Phys. Rev. B* **63**: 035109 (2001); doi:10.1103/PhysRevB.63.035109
- J. HUBBARD: ‘Electron correlations in narrow energy bands’; *P. Roy. Soc. Lond.* **276**: 238 (1963)
- D. JÉROME, T. M. RICE, and W. KOHN: ‘Excitonic Insulator’; *Phys. Rev.* **158**: 462 (1967); doi:10.1103/PhysRev.158.462
- J. KANAMORI: ‘Electron Correlation and Ferromagnetism of Transition Metals’; *Prog. Theor. Phys.* **30**: 275 (1963); doi:10.1143/PTP.30.275
- A. A. KATANIN: ‘Fulfillment of Ward identities in the functional renormalization group approach’; *Phys. Rev. B* **70**: 115109 (2004)
- M. KELLER, W. METZNER, and U. SCHOLLWÖCK: ‘Thermodynamics of a superconductor with strongly bound Cooper pairs’; *Phys. Rev. B* **60**: 3499 (1999); doi:10.1103/PhysRevB.60.3499
- H. C. KRAHL and C. WETTERICH: ‘Functional renormalization group for d-wave superconductivity in Hubbard type models’; *Phys. Lett. A* (2007); doi:10.1016/j.physleta.2007.03.028
- M. Y. KUCHIEV and O. P. SUSHKOV: ‘Many-body correlation corrections to superconducting pairing in two dimensions’; *Phys. Rev. B* **53**: 443 (1996); doi:10.1103/PhysRevB.53.443
- J. S. LANGER: ‘Perturbation Expansions and Functional Integrals in the Theory of Superconductivity’; *Phys. Rev.* **134**: A553 (1964); doi:10.1103/PhysRev.134.A553
- P. A. LEE, T. M. RICE, and P. W. ANDERSON: ‘Conductivity from charge or spin density waves’; *Solid State Commun.* **14**: 703 (1974)
- K. LEVENBERG: ‘A method for the solution of certain problems in least squares’; *Quart. Appl. Math* **2**: 164 (1944)
- G. D. MAHAN: *Many-Particle Physics*; Physics of Solids and Liquids; Kluwer Academic/Plenum Publishers, New York; third edition edition (2000)

- D. W. MARQUARDT: ‘An Algorithm for Least-Squares Estimation of Non-linear Parameters’; *SIAM Journal on Applied Mathematics* **11**: 431 (1963); doi:10.1137/0111030; URL <http://link.aip.org/link/?SMM/11/431/1>
- A. MARTÍN-RODERO and F. FLORES: ‘Solution for the U-negative Hubbard superconductor including second-order correlation effects’; *Phys. Rev. B* **45**: 13008 (1992); doi:10.1103/PhysRevB.45.13008
- V. MEDEN: ‘Funktionale Renormierungsgruppe’; Website of Volker Meden (2005); URL <http://www.theorie.physik.uni-goettingen.de/~meden/funRG/>
- W. METZNER: ‘Functional Renormalization Group Computation of Interacting Fermi Systems’; *Prog. Theor. Phys. Suppl.* **160**: 58 (2005)
- W. METZNER, C. CASTELLANI, and C. DI CASTRO: ‘Fermi systems with strong forward scattering’; *Adv. Phys.* **47**: 317 (1998)
- W. METZNER, J. REISS, and D. ROHE: ‘Magnetic and superconducting correlations in the two-dimensional Hubbard model’; *phys. status solidi (b)* **243**: 46 (2006)
- W. METZNER, D. ROHE, and S. ANDERGASSEN: ‘Soft Fermi Surfaces and Breakdown of Fermi-Liquid Behavior’; *Phys. Rev. Lett.* **91**: 066402 (2003); doi:10.1103/PhysRevLett.91.066402
- R. MICNAS, J. RANNINGER, and S. ROBASZKIEWICZ: ‘Superconductivity in narrow-band systems with local nonretarded attractive interactions’; *Rev. Mod. Phys.* **62**: 113 (1990); doi:10.1103/RevModPhys.62.113
- T. MORRIS: ‘The exact renormalization group and approximate solutions’; *Int. J. Mod. Phys. A* **9**: 2411 (1994)
- B. MÜHLSCHLEGEL: ‘Asymptotic Expansion of the Bardeen-Cooper-Schrieffer Partition Function by Means of the Functional Method’; *J. Math. Phys.* **3**: 522 (1962)
- J. W. NEGELE and H. ORLAND: *Quantum Many-Particle Systems*; Westview Press (1998)
- A. NEUMAYR and W. METZNER: ‘Renormalized perturbation theory for Fermi systems: Fermi surface deformation and superconductivity in the two-dimensional Hubbard model’; *Phys. Rev. B* **67**: 035112 (2003); URL <http://link.aps.org/abstract/PRB/v67/e035112>
- J. F. NICOLL and T. S. CHANG: ‘An exact one-particle-irreducible renormalization-group generator for critical phenomena’; *Phys. Lett. A* **62**: 287 (1977); doi:10.1016/0375-9601(77)90417-0

- F. PISTOLESI, C. CASTELLANI, C. DI CASTRO, and G. C. STRINATI: ‘Renormalization-group approach to the infrared behavior of a zero-temperature Bose system’; *Phys. Rev. B* **69**: 024513 (2004); doi:10.1103/PhysRevB.69.024513; URL <http://link.aps.org/abstract/PRB/v69/e024513>
- J. POLCHINSKI: ‘Renormalization and effective lagrangians’; *Nuclear Physics B* **231**: 269 (1984); doi:10.1016/0550-3213(84)90287-6
- V. N. POPOV: *Functional Integrals and Collective Excitations*; Cambridge University Press (1991)
- M. RANDEIRA, N. TRIVEDI, A. MOREO, and R. T. SCALETTAR: ‘Pairing and spin gap in the normal state of short coherence length superconductors’; *Phys. Rev. Lett.* **69**: 2001 (1992); doi:10.1103/PhysRevLett.69.2001
- J. REISS: *Renormalised Mean-Field Analysis of the 2D Hubbard Model*; Ph.D. thesis; Universität Stuttgart (2006)
- J. REISS, D. ROHE, and W. METZNER: ‘Renormalized mean-field analysis of antiferromagnetism and d-wave superconductivity in the two-dimensional Hubbard model’; *Phys. Rev. B* **75**: 075110 (2007); doi:10.1103/PhysRevB.75.075110; URL <http://link.aps.org/abstract/PRB/v75/e075110>
- M. J. RICE and S. STRÄSSLER: ‘Theory of a quasi-one-dimensional band-conductor’; *Solid State Commun.* **13**: 125 (1973)
- S. ROBASZKIEWICZ, R. MICNAS, and K. A. CHAO: ‘Thermodynamic properties of the extended Hubbard model with strong intra-atomic attraction and an arbitrary electron density’; *Phys. Rev. B* **23**: 1447 (1981); doi:10.1103/PhysRevB.23.1447
- D. ROHE: *Renormierungsgruppenanalyse des Hubbard-Modells in zwei Dimensionen*; Ph.D. thesis; Universität Stuttgart (2005)
- D. ROHE and W. METZNER: ‘Pair-fluctuation-induced pseudogap in the normal phase of the two-dimensional attractive Hubbard model at weak coupling’; *Phys. Rev. B* **63**: 224509 (2001); doi:10.1103/PhysRevB.63.224509
- D. ROHE and W. METZNER: ‘Pseudogap at hot spots in the two-dimensional Hubbard model at weak coupling’; *Phys. Rev. B* **71**: 115116 (2005); doi:10.1103/PhysRevB.71.115116; URL <http://link.aps.org/abstract/PRB/v71/e115116>
- L. ROSA, P. VITALE, and C. WETTERICH: ‘Critical Exponents of the Gross-Neveu Model from the Effective Average Action’; *Phys. Rev. Lett.* **86**: 958 (2001); doi:10.1103/PhysRevLett.86.958

- M. SALMHOFER: ‘Continuous Renormalization for Fermions and Fermi Liquid Theory’; *Comm. Math. Phys.* **194**: 249 (1998a); doi:10.1007/s002200050358
- M. SALMHOFER: ‘Renormalization: An Introduction’; *Springer Texts and Monographs in Physics*, Springer, Heidelberg (1998b)
- M. SALMHOFER and C. HONERKAMP: ‘Fermionic Renormalization Group Flows—Technique and Theory—’; *Prog. Theor. Phys.* **105**: 1 (2001)
- M. SALMHOFER, C. HONERKAMP, W. METZNER, and O. LAUSCHER: ‘Renormalization Group Flows into Phases with Broken Symmetry’; *Prog. Theor. Phys.* **112**: 943 (2004)
- R. T. SCALETTAR, E. Y. LOH, J. E. GUBERNATIS, A. MOREO, S. R. WHITE, D. J. SCALAPINO, R. L. SUGAR, and E. DAGOTTO: ‘Phase Diagram of the Two-Dimensional Negative- U Hubbard Model’; *Phys. Rev. Lett.* **63**: 218 (1989); doi:10.1103/PhysRevLett.63.218
- F. SCHÜTZ, L. BARTOSCH, and P. KOPIETZ: ‘Collective fields in the functional renormalization group for fermions, Ward identities, and the exact solution of the Tomonaga-Luttinger model’; *Phys. Rev. B* **72**: 035107 (2005); doi:10.1103/PhysRevB.72.035107
- F. SCHÜTZ and P. KOPIETZ: ‘Functional renormalization group with vacuum expectation values and spontaneous symmetry breaking’; *J. Phys. A* **39**: 8205 (2006); doi:10.1088/0305-4470/39/25/S28
- R. SHANKAR: ‘Renormalization group for interacting fermions in $d > 1$ ’; *Physica A* **177**: 530 (1991); doi:10.1016/0378-4371(91)90197-K
- R. SHANKAR: ‘Renormalization-group approach to interacting fermions’; *Rev. Mod. Phys.* **66**: 129 (1994); doi:10.1103/RevModPhys.66.129
- J. M. SINGER, M. H. PEDERSEN, T. SCHNEIDER, H. BECK, and H.-G. MATUTTIS: ‘From BCS-like superconductivity to condensation of local pairs: A numerical study of the attractive Hubbard model’; *Phys. Rev. B* **54**: 1286 (1996); doi:10.1103/PhysRevB.54.1286
- P. STRACK, R. GERSCH, and W. METZNER: ‘NN’; *in preparation* (2007)
- A. TOSCHI, P. BARONE, M. CAPONE, and C. CASTELLANI: ‘Pairing and superconductivity from weak to strong coupling in the attractive Hubbard model’; *New J. Phys.* **7**: 7 (2005a); doi:10.1088/1367-2630/7/1/007; URL <http://stacks.iop.org/1367-2630/7/7>
- A. TOSCHI, M. CAPONE, and C. CASTELLANI: ‘Energetic balance of the superconducting transition across the BCS—Bose Einstein crossover in the attractive Hubbard model’; *Phys. Rev.*

- B* **72**: 235118 (2005b); doi:10.1103/PhysRevB.72.235118; URL <http://link.aps.org/abstract/PRB/v72/e235118>
- P. G. J. VAN DONGEN: ‘Thermodynamics of the extended Hubbard model in high dimensions’; *Phys. Rev. Lett.* **67**: 757 (1991); doi:10.1103/PhysRevLett.67.757
- F. J. WEGNER and A. HOUGHTON: ‘Renormalization Group Equation for Critical Phenomena’; *Phys. Rev. A* **8**: 401 (1973); doi:10.1103/PhysRevA.8.401
- S. WEINBERG: ‘New Approach to the Renormalization Group’; *Phys. Rev. D* **8**: 3497 (1973); doi:10.1103/PhysRevD.8.3497
- C. WETTERICH: ‘Exact evolution equation for the effective potential’; *Phys. Lett. B* **301**: 90 (1993); doi:10.1016/0370-2693(93)90726-X
- C. WIECZERKOWSKI: ‘Symanzik’s improved actions from the viewpoint of the renormalization group’; *Comm. Math. Phys.* **120**: 149 (1988); doi:10.1007/BF01223210
- K. G. WILSON: ‘Renormalization Group and Critical Phenomena. I. Renormalization Group and the Kadanoff Scaling Picture’; *Phys. Rev. B* **4**: 3174 (1971a); doi:10.1103/PhysRevB.4.3174
- K. G. WILSON: ‘Renormalization Group and Critical Phenomena. II. Phase-Space Cell Analysis of Critical Behavior’; *Phys. Rev. B* **4**: 3184 (1971b); doi:10.1103/PhysRevB.4.3184
- K. G. WILSON: ‘Renormalization of a Scalar Field Theory in Strong Coupling’; *Phys. Rev. D* **6**: 419 (1972); doi:10.1103/PhysRevD.6.419
- H. YAMASE and H. KOHNO: ‘Possible Quasi-One-Dimensional Fermi Surface in $\text{La}_{2-x}\text{Sr}_x\text{CuO}_4$ ’; *J. Phys. Soc. Japan* **69**: 332 (2000); doi:10.1143/JPSJ.69.332; URL <http://jpsj.ipap.jp/link?JPSJ/69/332/>
- H. YAMASE, V. OGANESYAN, and W. METZNER: ‘Mean-field theory for symmetry-breaking Fermi surface deformations on a square lattice’; *Phys. Rev. B* **72**: 035114 (2005); doi:10.1103/PhysRevB.72.035114
- D. ZANCHI and H. J. SCHULZ: ‘Weakly correlated electrons on a square lattice: A renormalization group theory’; *Europhys. Lett.* **44**: 235 (1998); doi:10.1209/epl/i1998-00462-x; URL <http://stacks.iop.org/0295-5075/44/235>
- D. ZANCHI and H. J. SCHULZ: ‘Weakly correlated electrons on a square lattice: Renormalization-group theory’; *Phys. Rev. B* **61**: 13609 (2000); doi:10.1103/PhysRevB.61.13609

Acknowledgments

First of all, I would like to thank my advisor, Prof. Dr. Walter Metzner, for his unwavering friendliness and his invaluable advice. My second mentor, Prof. Dr. Carsten Honerkamp, has spent countless hours patiently explaining solid state theory to me and was a great partner in several projects. Two former Ph.D. students I am particularly indebted to are Dr. Daniel Rohe, who always kept me believing that what I was trying was doable, and Dr. Julius Reiss, who was always willing to share his great treasure of knowledge with me. I thank Dr. Hiroyuki Yamase for sharing an office with me for several years, always gladly answering my questions. Through his fast-paced and fascinating lectures, Prof. Dr. Alejandro Muramatsu allowed me to understand a number of things about the renormalization group. To him I am also grateful for co-assessing this work. Prof. Dr. Martin Zirnbauer taught me a large portion of what I know about theoretical physics, and is thanked for that.

On the personal side, I am grateful to Kristina Piecha, who was always supportive while having to compensate my rashness with her own prudence. My parents Uschi and Claus Gersch gladly counselled well me whenever I asked for advice. My brother Rainer Gersch brought a refreshingly down-to-earth view to many situations, and simplified a number of things. All three cannot be thanked enough.

For making a great effort to improve the Ph.D. students' experience at the Stuttgart Max Planck Institutes, and being thoroughly enjoyable colleagues for a year, I thank Hasan Cakmak, Peter Lipowsky, and Christian Michaelis.

Extending the circle are a number of more or less senior colleagues who, working on related or unrelated problems, are to be thanked for being ready and willing to think about mine: Dr. Andrey Katanin, Dr. Tilman Enss, Dr. Sabine Andergassen, Philipp Strack, Dr. Karsten Held, Prof. Dr. Thierry Giamarchi, Prof. Dr. Wolfgang von der Linden, and Prof. Dr. Manfred Salmhofer. I enjoyed many delightful discussions about physics and otherwise with Dr. Maria Daghofer, Julia Unterhinninghofen, Dr. Philip Brydon, Dr. Danilo Neuber, Dr. Anup Mishra, Dr. Corinna Kollath, Dr. Dirk Manske, Dr. Heinz Barentzen, Dr. Roland Zeyher, Krzysztof Wohlfeld, Philipp Hansmann, Dr. Peter Horsch, Dr. Ioannis Zegkinoglou, Vladimir Hinkov, Anton Suchaneck, Dr. Yi-Feng Yang, Dr. Sergej Brener, Dr. Hans-Christian Krahl, and Dr. Inga Fischer.

Finally, I thank my referees for contributing many useful suggestions for my papers.

To all I have forgotten I owe apologies, and I beg their forgiveness.

Published previously

Parts of this work were published previously in Gersch et al. (2005), Gersch et al. (2006a), and Gersch et al. (2006b).

Curriculum Vitae

Name	Simon <u>Roland</u> Gersch
Date of birth	May 10th, 1979
Place of birth	Köln
Nationality	German

Education and employment

06/1998	Abitur, Gymnasium Sürther Straße in Köln
08/1998-08/1999	Civil Service, Arbeiterwohlfahrt Köln
10/1999-06/2004	Studies of physics, Universität zu Köln
06/2004	Diploma in physics, thesis on <i>Randbedingungen für mesoskopische Systeme mit Dirac-Näherung</i> supervised by Prof. Dr. Martin R. Zirnbauer
09/2004-today	Ph.D. studies supervised by Prof. Dr. Walter Metzner at the Max-Planck-Institut für Festkörperforschung, Stuttgart

Stuttgart, July 31 2007